

**FOLDING AND BOUDINAGE UNDER
CONSTRICION AND PLANE STRAIN: RESULTS
FROM ANALOGUE MODELLING**

Dissertation
Zur Erlangung des Doktorgrades
der Naturwissenschaften

vorgelegt beim Fachbereich Geowissenschaften
der Johann Wolfgang Goethe – Universität
in Frankfurt am Main

von
Mathurin Enama Mengong
aus Jaunde (Kamerun)

Frankfurt am Main, 2005

vom Fachbereich Geowissenschaften der

Johann Wolfgang Goethe – Universität als Dissertation angenommen.

Dekan:

Gutachter:

Datum der Disputation:

ACKNOWLEDGEMENTS

During this research work, I had the opportunity to learn many new things and to understand many old things.

First, I would like to express my gratitude to my supervisor Prof. Dr. Gernold Zulauf for setting up the project and giving me the possibility to work in his group. For all his duties, he has always taken the time to explain complex topics in an understandable way. The benefit of this collaboration is invaluable.

I am grateful to the staff of the Division of Neuroradiology of the University hospital in Erlangen, especially Dr. B.F. Tomandl for providing the Computer Tomography. In addition, I am very much obliged to Dr. Joachim Kaschta and Ralf Kürschner, Lehrstuhl für Polymerwerkstoffe, Werkstoffwissenschaften, Universität Erlangen-Nürnberg, for providing the traction apparatus and for support when using the machine.

My deep respect is due to Prof. Dr. Bernhard Schulz. With him, I had, many interesting discussions concerning folding and boudinaging and his constructive critics contributed significant to this research work.

I would like to extend a very special thank you to Dr. Carlo Dietl for providing me with very helpful comments, critics, and Dr. Janet Zulauf for her invaluable contribution to CT images and for support and useful discussions.

I am very grateful to S. Schmalholz, S.H. Treagus, H. Koyi and N.S Mancktelow for support and providing me with very helpful comments and critics.

I thank DFG (Deutsche Forschungsgemeinschaft, Zu 73/7), and DAAD (Deutscher Akademischer Austauschdienst A/01/20519) for providing financial support during my work.

Many more persons contributed to my PhD in various ways and made my stay in Erlangen and Frankfurt a real pleasure. Konrad Kunz always helped in case of problems with laboratory equipment, Dani Lutz, Mrs Kühnert, Mrs Klein and Mrs Schlapp for the

friendship. Thanks to all members of the Institut für Geologie und Mineralogie at Erlangen for the good time. Thanks a lot for everything Dipl. Ing. Steve Oswald Pentang Mbandou, Dipl. Ing. Francky Jöel Nna, Sandra Romano, Elena Galadí-Enríquez, Thomas Klein, Gautier Njiekak, Dr. Michel Bestmann, Dr. Leonard Elat, Prof. Dr Rohan Weerasooriya, and Prof. Dr Dissanayake.

I am very grateful to my parents and my brothers and sisters who always supported me during my studies and this PhD work. Joséphine Mendana Nsah, without you the past years would never have been so beautiful. Thank you so much for your support and your love.

ABSTRACT

One possible approach to study systematically the influence of the deformation regime on the geometry of geological structures like folds and boudins is analogue modelling. For a complete understanding of the resulting structures, consideration of the third dimension is required.

This PhD study deals with scaled analogue modelling under *constriction* and *plane-strain conditions* to improve our knowledge of folding and boudinage of lower crustal rocks in space and time. Plasticine is an appropriate analogue material for rocks in the lower crust. Therefore, this material was used for the experiments. The macroscopic behaviour of most types of plasticine is quite similar to rocks undergoing strain-rate softening and strain hardening regardless of the different microscopic aspects of deformation. Therefore, if one is aware that the stress exponent and viscosity increase with increasing strain, the original plasticine types used with stress exponents ranging from 5.8 to 8.0 are adequate for modelling geologic structures. The same holds for plasticine/oil mixtures. Thus, plasticine and plasticine/oil mixtures can be used to model the viscous flow of different rock types in the lower crust. If climb-accommodated dislocation creep and associated steady-state flow is assumed for the natural rocks, the plasticine/oil mixtures should be used, which flow under steady-state conditions.

Three different experimental studies of plane-strain coaxial deformation of stiff layers, with viscosity η_2 and stress exponent n_2 , embedded in a weak matrix, with viscosity η_1 and stress exponent n_1 , have been carried out. The undeformed samples (matrix plus layer) were cubes with an edge length of 12 cm. All experimental runs have been carried out at $T = 25 \pm 1^\circ\text{C}$ and varying strain rates $\dot{\epsilon}$, ranging from $7.9 \times 10^{-6} \text{ s}^{-1}$ to $1.7 \times 10^{-2} \text{ s}^{-1}$, until a finite longitudinal strain of 30% – 40% was achieved.

The first experimental study improved the understanding about the evolution of folds and boudins when the layer is oriented perpendicular to the Y -axis of the finite strain ellipsoid. The rock analogues used were *Beck's green* plasticine (matrix) and *Beck's black* plasticine (competent layer), both of which are strain-rate softening modelling materials with stress exponent $n = \text{ca. } 8$. The effective viscosity η of the matrix plasticine was changed by adding different amounts of oil to the original plasticine. At a strain rate $\dot{\epsilon}$ of 10^{-3} s^{-1} and a finite strain e of 10%, the effective viscosity of the matrix ranges from 1.2×10^6 to $7.2 \times 10^6 \text{ Pa s}$. The effective viscosity of the competent layer has been determined as $4.2 \times 10^7 \text{ Pa s}$. If the viscosity ratio is large ($> \text{ca. } 20$) and the initial thickness of the competent layer is small, both folds and boudins develop simultaneously. Although the growth rate of the folds seems to be higher than the growth rate of the boudins, the wavelength of both structures is approximately the same as is suggested by analytical solutions. A further unexpected, but characteristic, aspect of the deformed competent layer is a significant increase in thickness, which can be used to distinguish plane-strain folds and boudins from constrictional folds and boudins.

In the second experimental study, the impact of varying strain rates on growing folds and boudins under plane strain have been investigated. The strain rates used range from $7.9 \times 10^{-6} \text{ s}^{-1}$ to $1.7 \times 10^{-2} \text{ s}^{-1}$. The stiff layer and matrix consist of non-linear viscous *Kolb grey* and *Beck's green* plasticine, respectively, both of which are strain-rate softening modelling materials with power law exponents (n) and apparent viscosities (η) ranging from 6.5 to 7.9 and 8.5×10^6 to $7.2 \times 10^6 \text{ Pa s}$, respectively. The effective viscosity (η) of the matrix plasticine was partly modified by adding oil to the original plasticine. At the strain rates used in the experiments the viscosity ratio between layer and matrix ranges between 3 and 10. Different runs have been carried out where the layer was oriented perpendicular to the principal strain axes ($X > Y > Z$). The results suggest a considerable influence of the strain rate on the geometry of the deformed stiff layer including its thickness. This holds for every type of layer orientation ($S \perp X, S \perp Y, S \perp Z$). If the stiff layer is oriented perpendicular to the short

axis Z of the finite strain ellipsoid, the number of the resulting boudins and the thickness of the stiff layer increase, whereas the length of boudins decreases with increasing strain rate. If the stiff layer is oriented perpendicular to the long axis, X , of the finite strain ellipsoid, enlargement of the strain rate results in increasing wavelength of folds, whereas the number of folds and the degree of thickening of the stiff layer decreased. If the stiff layer is oriented perpendicular to the intermediate Y -axis of the finite strain ellipsoid enlargement of the strain rate results in a decreasing number of boudins and folds associated with increasing wavelengths of both structures.

The wavelength of folds is approximately half of the boudins wavelength. This is true for the case where folds and boudins develop simultaneously ($S \perp Y$) and for cases where both structures develop independently (folds at $S \perp X$ and boudins at $S \perp Z$).

In the third experimental study, scaled analogue experiments have been carried out to demonstrate the growth of plane-strain folds and boudins through space and time. Previous 3D-studies are based only on finite deformation structures. Their results can therefore not be used to prove if both structures grew simultaneously or in sequence. Plane strain acted on a single stiff layer that was embedded in a weak matrix, with the layer oriented perpendicular to the intermediate Y -axis of the finite strain ellipsoid. Two different experimental runs have been carried out using computer tomography (CT) to analyse the results. The first run was carried out without interruption. During the second run, the deformation was stopped in each case at longitudinal strain increments of 10%. Every experiment was carried out at a temperature T of 25°C and a strain rate, $\dot{\epsilon}$, of ca. $4 \times 10^{-3} \text{ s}^{-1}$ until a finite longitudinal strain of 40% was achieved with a viscosity contrast m of 18.6 between the non-linear viscous layer (*Kolb brown* plasticine) and the matrix (*Beck's green* plasticine with 150 ml oil kg^{-1}). The apparent viscosity, η , and the stress exponent, n , for the layer at a strain rate $\dot{\epsilon} = \text{ca. } 10^{-3} \text{ s}^{-1}$ and a finite strain $e = 10\%$ are $2.23 \times 10^7 \text{ Pa s}$ and $n = 5.8$ and for the matrix $1.2 \times 10^6 \text{ Pa s}$ and

10.5. These new data that result from incremental analogue modelling corroborate previous suggestions that folds and boudins are coeval structures in cases of plane-strain coaxial deformation with the stiff layer oriented perpendicular to the intermediate Y -axis of the finite strain ellipsoid. They will be of interest for all workers who are dealing with plane-strain boudins and folds, where the fold axes are parallel to the major axis (X) of the finite strain ellipsoid.

As has been demonstrated by the first experimental study, coeval folding and boudinage under plane strain, with $S \perp Y$, are associated with a significant increase in the thickness of the competent layer. The latter phenomenon does not occur in other cases of simultaneous folding and boudinage, such as bulk pure constriction. To study the impact of layer thickness on the geometry of folds and boudins under pure constriction, we carried out additional experiments using different types of plasticine for a stiff layer and a weaker matrix to model folding and boudinaging under pure constriction, with the initially planar layer oriented parallel to the X -axis of the finite strain ellipsoid. The stiff layer and matrix consist of non-linear viscous *Kolb brown* and *Beck's green* plasticine, respectively, both of which are strain-rate softening modelling materials. Six runs have been carried out using thicknesses of the stiff layer of 1, 2, 4, 6, 8 and 10 ± 0.2 mm. All experimental runs were carried out at a temperature T of $30 \pm 2^\circ\text{C}$ and a strain rate, $\dot{\epsilon}$, of ca. $1.1 \times 10^{-4} \text{ s}^{-1}$ until a finite longitudinal strain of 40% was achieved with a viscosity contrast m of 3.1 between the stiff layer (*Kolb brown* plasticine) and the matrix (*Beck's green* plasticine). The apparent viscosity, η , and the stress exponent, n , for the layer at a strain rate $\dot{\epsilon} = \text{ca. } 10^{-3} \text{ s}^{-1}$ and a finite strain $e = 10\%$ are $2.23 \times 10^7 \text{ Pa s}$ and $n = 5.8$ and for the matrix $7.2 \times 10^6 \text{ Pa s}$ and 7.9. Our results suggest a considerable influence of the initial thickness of the stiff layer on the geometry of the deformed stiff layer. There is no evidence for folding in $XY=YZ$ -sections if the initial thickness of the competent layer is larger than ca. 8 mm. If the initial thickness of the competent layer is set at ca. 10 ± 0.2 mm, both folds and boudins develop simultaneously. However, the growth rate of the boudins seems to

be higher than the growth rate of the folds. A further expected, but characteristic, aspect of the deformed competent layer is no change in thickness of the competent layer, which can be used to distinguish plane-strain folds and boudins from constrictional folds and boudins. The model results are important for the analysis and interpretation of deformation structures in rheologically stratified rocks undergoing dislocation creep under bulk constriction. Tectonic settings where constrictional folds and boudins may develop simultaneously are stems of salt diapirs, subduction zones or thermal plumes.

To make (paleo) viscosimetric statements possible, the rheological data of the different plasticine types were related to the geometrical data. When comparing the normalized dominant wavelength W_d obtained from the deformed layer of the models with the theoretical dominant wavelength (L_d) calculated using the Smith equation (1977, 1979), the latter probably also holds when folding and boudinage develop simultaneously ($S \perp Y$) and when boudins develop independently ($S \perp Z$), but can obviously not be applied at very low viscosity ratios as is indicated by the low-strain-rate experiments.

ZUSAMMENFASSUNG

Um den Einfluss des Deformationsregimes auf die Geometrie von geologischen Strukturen wie Falten und Boudins systematisch zu studieren, werden häufig Analogmodellierungen durchgeführt. Zum Verständnis der dabei modellierten Strukturen ist die Berücksichtigung der dritten Dimension erforderlich.

Im Rahmen meiner Doktorarbeit habe ich Analogexperimente unter konstriktionalen und ebenen Verformungsbedingungen durchgeführt, um das Wissen über die raumzeitliche Bildung von Falten und Boudins in der tieferen Kruste zu erweitern. Eine wesentliche Voraussetzung für die Durchführung von skalierten Modellierungen ist, dass das rheologische Verhalten des Analogmaterials hinreichend genau bekannt ist. Die rheologischen Bedingungen der Unterkruste lassen sich gut mit Plastilin simulieren. Daher wurde dieses Material für die hier vorgestellte Modellierung verwendet und vor den eigentlichen Modellierungen rheologische Analysen an den verwendeten Plastilintypen durchgeführt. Das makroskopische rheologische Verhalten der meisten Plastilintypen ist dem von Unterkrustengesteinen ähnlich, die „strain rate softening“ und „strain hardening“ erfahren, unabhängig von den unterschiedlichen mikroskopischen Aspekten der Deformation der beiden Materialien. Wenn man also beachtet, dass der Spannungsexponent und die Viskosität sich mit Zunahme des Strains erhöhen, sind Plastilintypen mit Spannungsexponenten zwischen 5.8 und 8.0 für das Modellieren von geologischen Strukturen geeignet. Dasselbe gilt für Plastilin/Öl Mischungen. Daher können Plastilin und Plastilin/Öl Mischungen benutzt werden, um das viskose Fließen verschiedener Gesteine der Unterkrust zu modellieren. Wenn Versetzungskriechen und -klettern als typische Deformationsmechanismen von natürlichen Unterkrustengesteinen unter steady-state-Bedingungen angesehen werden, sollten Plastilin/Öl-Mischungen benutzt werden.

Drei verschiedene experimentelle Studien über die Deformation einer kompetenten Lage eingebettet in einer inkompetenten Matrix unter *koaxialen ebenen Verformungsbedingungen* wurden durchgeführt. In beiden Fällen war das undeformierte Modell (Matrix plus Lage) ein Würfel mit der Kantenlänge 12 cm. Sämtliche Experimente wurden bei einer Raumtemperatur $T = 25 \pm 1^\circ\text{C}$ und einer Strainrate $\dot{\epsilon} = 7.9 \times 10^{-6} \text{ s}^{-1}$ bis $1.7 \times 10^{-2} \text{ s}^{-1}$ durchgeführt, bis ein finiter Strain von 30- 40% erreicht war.

Ziel des ersten Experimentes war es, die Deformation einer kompetenten Lage senkrecht zur *Y*-Achse des finiten Strainellipsoids und die damit einhergehende Entwicklung von Falten und Boudins bei koaxialer, ebener Verformung zu simulieren.

Die verwendeten Plastilintypen *Becks Grün* (Matrix) und *Becks Schwarz* (kompetente Lage) haben einen Spannungsexponenten $n \approx 8$. Die effektive Viskosität η_I des Matrixplastilins wurde durch Hinzufügen unterschiedlicher Ölmengen zu Ursprungsplastilin verändert. Bei einer Strainrate $\dot{\epsilon}$ von 10^{-3} s^{-1} und einem finiten Strain e von 10% lag die effektive Viskosität der Matrix zwischen 1.2×10^6 und $7.2 \times 10^6 \text{ Pa s}$. Bei großem Viskositätskontrast zwischen kompetenter Lage und Matrix ($m > 20$) und geringer Dicke der kompetenten Lage entwickeln sich Falten und Boudins gleichzeitig. Obwohl die Wachstumsrate der Falten höher als die der Boudins zu sein scheint, sind die Wellenlänge beider Strukturen annähernd gleich, wie auch theoretische Ableitungen vermuten lassen. Dabei nimmt die Dicke der kompetenten Lage mit zunehmendem Strain signifikant zu. Diese Beobachtung erlaubt es, Falten und Boudins, die auf ebene Verformung zurückgeführt werden können, von konstruktionalen Falten und Boudins zu unterscheiden.

Im Rahmen der zweiten experimentellen Studie wurde die Auswirkung unterschiedlicher Strainraten bei ebener Verformung auf wachsende Falten und Boudins untersucht. Folgende Strainraten wurden angewendet: $7.9 \times 10^{-6} \text{ s}^{-1}$, $1.4 \times 10^{-5} \text{ s}^{-1}$, $2.7 \times 10^{-4} \text{ s}^{-1}$, $1.1 \times 10^{-3} \text{ s}^{-1}$, $1.1 \times 10^{-2} \text{ s}^{-1}$, $1.7 \times 10^{-2} \text{ s}^{-1}$. Die Matrix des Modells bestand aus *Becks Grün*-Plastilin, die kompetente Lage aus *Kolb Grau*-Plastilin. Beide Modellmaterialien verhalten sich

nichtlinearviskos (n_1 von *Becks Grün* = 7.9 und n_2 von *Kolb Grau* = 6.5). Die scheinbare Viskosität liegt bei 7.2×10^6 Pa s (η_1 , *Becks Grün*) und 8.5×10^6 (η_2 , *Kolb Grau*). Auch hier wurde die effektive Viskosität des Matrixplastilins durch Hinzufügen von Öl verändert. Mehrere Versuche mit unterschiedlicher Orientierung der kompetenten Lage (S) zu den Hauptstrainachsen ($X > Y > Z$) wurden durchgeführt. Die Ergebnisse lassen auf einen beachtlichen Einfluss der Strainrate auf die Geometrie der deformierten kompetenten Lage schließen. Dies gilt für jede Art der Schichtorientierung ($S \perp X$, $S \perp Y$, $S \perp Z$). Wenn die kompetente Lage senkrecht zur Z -Achse des finiten Strainellipsoids ausgerichtet ist, stellt man eine Zunahme der Boudinanzahl und der Dicke der kompetenten Lage fest, wohingegen die Länge der Boudins abnimmt. Wenn die kompetente Lage senkrecht zur X -Achse des finiten Strainellipsoids orientiert ist, führt die Erhöhung der Strainrate zu einer Zunahme der Faltenwellenlänge. Gleichzeitig nehmen Faltenanzahl und Verdickungsgrad der kompetenten Lage ab. Wenn die kompetente Lage senkrecht zur Y -Achse des finiten Strainellipsoids ausgerichtet ist, führt die Erhöhung der Strainrate zu einer Abnahme der Anzahl von Boudins und Falten. Gleichzeitig nimmt die Wellenlänge beider Strukturen zu. Die Wellenlänge der Falten ist ca. halb so groß wie die Wellenlänge der Boudins. Dies gilt sowohl für Fälle, wo Falten und Boudins sich gleichzeitig entwickeln ($S \perp Y$), als auch für Fälle, bei denen beide Strukturen sich unabhängig voneinander entwickeln (Falten mit $S \perp X$ und Boudins mit $S \perp Z$).

Im Rahmen der dritten experimentellen Studie wurden skalierte Analogexperimente durchgeführt, um die raumzeitliche Entwicklung von Falten und Boudins bei ebener Verformung zu zeigen. Alle bisherigen 3D-Studie auf diesem Feld basieren nur auf finiten Deformationsstrukturen. Ihre Ergebnisse können daher nicht benutzt werden, um zu beweisen, ob Falten und Boudins gleichzeitig oder nacheinander wachsen. Eine einzelne kompetente Lage (eingebettet in einer inkompetenten Matrix) wurde ebener Verformung ausgesetzt. Dabei war die kompetente Lage senkrecht zur Y -Achse des finiten Strainellipsoids

orientiert. Zwei unterschiedliche Experimente wurden durchgeführt und mit Computertomographie (CT) analysiert. Im ersten Experiment wurde ohne Unterbrechung von 0 – 40% Verkürzung deformiert. Während des zweiten Experimentes wurde die Deformation nach jeweils 10% des longitudinalen Strain gestoppt. Jedes Experiment wurde bei einer Raumtemperatur T von 25°C und einer Strainrate $\dot{\epsilon}$ von ca. $4 \times 10^{-3} \text{ s}^{-1}$ durchgeführt, bis ein finiter Strain von 40% erreicht war. Der Viskositätskontrast m betrug 18.6. Die Matrix des Modells bestand aus *Becks Grün*-Plastilin, die kompetente Lage aus *Kolb Braun*-Plastilin. Beide Modellmaterialien sind nichtlinearviskos (n_1 von *Becks Grün* = 10.9 und n_2 von *Kolb Braun* = 6.5). Die scheinbare Viskosität liegt bei $1.2 \times 10^6 \text{ Pa s}$ (η_1 , *Becks Grün*) und 2.23×10^7 (η_2 , *Kolb Braun*). Die neuen Daten belegen, dass sich Falten und Boudins unter ebener koaxialer Deformation gleichzeitig bilden, wenn die kompetente Lage senkrecht zur Y -Achse des finiten Strainellipsoids orientiert ist. Die Ergebnisse sind für all jene von Interesse, die sich mit ebener Verformung und der Bildung von Boudins und Falten beschäftigen, wobei die Faltenachsen parallel zur X -Achse des finiten Strainellipsoids liegen.

Wie in der ersten experimentellen Studie demonstriert wurde, sind Faltung und Boudinage unter ebener Verformung mit einer bedeutenden Zunahme der Dicke der kompetenten Lage verbunden. Dieses Phänomen tritt nicht in anderen Fällen gleichzeitiger Faltung und Boudinage auf, wie z.B. reiner Konstriktion. Um den Einfluß der Lagenmächtigkeit auf die Geometrie von Falten und Boudins bei reiner Konstriktion zu studieren, wurden zusätzliche Experimente mit unterschiedlichen Plastilintypen durchgeführt. Lage und Matrix durchliefen reine Konstriktion, wobei die kompetente Lage parallel zur X -Achse des finiten Strainellipsoids orientiert war. Die Deformationsgeometrie der kompetenten Lage ist mit Schnitten entlang YZ und $XY=XZ$ untersucht worden. Die kompetente Lage und die Matrix bestehen aus nichtlinearviskosem *Kolb Braun*-Plastilin und *Becks Grün*-Plastilin. Beides sind „strain softening“ Materialien. Sechs Experimente sind mit Mächtigkeiten der steifen Lage von 1, 2, 4, 6, 8 und $10 \pm 0.2 \text{ mm}$ durchgeführt worden. Alle Experimente wurden bei einer

Raumtemperatur T von 30 ± 2 °C und bei einer Strainrate von ca. $1.1 \times 10^{-4} \text{ s}^{-1}$ durchgeführt, bis ein finiter Strain von 40% erzielt war (Viskositätskontrast m zwischen kompetenter Lage (*Kolb Braun Plastilin*) und Matrix (*Becks Grün Plastilin*) von 3.1). Für die kompetente Lage ist die scheinbare Viskosität, $\eta = 2.23 \times 10^7 \text{ Pa s}$ und der Spannungsexponenten, $n = 5.8$; für die Matrix $7.2 \times 10^6 \text{ Pa s}$ und 7.9 bei einer Strainrate $\dot{\epsilon}$ von ca. 10^{-3} s^{-1} und einem finiten Strain $e = 10\%$. Unsere Ergebnisse zeigen einen beträchtlichen Einfluss der Ausgangsdicke der kompetenten Lage auf die Geometrie der verformten Lage. Es gibt keinen Beweis dafür, dass Faltung in den $XY=YZ$ Schnitten stattfindet, wenn die Ausgangsdicke der kompetenten Lage größer als ca. 8 mm ist. Wenn die Ausgangsdicke der kompetenten Lage 10 ± 0.2 mm beträgt, entwickeln sich Falten und Boudins gleichzeitig. Die Wachstumsrate der Boudins scheint jedoch höher als die Wachstumsrate der Falten zu sein. Ein weiterer charakteristischer Aspekt der verformten kompetenten Lage ist, dass keine Änderung der Dicke der kompetenten Schicht stattfindet. Dieses Phänomen kann verwendet werden, um gleichzeitig gebildete ebene Falten und Boudins (mit $S \perp Y$) von konstruktionalen Falten und Boudins zu unterscheiden. Die Ergebnisse des Modells sind für die Analyse und die Deutung von Deformationsstrukturen in rheologisch geschichteten Gesteinen wichtig, die Versetzungskriechen bei reiner Konstriktion durchlaufen. Tektonische Settings, in denen sich konstruktional Falten und Boudins gleichzeitig entwickeln, sind Stämme von Salzdiapiren, Subduktionzonen oder Mantelplumes.

Um paläoviskosimetrische Aussagen machen zu können, wurde die Plastilinrheologie mit der Geometrie der erzielten Strukturen in Beziehung gesetzt. Vergleicht man die normalisierten dominanten Wellenlänge W_d der deformierten Lage mit der aus der Smith-Gleichung (1977, 1979) errechneten theoretischen dominanten Wellenlänge (L_d), so wird klar, dass die Smith-Gleichung auch für die Fälle gilt, in denen Falten und Boudins sich gleichzeitig entwickeln ($S \perp Y$) sowie für den Fall, wo Boudins sich unabhängig entwickeln ($S \perp Z$). Die vorgestellten

Experimente bestätigen damit die Gleichung von Smith. Vorsicht ist jedoch geboten bei sehr niedrigen Viskositätskontrasten zwischen Lage und Matrix.

Experimente bestätigen damit die Gleichung von Smith. Vorsicht ist jedoch geboten bei sehr niedrigen Viskositätskontrasten zwischen Lage und Matrix.

TABLE OF CONTENTS

ACKNOWLEDGEMENTS	I
ABSTRACT	III
ZUSAMMENFASSUNG	IX
TABLE OF CONTENTS	XV
1 INTRODUCTION	1
1.1 General background	1
1.2 Problem definition	2
1.3 Aims of the study	4
2 BACKGROUND TO FOLDING AND BOUDINAGING	7
2.1 Definition and importance of folding for geology	7
2.2 Definition and importance of boudinaging for geology	9
2.3 Previous studies	11
2.3.1 Analytical approaches to the formation of folds and boudins	11
2.3.1.1 Folding of a Newtonian layer embedded in a Newtonian matrix	13
2.3.1.2 Folding and boudinage of a non-Newtonian layer	15
2.3.2 Analogue and numerical experiments on buckle folding	17
2.3.3 Analogue models of boudinage	23
3 EXPERIMENTAL APPROACHES	27
3.1 Scaling procedure	27
3.2 Plasticine as analogue material	29
3.2.1 Rheological measurements	31
3.2.1.1 Sample preparation	31
3.2.1.2 Uniaxial compression tests	32
3.2.1.3 Stress exponents	34
3.2.1.4 Apparent viscosity	36

3.3	Analogue modelling of geological structures	36
3.3.1	Deformation apparatus	36
3.3.2	The experimental procedure	39
3.4	Computer Tomography (CT)	40
3.4.1	Introduction	40
3.4.2	Visualization of the CT-data	43
3.4.3	Evaluation of the CT-data	44
4	EXPERIMENTAL RESULTS	47
4.1	Rheology of plasticine used for experiments	47
4.2	Coeval folding and boudinage under plane strain with the axis of no change perpendicular to the layer	50
4.3	The impact of strain rate on folding and boudinage under plane strain	56
4.3.1	Stiff layer perpendicular to the long axis of the finite strain ellipsoid ($S \perp X$)	57
4.3.2	Stiff layer perpendicular to the short axis of the finite strain ellipsoid ($S \perp Z$)	60
4.3.3	Stiff layer perpendicular to the intermediate axis of the finite strain ellipsoid ($S \perp Y$)	64
4.4	Coeval folding and boudinage under plane strain through space and time	67
4.5	Coeval folding and boudinage under pure constriction with the X -axis parallel to the layer	70
5	DISCUSSION	75
5.1	Rheological data	75
5.2	Coeval folding and boudinage under plane strain with the axis of no change perpendicular to the layer	76
5.3	The impact of strain rate on folding and boudinage under plane strain	81
5.4	Coeval folding and boudinage under pure constriction with the X -axis parallel to the layer	85
6	CONCLUSIONS AND OPEN QUESTIONS	87
7	REFERENCES	91
	LIST OF ABBREVIATIONS	107
	CURRICULUM VITAE	109

1 INTRODUCTION

1.1 General background

The study of folds and boudins is a problem of first importance to understand the temporal evolution of geological structures. Folds and boudins can give information about relative plasticity and relative strength of rocks during deformation. They therefore provide an excellent key to the forces involved in deformation of rocks and the rheological characteristics of rocks, their strength and viscosity. Investigations of folding and boudinage in the light of the known behaviour of other unstable systems is therefore of primary importance not only for the interpretation of geological processes, but also for large-scale geophysical interpretations of flow strengths and dynamics of the continental crust. Thus, it may be possible to provide a useful link between experimental, theoretical and field data.

One possible approach to study the influence of the deformation regime on the geometry of geological structures like folds and boudins is to perform experimental deformation using rock analogues. The latter have been used since the beginning of the 19th century to provide qualitative insights into specific geological problems (Schellart, 2002). The aim of such experiments is to activate the same processes that occur in nature, but under scaled and well-constrained conditions. The analogue modelling offers two advantages: it makes it possible to observe easily the origin, operation and interaction of the structures related to flexible tectonics like their influence at once of displacements. It allows the analysis of finished deformations of great width. The object is not more to solve by calculation a formulated problem in a mathematic way but to reproduce in laboratory a phenomenon by simulating on a model a certain number of conditions necessary to its realization. In this study we have mainly tried to model development of small-scale structures that can be used as kinematics' indicators in studies of large-scale tectonics. In future, this should be integrated into large-scale tectonic reconstructions and inversion modelling. Since the experimental technique can

be readily applied to offer solutions for three-dimensional problems involving large strains, it can offer invaluable new insights into geological problems, which are intrinsically three-dimensional and often involve large amounts of strain.

1.2 Problem definition

Deformation processes in rocks are difficult to model experimentally. The very slow deformation processes in rocks, and the large scale of many structures such as folds, boudins, mullions and thrusts cannot be reproduced in the laboratory. Geologists therefore have to restrict themselves to observational science, like in archaeology, or apply “tricks” to learn something in the laboratory through modelling studies. Modelling studies can be undertaken as high-pressure experiments on small samples to learn about rheology, by using analogue materials as a substitute for rocks to learn about development of small-scale structures; or by numerical experiments modelling small or large-scale processes. Although the structure seems simple at first approach, there are many small-scale structures that remain ambiguous, but which contain potentially important information on the kinematics’ development of the area.

A single layer embedded in a less viscous matrix will deform heterogeneously if shortened parallel or perpendicular to the layering and folds or boudins will form, respectively. However, various orientations of the layer can lead to formation of folds and/or boudins under oblate, plane and constrictional conditions. The pictures that could possibly develop within these deformation regimes are depicted in the schematic drawings of Zulauf et al. (2003, see also Weijermars, 1997). It is clear that folds and boudins will form synchronously whenever the stretching direction X is parallel to the fold axes and the intermediate axis of the strain ellipsoid Y is perpendicular to the axial plane. Most experiments found in the literature have been carried out under *plane-strain conditions* with the stiff layer oriented either perpendicular to the long axis X or perpendicular to the short axis Z of the finite strain

ellipsoid (Figs. 1.1a,b). Most of these models imply plane-strain conditions, with the length of the intermediate Y -axis of the finite strain ellipsoid kept constant. However, the finite strain of many natural tectonites deviates significantly from plane strain (e.g. Pfiffner and Ramsay, 1982). Naturally deformed rocks may consist of L , $L > S$, $S > L$, or S tectonites, where the longitudinal strain e along the Y -axis deviates from zero. However, the origin of L and $L > S$ tectonites in particular has been hardly verified by experiments.

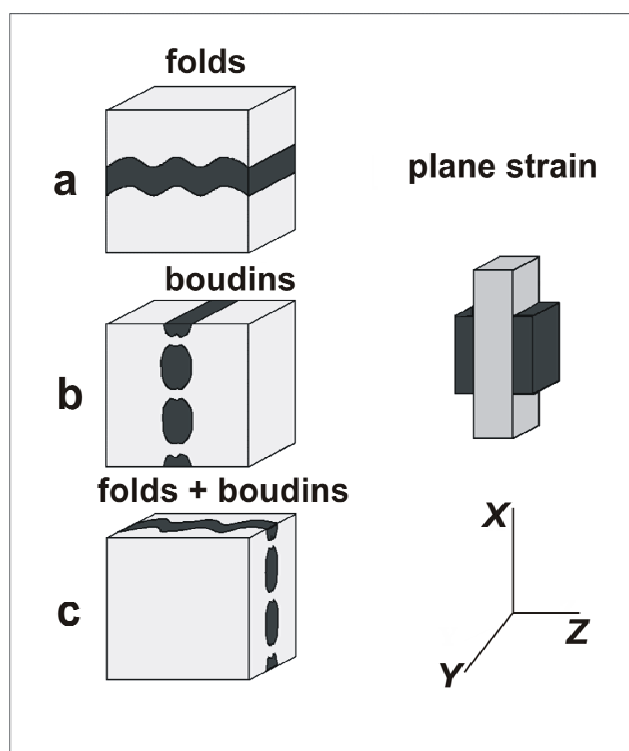


Fig. 1.1: Principal effect of a stiff layer orientation in reference to the axes of finite plane strain (after Zulauf et al., 2003).

Moreover, largely unknown are the structures of *the constrictional regime*, where folds and boudins should develop simultaneously if a stiff layer is embedded in a matrix with the X -axis parallel to the layer, although $S > L$ - and $L > S$ tectonites are common in the nature (Fig. 1.2). Results of theoretical studies (Ramberg, 1959, Fig. 7; Ramsay, 1967; Talbot and Sokoutis, 1995; Weijermars, 1997; Fig. 14.24) and analogue scale-model experiments (Kobberger and Zulauf, 1995; Zulauf et al., 2003; Zulauf and Zulauf, 2005) suggest that both folds and

boudins may grow under constriction. We present new data, which continue the investigations of Zulauf et al. (2003) and Zulauf and Zulauf (2005).

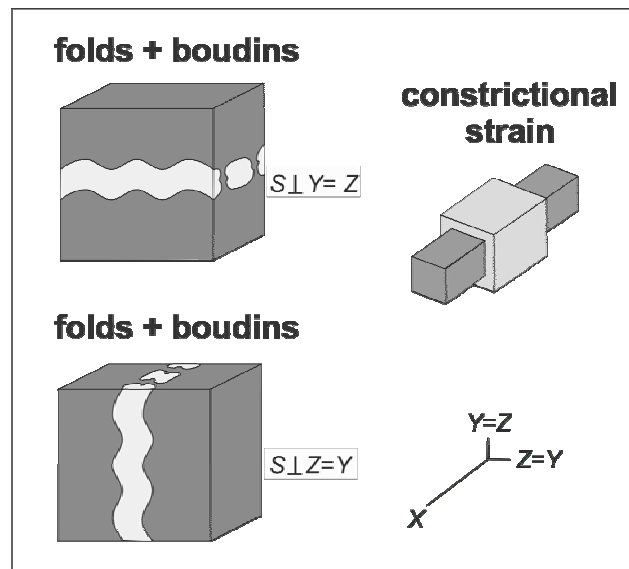


Fig. 1.2: Principal effect of a stiff layer orientation in reference to the axes of finite constrictional strain (after Zulauf et al., 2003).

1.3 Aims of the study

There is a need for analogue modelling of geological structures (folds, boudins) in mechanically stratified material under *plane-strain conditions* with the axis of no change perpendicular to the stiff layer (Fig. 1.1c). The geometry of the instabilities should be compared to predictions arising from analytical solutions. The thickness of the deformed competent layer and the rheology of matrix and layer are generally believed to be important for the geometry of the instabilities (e.g., Watkinson, 1975; Zulauf et al., 2003). Apart from these basic parameters, the impact of varying stress exponents, strain rates, and orientation of the layer has been investigated in detail in the present study. The experiments of the present thesis have been carried out using a new deformation apparatus that can produce the full range of three-dimensional coaxial deformation, from pure constriction via plane strain to pure flattening (Zulauf et al., 2003).

Three different experimental studies of plane-strain coaxial deformation of a single stiff layer, with viscosity η_2 and stress exponent n_2 , that is embedded in a weak matrix, with viscosity η_1 and stress exponent n_1 , have been carried out. In all experimental studies the undeformed samples (matrix plus layer) were cubes with an edge length of 12 cm. All experimental runs have been carried out at $T = 25 \pm 1^\circ\text{C}$ and varying strain rates $\dot{\epsilon}$, ranging from $7.9 \times 10^{-6} \text{ s}^{-1}$ to $1.7 \times 10^{-2} \text{ s}^{-1}$, until a finite longitudinal strain of 30% – 40% was achieved.

The first experimental study has been carried out to improve our understanding about the impact of layer thickness and viscosity contrast between layer and matrix on the evolution of folds and boudins when the layer is oriented perpendicular to the Y -axis of the finite strain ellipsoid. The rock analogues used were *Beck's green* plasticine (matrix) and *Beck's black* plasticine (competent layer), both of which are strain-rate softening modelling materials with stress exponent $n = \text{ca. } 8$. The effective viscosity η of the matrix plasticine was changed by adding different amounts of oil to the original plasticine. The geometry of the instabilities will be presented and compared with predictions rising from analytical solutions.

In the second experimental study, the impact of varying strain rates on growing folds and boudins under plane strain have been investigated. The stiff layer and matrix consist of non-linear viscous *Kolb grey* and *Beck's green* plasticine, respectively. Different runs have been carried out where the layer was oriented perpendicular to the principal strain axes ($X > Y > Z$).

In the third experimental study, the impact of plane strain on the deformation structures of rheologically stratified analogue material was investigated in 4D. Plane strain acted on a single stiff layer that was embedded in a weak matrix, with the layer oriented perpendicular to the intermediate Y -axis of the finite strain ellipsoid. Two different experimental runs have been carried out using computer tomography (CT) to analyze the results. The first run was carried out without interruption. During the second run, the deformation was stopped in each case at longitudinal strain increments of 10%.

During the fourth experimental study the impact of layer thickness on the geometry of folds and boudins under pure constriction has been studied with the initially planar layer oriented parallel to the X -axis of the finite strain ellipsoid. The stiff layer and matrix consist of non-linear viscous *Kolb brown* and *Beck's green* plasticine, respectively. The deformation geometry of the layer has been investigated using conventional cuts along YZ and $XY=XZ$.

2 BACKGROUND TO FOLDING AND BOUDINAGING

2.1 Definition and importance of folding for geology

Folds are perhaps the commonest and most obvious manifestation of deformation in layered or foliated rocks. The study of fold development is, therefore, fundamental to understanding orogenesis (Mancktelow and Abbassi, 1992). In nature, rock units often exhibit planar features and show a layered structure. Compression or shortening parallel to the planar surfaces can cause a deflection of one or several layers in a direction orthogonal to the planar surfaces (Fig. 2.1).

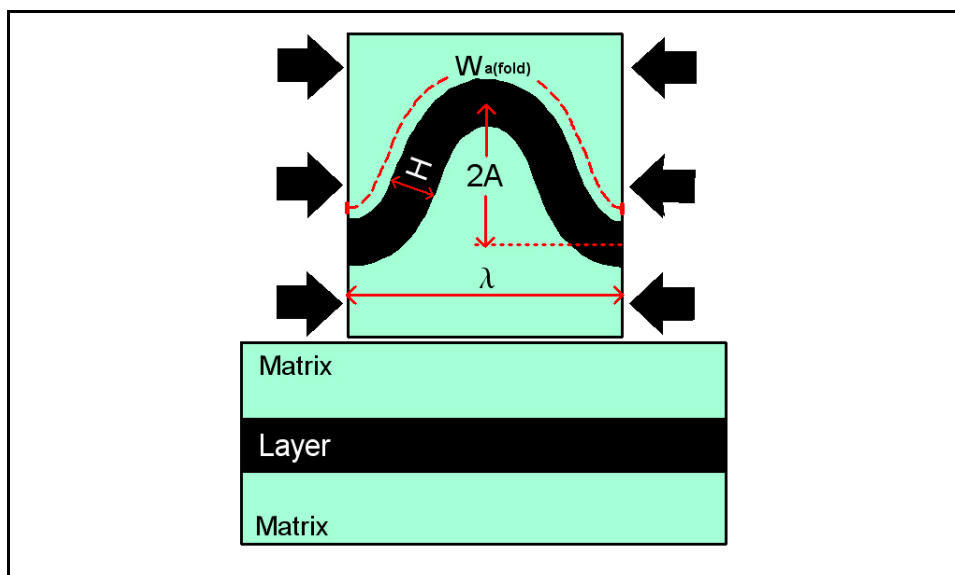


Fig. 2.1: Schematic two-dimensional model of single layer buckling. Due to compression or shortening, the initially flat layer deflects in a direction orthogonal to the shortening direction. The geometry of a folded layer is characterized by the wavelength (λ), amplitude (A), layer thickness (H), and average fold arclength ($W_{a(fold)}$) in YZ- sections (after Schmalholz, 2000).

This mechanical process is termed buckling (e.g., Biot, 1961; Ramberg, 1961; Chapple, 1968; Johnson and Fletcher, 1994). The resulting structures are, in general, termed folds (e.g., Ramsay and Huber, 1987). If only one layer is folded, one speaks of single-layer folding (Fig. 2.2); if several layers are folded one speaks of multilayer folding (Fig. 2.3).



Fig. 2.2: Example of single-layer ptygmatic folds of a granite dyke within a gneissic granite, representing probably late-orogenic intrusions of the Svecofennian orogenesis (1.83 – 1.8 Ga); Åva/Brändö, northeastern part of the Åland archipelago in the Baltic Sea southwest of Finland (copyright of C.Dietl, 07/05).



Fig. 2.3: Multilayer folding of a Jurassic chert-limestone sequence of the Pindos unit of southern Crete (Agios Pavlos).

The lithosphere, itself a layer, exhibits numerous planar features on different scales. On a large scale, it may be divided into the upper and lower crust and upper mantle. On a smaller scale, planar features are sedimentary bedding or metamorphic layering. On the microscale, planar foliations are present. Therefore, folding frequently occurs during deformation of the lithosphere on all scales.

In general, the stress state and distribution within rock units is strongly controlled by folding. A considerable perturbation on any initial stress state can be present even if fold amplitudes and overall shortening are small. The initiation and spacing of thrusts and shear zones can be

strongly affected by the folding process and subsequent stress field. Folding-controlled distribution of high and low pressure areas may control the migration of fluids and eventual crystallisation of mineral resources. Weak zones in rocks, such as areas with strong schistosity, are often generated through folding, and locating of these weak zones is important in Engineering Geology (e.g., when building tunnels). Therefore, the understanding of the mechanical process of folding is a key step to understand lithosphere deformation in general and e.g., mountain building in particular.

2.2 Definition and importance of boudinaging for geology

Boudinage structures, first described by Ramsay (1866) and Harker (1889), and named by Lohest (1909), when it was coined by geologists in Belgium to describe certain structures in metamorphosed layered sandstones and shales, are common extensional features, especially in rocks with a layering of contrasting lithologies (Quirke, 1923; Whitten, 1966; Price and Cosgrove, 1990). The shape of the separated bodies, i.e. the boudins, occur as a subdivision of a planar volume of rock by regularly spaced veins or zones of enhanced deformation, the interboudin zones or boudin necks. This planar rock volume can be a layer, group of parallel layers or simply a domain of foliated rock, apparently showing no competence contrast (Coe, 1959; Platt and Vissers, 1980; Passchier and Druguet, 2002). The development of foliation boudins is attributed to the presence of pre-existing fractures (Platt and Vissers, 1980; Mandal and Karmakar, 1989) or interlocking pinching-and-swelling instability (Cobbold et al., 1971). In three-dimensions, most boudins occur as long tabular strips separated by boudin necks. However, if deformation deviates from plane strain, more complex shapes such as chocolate tablet boudinage, with rectangular or approximately cylindrical shaped boudins, may develop (Fig. 2.4).

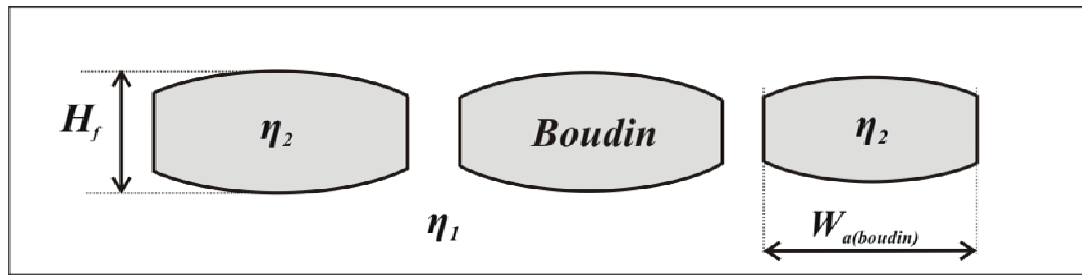


Fig. 2.4: Terminology and measurable parameters used to describe idealized late stage of boudinage of a stiff layer embedded in a weak matrix. H_f = maximum boudin thickness; $W_{a(boudin)}$ = boudin length; η_1 = matrix viscosity and η_2 = layer viscosity.

Similar structures were described earlier by several other authors, for example, by MacCulloch (1816, Plate 15) in Glen Tilt, Central Scottish Highlands. For further references and reviews of the historical aspects see Cloos (1947) or Ramberg (1955) and Whitten (1966). In cross-section normal to the boudinaged planar volume of rock and the boudin necks, individual boudins occur in a range of shapes (Passchier and Druguet, 2002). The shape of the boudins may vary from rectangular to lens-shaped depending on the competence contrast and arranged in a linear train of orthorhombic symmetry but there are also some, especially in ductile shear zones, with parallelogram-shaped cross-sections and/or relative displacement on the interboudin popularly known as asymmetric boudins (Passchier and Druguet, 2002; Figs. 1 and 2a).

The rheological behaviour of the competent layer might vary from brittle to ductile failure, whereas the matrix reacts by viscous flow. Brittle boudins result from extensional or shear failure of the competent beds. In the latter case the boudins are often asymmetrical; such boudins have a monoclinic- or triclinic symmetry and their geometry suggests that they carry information on the rotational component of progressive deformation, and could act as shear sense indicators (Hanmer, 1986; Gaudemer and Tapponier, 1987; Malavieille, 1987; Marcoux et al., 1987; Goldstein, 1988; Malavieille and Lacassin, 1988; Hanmer and Passchier, 1991).

The geological importance of boudinage structures is not less than that of folding or faulting and their role in providing understanding of the character and development of geological

processes is often significantly greater due to a number of specific features of these structures (Tokhtuev, 1967). Thus only detailed systematic study of boudinage structures as well as other structural features (and often in preference to all other structural features, especially in metamorphic complexes), gives us an opportunity to obtain additional data for the solving of many important problems of tectogenesis, metamorphism and mineralization. Knowledge of the features of morphology of boudinage structures and of the regularity of their spatial distribution facilitates more effective management and execution of mineral exploration and geophysical surveys (Tokhtuev, 1967; and references therein). This constitutes the great practical value of the study of boudinage structures.

2.3 Previous studies

2.3.1 Analytical approaches to the formation of folds and boudins

The collapse of deformable structures under stress has fascinated scientists and engineers since 1744 when Euler present his linear stability analysis of the large-scale structural failure of plates, known as the buckling instability (Landau and Lifshitz, 1970). Since then many studies have been devoted to the description of buckle folds. Bazant and Cedolin (1991) noticed that failure of compressed layers can be split into two categories: (i) material failure which can be investigated using equilibrium equations that are derived for the undeformed configuration of the layer, and (ii) structural instabilities which in contrast with the first category require equilibrium equations that are derived for the deformed configuration of the layer. Buckling is one of the fundamental prototypes of structural stability problems. According to Schmalholz (2000), Euler (1744) was probably the first who solved the first buckling problem. At his time, the classical bending theories assumed that the bending strain ε is proportional to the curvature of the beam (Bernoulli-Navier hypothesis):

$$\varepsilon = \frac{y}{r} \quad [2-1]$$

where y and r are the transverse coordinate measured from the middle line of the beam and r is the radius of curvature of the beam (Fig. 2.5).

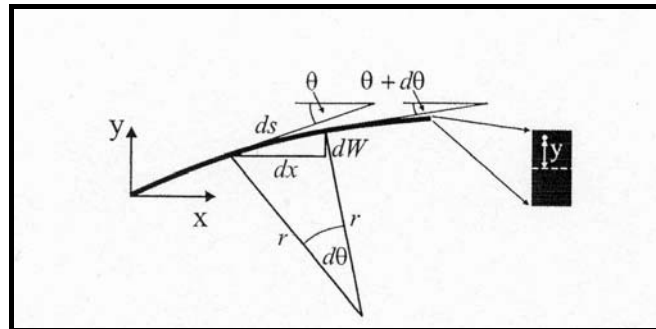


Fig. 2.5: Geometry of the deflected beam. r = radius of curvature; ds = the infinitesimal segment of the arc length; θ = angle between the x -axes and the tangent to a point on the beam; dW = the infinitesimal vertical deflection; and y = the vertical distance from the beam's middle line to a point above the middle line (after Schmalholz, 2000).

With this work, he laid the foundation for the development of the general thin-plate theories of buckling (e.g. Timoshenko and Woinowsky-Krieger, 1959) that are widely used to study folding problems. The major difference between the Euler beam and natural folds is that the Euler beam is free whereas folded layers are embedded in materials weaker than the layers. Smoluchowski (1909a) apparently performed the first analytical investigation of buckling of an elastic plate lying on top of a fluid. He verified his analytical solution by experiments, performed with various elastic materials (e.g. gelatine solution) floating on a viscous fluid (e.g. mercury) (Smoluchowski, 1909b). It should be noted that in the middle of the last century, a number of studies verified Smoluchowski's buckling theory using thin-plate theories. Thereby, folding of either pure elastic or pure viscous single-layers embedded in a pure elastic or pure viscous infinite matrix is studied (e.g. Biot, 1961; Sherwin and Chapple, 1968; Ramberg, 1959; Smith, 1975, 1977; Fletcher, 1977, 1991). The initial shape of the folded layers is assumed to be sinusoidal and the growth of the amplitude is assumed to be exponential with time. The most important result of these studies is the identification of a maximum amplification rate for a certain ratio of wavelength to thickness of the single layer, which is designated the dominant wavelength. A layer perturbation that exhibits this dominant

wavelength grows exponentially faster than all other layer perturbations, and it has presumably selected and locked at the nucleation stage.

2.3.1.1 *Folding of a Newtonian layer embedded in a Newtonian matrix*

In the case of a viscous single layer embedded in an infinite viscous matrix, Biot (1961) derived the expression for the dominant wavelength λ_d based on plate theory:

$$\frac{\lambda_d}{H} = 2\pi \sqrt[3]{\frac{1}{6} \frac{\eta_2}{\eta_1}} \quad [2-2]$$

where H , η_2 and η_1 are the thickness of the layer, the viscosity of the layer and the viscosity of the matrix, respectively. The “viscous” dominant wavelength only depends on the viscosity contrast between layer and matrix and is independent of the layer-parallel stress or shortening rate. He noted that, in contrast to the case of an elastic plate, the dominant wavelength is independent of the compressive load. He additionally treated the folding of a stack of α layers with perfect slip and viscosity η_2 and found that the dominant wavelength is

$$\frac{\lambda_d}{H} = 2\pi \sqrt[3]{\frac{\alpha\eta_2}{6\eta_1}} \quad [2-3]$$

The result is striking: a single layer with viscosity η_2 and thickness H will have a smaller wavelength than a multilayer with the same thickness.

Ramberg (1959) presented an equation quite similar to that derived by Biot [2-2], except that the constant ‘six’ in the denominator of equation was replaced by an undetermined constant. He was unsure how to treat the effect of matrix, but two years later, he showed that this equation is a first-order approximation to his solution.

Sherwin and Chapple (1968) studied the influence of layer thickness on the dominant wavelength. They collected numerous hand samples containing folded quartz veins in phyllitic or sandy matrix and calculated the average arc wavelength by dividing the total arc

length by the number of folds (see equation 2-7). The mean relative wavelengths were 4.0 to 6.8, and the viscosity ratios between layer and matrix were calculated to be 2 to 8, which are too low for the Biot theory. Thus, they extended the Biot theory and considered layer parallel shortening. The dominant wavelength of the final fold is

$$\frac{\lambda_d}{H} = 2\pi \sqrt[3]{\frac{\eta_2}{6\eta_1} \frac{1 + \lambda}{2\lambda^2}} \quad [2-4]$$

where λ is the uniform, finite elongation related to fold growth. With this equation, they calculated the viscosity ratio to be in the range of 16 to 21. In addition, dominant wavelength expressions were derived for single layers and matrices exhibiting power-law rheology (e.g. Smith, 1975; Fletcher, 1977, 1991).

Smith (1975) presented a “unified theory on the onset of folding, boudinage and mullion structure” based on hydrodynamics. He distinguished a basic state of flow driven by the overall stress and a perturbing (secondary) flow, due to the inclination of the layer/matrix interface. The shift of the interface results from both types of flows. However, absolute growth will only occur, if the total growth rate is positive. In cases of Newtonian materials, only folds can compete the kinematics’ decay (Fig. 2.6).

Fletcher (1977) derived the same solution for the folding instability like Smith (1975) in a slightly way. Nevertheless, these theoretical studies have shown that Ramberg and Biot’s solutions are wrong, especially for low viscosity ratios (Fig. 2.7) and for high viscosity ratios; the solutions of Ramberg and Biot predict nearly the same dominant wavelength.

Later (Fletcher, 1991) extended the analytical solution for folding of a Newtonian layer for the three-dimensional case. For this general solution, a toroidal flow is required to satisfy the boundary conditions. The poloidal flow determines the rate of fold growth. He also stated that a cylindrical fold, with axis normal to the direction of maximum shortening in the plane of the layer would grow most rapidly.

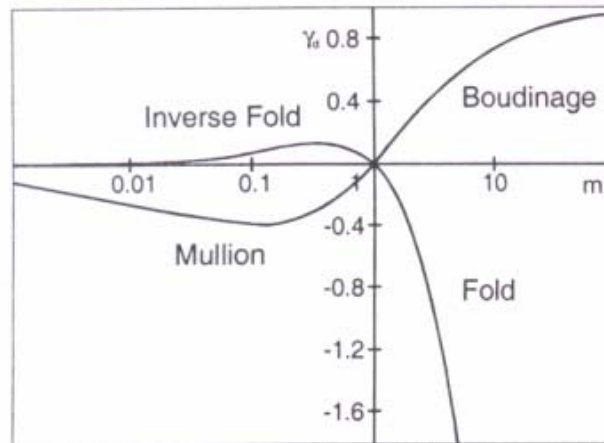


Fig. 2.6: Smith's (1975) plot of normalized dynamic growth rate γ_d vs. viscosity ratio $m = \eta_2/\eta_1$. Growth rates result from secondary flow. Negative γ_d indicates layer parallel shortening, positive γ_d layer parallel lengthening for the formation of the instability.

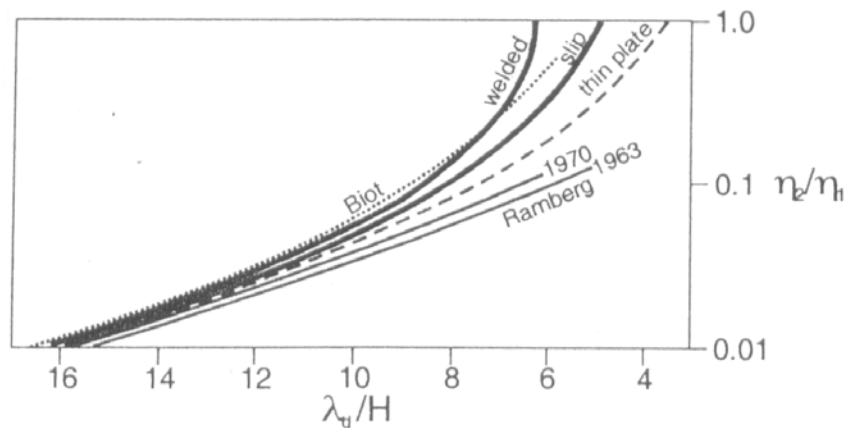


Fig. 2.7: Fletcher's (1977) plot of dominant wavelength vs. viscosity ratio ($m = \eta_2/\eta_1$) and his "exact" thick plate solution for folding with and without interfacial slip (bold line, 1977; Fig. 3). For comparison Ramberg's solution (thin line) for folding with interfacial adherence (1962) and slip along the interface (1970), Biot's (dotted line, 1961) thick plate solution for folding with interfacial slip and the thin plate solution (dashed line, equation [2-1]).

2.3.1.2 Folding and boudinage of a non-Newtonian layer

Most of the theoretical models based on linear viscous or elastic materials can only predict the growth rates and spacing of folds along a train in the initial stages of deformation (Ramberg, 1960; Biot, 1961; Sherwin and Chapple, 1968). There are some theories available to make predictions of folds growth and shape to significant amplitudes. Thus, Fletcher (1974) and Smith (1977) showed that quantitative agreement between theory and the observed folds requires using a non-Newtonian model. Fletcher (1974) developed the theory to third order

and derived linearized constitutive relations for an incompressible power-law fluid to show that the rheology of a limestone layer embedded in shale was strongly nonlinear in folding. He presented the first analytical solution for folding of a single layer with power-law rheology embedded in a matrix with power-law rheology:

$$\frac{\lambda_d}{H} \cong \frac{2\pi}{\sqrt[3]{6R}} \quad [2-5]$$

where $\mathbf{R} = n_2 \mathbf{Q}$, and $\mathbf{Q} = \sqrt{\frac{n_2 \eta_2}{n_1 \eta_1}}$

Smith's theory is more general, does not depend on any specific rheology, and takes account of non-Newtonian materials. The normalised dominant wavelength of a non-Newtonian layer embedded in a non-Newtonian matrix for both folding and boudinage is defined by the following equation (Fletcher, 1974; Smith, 1977, 1979):

$$L_d = \frac{\lambda_d}{H} = 3.46 \frac{n_1^{\frac{1}{6}} m^{\frac{1}{3}}}{n_2^{\frac{1}{3}}} \quad [2-6]$$

where L_d is the theoretical wavelength/thickness ratio, n_1 , η_1 and n_2 , η_2 are the stress exponents and the effective viscosities in the flow laws for matrix and layer, respectively, λ_d is the dominant wavelength, H is the layer thickness, and m is the viscosity contrast m of layer and matrix ($m = \eta_2/\eta_1$). Enlargement of m results in an increasing theoretical wavelength/thickness ratio (Fig. 2.8).

Fig. 2.8 is a plot of equation [2-6]. Substituting the measured values of the stress exponents and the effective viscosities into equation [2-6], the dominant wavelength/thickness, L_d found should be similar to the values calculated for the average arc length of folds/thickness ratio ($W_{d(fold)}$) and the average boudin wavelength/thickness ratio ($W_{d(boudin)}$).

The average arc length of folds ($W_{a(fold)}$) was calculated by the equation:

$$W_{a(fold)} = \text{total arc length}/n_{folds} \quad [2-7]$$

where n_{folds} is the number of folds in YZ-sections (Sherwin and Chapple 1968; Fletcher and Sherwin 1978). Given that the layer thickness does not significantly change during folding, this average arc length ($W_{a(fold)}$) is nearly the same as the average initial wavelength (Ramsay and Huber 1987, p. 383).

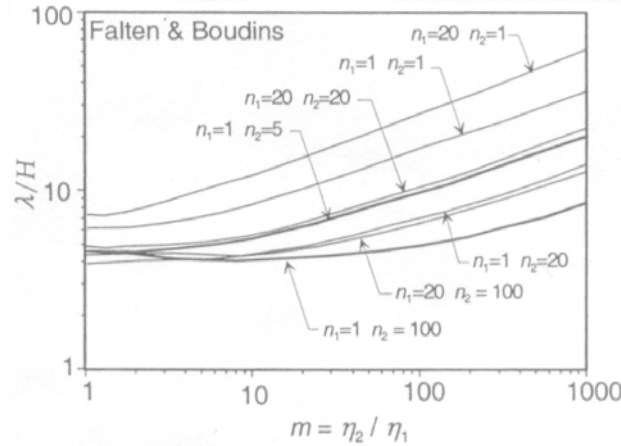


Fig. 2.8: Theoretical wavelength/thickness ratio ($\lambda d/H$) for folding and boudinage vs. viscosity contrast of layer and matrix m ($m = \eta_2/\eta_1$), where n_1 , η_1 and n_2 , η_2 are the stress exponents and the effective viscosities in the flow laws for matrix and layer, respectively (after Smith, 1977).

To compare the theoretical value (L_d) with the average arc length of folds ($W_{a(fold)}$) or average boudin wavelength ($W_{a(boudin)}$) measured in the experiments, we normalized the initial wavelength of the structures with the following equations:

$$W_{d(fold)} = W_{a(fold)}/H_f \quad [2-8]$$

$$W_{d(boudin)} = W_{a(boudin)}/H_f \quad [2-9]$$

where $W_{d(fold)}$ and $W_{d(boudin)}$ are the normalized dominant wavelength of folds and boudins, respectively, and H_f is the finite thickness.

2.3.2 Analogue and numerical experiments on buckle folding

The study of geological structures requires the knowledge of the mechanism that creates them. The folding process has been investigated by a number of researchers, following the pioneering work by James Hall (1815) and Bailey Willis (1891 – 1892), and using both

deformable materials and mathematical treatments. Probably Sir James Hall (1815) presented the first documentation of an analogue experiment to simulate a geological process in the Transactions of the Royal Society of Edinburgh. Here, he described his first attempts to model folding in geological strata, as he had observed in a belt of deformed Silurian clastic rocks that run across the southern Uplands of Scotland from Galloway to Berwickshire. Two experiments were performed. In the first experiment, several pieces of cloth, linen and woollen fabric were spread out on a table, one above the other. A flat door was put on top of the layered stack, being loaded with weights, to confine the stack. Next, two boards were applied to the sides of the stratified mass and were subsequently forced towards each other. This resulted in the gradual uplift of the heavy door, while the strata were constrained and adopted upward and downward bending folds. In the second experiment, beds of clay confined in a box were subjected to lateral compression due to the movement of movable ends driven by screw jacks, which is basically the same experimental design as is still in use today for fold- and thrust-type experiments. This experiment resulted in the generation of folds in the strata. The similarity between the folds reproduced in the experiments and folds observed in natural strata led the author to conclude that folds observed in nature must have a similar origin as in the experiment and therefore are the result of horizontal compression. Thereby, he further recognized the mechanism of layer thickening during layer-parallel compression.

Bailey Willis (1891 – 1892) conducted layer-parallel shortening experiments with various wax mixtures (beeswax, beeswax plus plaster of Paris to harden it, beeswax plus Venice turpentine to soften it) and compared his results with the geometry and lateral distribution of folds in the Appalachians. He loaded the wax with slot in order to simulate the overburden pressure. Willis varied the viscosity of the “stratified beds” also laterally in order to model facies changes.

Ramberg (1959, 1961) and Biot et al. (1961) made analytical approaches. Ramberg (1959) investigated the evolution of ptygmatic folding and used putty and plasticine to simulate the incompetent and competent veins, respectively. The stiff layer was deformed in simple and pure shear under plane-strain conditions. Additionally he performed experiments with rubber sheets in order to investigate the contact strain adjacent to the deformed layer (Ramberg, 1961). As for Biot et al. (1961), he conducted plane strain tests based on the buckling theory. He considered two cases – an elastic layer and a viscous layer, respectively, embedded in a viscous medium. The viscous matrix was corn syrup, the viscous layer was roofing tar and the elastic layer was made of cellulose acetate butyrate. The material properties were investigated in detail and Biot established the term “dominant wavelength”, i.e. the fastest growing disturbance in a viscous layer. He demonstrated that this wavelength is independent on the layer thickness and the viscosity contrast of both layer and matrix. Biot suggested that buckle folds would not form at viscosity ratios of less than 100.

Hudleston (1973b) modelled buckle folds of single viscous layers with various viscosity contrasts. The experiments were conducted under pure shear and plane-strain conditions. He used various solutions of ethyl cellulose in benzyl alcohol and investigated changes in arc length, layer thickness, wavelength/thickness ratio, amplification and fold shape. The latter was studied using a harmonic analysis (Hudleston, 1973a). The data obtained suggest the earliest visible fold shape to be close to sinusoidal and that the folds become broader in the hinges during progressive deformation. The changes in arc length suggested that layer parallel shortening decreased with increasing viscosity ratio of layer and matrix. If the folds had mean limb dips of 10 – 20°, a nearly constant arc length was established meaning that layer parallel shortening is only important at low amplitudes. Interestingly, Hudleston (1973b) produced folds at very low viscosity ratios (ca. 10) – a contradiction to Biot’s theory. However, Biot (1961) considered initial irregularities of a much small magnitude than those present in the experiments.

Watkinson (1975) conducted plane-strain experiments using clay multilayers with different viscosity and the layer-oriented perpendicular to the Y -axis of the finite strain ellipsoid. However, only the fold geometry in the YZ -plane was monitored. From these sections it was found that the thickness of the folded competent layers did not significantly change during deformation. Even at high finite strain, the folds are characterized by low amplitude to wavelength ratios.

Neurath and Smith (1982) investigated the growth rates of folds and boudins (the results of the latter will be described in 2.2). They used wax as rock analogue and investigated the material properties with uniaxial compression tests. The wax used for the experimental deformation is a power-law material characterized by both strain and strain-rate softening. The latter led to increased growth rates compared to the analytical solutions of e.g. Smith (1977). The viscosity ratios used in plane strain and pure shear models were 7.3 and 28. The experimental analysis was focusing on growth rates since these are more sensitive to rheological contrasts than the e.g. dominant wavelength.

Abbassi and Mancktelow (1992) conducted experiments with power-law material (paraffin wax) and investigated the influence of a pre-existing isolated perturbation in an otherwise planar layer. They characterized the material properties in detail. Experiments with three different bell-shaped perturbations (narrow, intermediate, and broad) and with two different viscosity ratios (8 and 30) were performed. They also compared results of layers with interfacial slip and welded interface. The development of fold shape was described by means of a Fourier series (see also Hudleston, 1973a). The presence of an initial perturbation controlled the development of the fold. Even up to large final amplitudes, the initial perturbation affected both the position of the component of maximum amplitude and the fold shape. However, neither the dominant wavelength nor the maximum growth rate was significantly influenced by the initial perturbation. Layer-parallel shortening decreased with increasing limb dips and ceased at around $30 - 40^\circ$. Strong bonding between layer and matrix

showed much slower amplitude of the perturbation and more homogeneous deformation than the experiments with welded interface.

Kobberger and Zulauf (1995) probably were the first who conducted pure constrictional strain experiments using plasticine. Folds and boudins formed in this power-law material. They observed the layer thickness to be approximately constant throughout the experiment and that the dominant wavelength of folds holds approximately the predictions of analytical solutions, e.g. Smith (1977).

Grujic and Mancktelow (1995) performed pure and simple shear experiments with paraffin wax under plane-strain conditions. They modelled folds with axes parallel to the extension direction. Especially the pure shear experiments with single competent layers and with two different viscosity ratios (8 and 600). At low viscosity ratios (30:1) and with initial perturbations of < 0.0125 of the layer thickness, the layer deformed homogeneously and no buckle folds developed. Folds only formed at high viscosity ratios (600:1) and propagated from the centre of the model towards its edges. The matrix flowed around the layer. In a second set of low viscosity ratio models, they introduced an initial perturbation. Only at large pre-experimental fold dips (ca. 45°) and large amplitude (1.5 of the layer thickness) the initially folded layers were boudinaged parallel to their fold axes.

Zulauf et al. (2003) conducted plane-strain experiments using a single competent layer of plasticine embedded in a weaker plasticine matrix. First results of these studies suggest that both folds and boudins grow simultaneously if particular layer thicknesses and viscosity contrasts are given. Especially the structures of plane-strain deformation, where folds and boudins should develop simultaneously if a stiff layer embedded in a weaker matrix is oriented perpendicular to the Y -axis of the finite strain ellipsoid, are of interest for the present study.

Numerical modelling using mathematical methods of integration of small portions has proved a useful alternative when high strains have to be reached. They were first used by Dieterich

(1969), Dieterich and Carter (1969) and have been employed extensively to analyze the influence of variables such as rheology, viscosity contrast and multilayer configuration in the folding process. This approach is only useful for modeling small folds. This method was applied for the linear-viscous case by several other workers, such as Hudleston and Stephansson (1974), Parrish (1973), Cobbold (1977), Anthony and Wickham (1978), Manz and Wickham (1978), Williams (1980) and Lan and Wang (1987).

Parrish (1973) extended the linear models to a non-linear one. However, the constitutive law used in his model was based on the linear case. After every strain increment the viscosity in each element was adjusted to the stress exponent. Thus the bulk behavior of the layer was of a power-law type. Gravity was included in the models by De Bremaecker and Becker (1978), but only for diapiric structures. Cruikshank and Johnson (1993) developed a numerical procedure to simulate high-amplitude folds, which they compared to large (up to 18 km) natural folds, even though they did not take into account the influence of gravity.

Johnson and Fletcher (1994) combined the analytical theory with numerical techniques and simulate viscous folding up to high amplitudes. However, investigations of finite amplitude folding were mainly performed using analogue and numerical experiments rather than nonlinear analytical theories. They performed experiments verified the assumed exponential growth of the fold amplitude for small strains. Thereby, exponential amplitude growth in settings with small competence contrast is valid for a wider strain range than in settings with high competence contrast. Also, the deformation component of homogeneous layer thickening increases when the competence contrast decreases. After the exponential growth the amplification slows down after a certain amount of strain (e.g., Cobbold, 1976; Hudleston, 1973; Zhang et al., 1996; Zuber and Parmentier, 1996). During progressive folding the alteration of geometric parameters (e.g., amplitude, arc length etc...) depends more or less strongly on the initial geometry and the material properties (e.g., Abbassi and Mancktelow, 1992; Hudleston, 1973; Ramberg, 1963). The different fold shapes of single-layer folds

developed in power-law material was used to estimate the power-law exponent from fold shapes (e.g., Hudleston and Lan, 1994; Lan and Hudleston, 1995b, and Lan and Hudleston, 1996). Furthermore, the initial perturbation of compressed layers was found to have a strong influence on the final fold development (e.g., Abbassi and Mancktelow, 1992; Cobbold, 1975; Mancktelow, 1999a, Mancktelow and Abbassi, 1992; Williams et al., 1978 and Zhang et al., 1996). The orientation and the distribution of stresses have been simulated during folding of single- and multilayer (e.g., Dieterich, 1970 and Stephansson, 1974). As expected, compressive stresses are observed within the lower parts of the fold hinge and extensional stresses within the upper part of the fold hinge. The development of thrusts was recorded within the fold limbs rather than within the fold hinges of compressed viscoelastoplastic layers (e.g. Gerbault et al., 1999).

2.3.3 Analogue models of boudinage

It seems that the first experimental studies on the formation of boudins were performed by Ramberg (1955). He used putty for simulating the incompetent rock and various kinds of modeling clay, plasticine and cheese for simulating the competent rock. No quantitative measurements of the material properties were conducted. However, Ramberg showed that the boudins shape and development depends on the strength and the plasticity of the layer. Additionally he presented an analytical treatise for fracture boudinage. Since then a large body of both natural and experimental work have been the subject of considerable study (e.g., Wilson, 1961; Ramsay, 1967; Etchecopar, 1974, 1977; Hobbs et al., 1976; Ghosh and Ramberg, 1976; Lloyd and Ferguson, 1981; Lloyd et al., 1982; Neurath and Smith, 1982; Woldekidan, 1982; Blumenfeld, 1983; Simpson and Schmid, 1983; Hanmer, 1984, 1986; Van der Molen, 1985; Ramsay and Huber, 1987; Goldstein, 1988; Lacassin, 1988; DePaor et al., 1991; Hanmer and Passchier, 1991; Mandal and Khan, 1991; Mandal et al, 1992; Swanson, 1992, 1999; Mandal et al, 2000; Goscombe et al., 2004). Previous attempts to

numerically model boudinage mostly dealt with the mechanisms of fracture and necking during layer-normal compression. Stress distribution and boudin displacement have been investigated with the use of the finite element method (*FEM*) and through theoretical considerations of elastic rock behaviour (Stephanson and Berner, 1971; Strömgarð, 1973; Selkmann, 1978; Treagus and Lan, 2000). Nevertheless, only very few experimental treatments using rock analogues to model boudins have been carried out.

Strömgarð (1973) studied the stress distribution in the regions adjacent to rectangular boudins with photo elastic material. However, due to the high tensile strength of the competent layer, the fracture had to be produced by cutting it. He also presented an analytical treatise on stress distribution in single and multilayer systems assuming linear-viscous or elastic material properties. One of the numerous general conclusions of this study is that the length of boudins formed by tension fracture is 2 – 4 times the layer thickness. If the deformation involves necking before rupture, the boudins might to be longer.

Neurath and Smith (1982) conducted numerous experiments using wax models and found that the boudins grew almost three times faster than predicted by the analytical solutions.

Woldekidan (1982) performed various experiments using wax or plasticine multilayer shortened perpendicular to the layering. Rectangular experimental boudins were compared with natural examples. Additionally he found out that low competence contrasts and/or closely spaced competent layers lead to a bulk mechanical anisotropy and thus internal pinch and swell and/or kink bands developed.

Mandal and Khan (1991) conducted experiments with obliquely cut wax layers submerged in pitch in order to study the offset and rhomboidal boudins during layer normal compression. They found out that rhomboidal boudins might either separate or only rotate and offset depending on the geometry.

Mandal et al. (1992) performed experiments with tubes of polyethylene, which were uniaxially stretched. The development and nature of wide-necked pinch and swell structures

was investigated. They concluded that neck zone spreading might be an important process in the development of pinch and swell structures. Furthermore, they observed that a swell dies out if two adjacent necks coalesce with each other.

Mandal et al. (2000) investigated the formation of tensile, shear fracture boudinage in multilayered plasticine, and found that the type of boudinage (i.e. shear or tensile fracture boudinage) and the aspect ratio (width/thickness) of boudins is dependent on the thickness ratio (T_R) of the brittle and ductile layers. The aspect ratio is exponentially increasing with decreasing T_R . Extensional shear fracture boudinage forms when T_R is in the range of 0.1 and 3.4, tensile fracture and shear fracture boudins at smaller and larger ratios, respectively.

3 EXPERIMENTAL APPROACHES

3.1 Scaling procedure

Our knowledge on rock deformation arises from field studies and laboratory experiments, the latter being applied to natural rocks or to analogue material. The problem of the reduction of scale and rate, necessary for experimental approach, is very delicate when a tectonic structure is modelled. For experimental reasons of choice of materials and due to the imperfect knowledge of the rheological properties of rocks under natural conditions it is impossible to replicate the nature in all aspects during modelling. It is thus necessary to choose well constrained material and perform the experiments under controlled conditions to keep uncertainties at minimum. The theory of these rules was first introduced by Hubbert (1937) and was later discussed by Hubbert (1951), Horsfield (1977), Shemenda (1983), Weijermars and Schmeling (1986), Richard (1991), Davy and Cobbold (1991) and Cobbold and Jackson (1992).

Weijermars and Schmeling (1986, Fig. 3) compiled a flow map (log strain rate vs. log stress) of various rocks and commonly used analogue materials (Fig. 3.1).

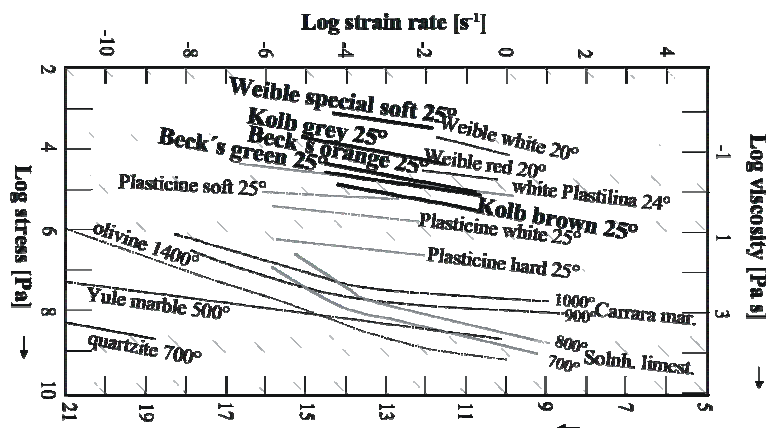


Fig. 3.1: Log stress vs. log strain rate diagram showing flow curves of investigated rock samples (at $e = 10\%$) and analogue material, tested in previous studies: Weible red and Weible white plasticine at $e = 5\%$ (Kobberger and Zulauf, 1995); Plasticine Special Soft, Plasticine Standard Hard and plasticine Standard White at $e = 10\%$ (McClay, 1976); White Plastilina (Weijermars, 1986). Flow curves for rocks: Yule marble (Heard and Raleigh, 1972), Solnhofen limestone (Schmid et al., 1977); Carrara marble (Schmid et al., 1980); quartzite (Heard and Carter, 1968); olivine (Ashby and Verall, 1977); all temperatures are in $^{\circ}\text{C}$ (diagram after Zulauf and Zulauf, 2004).

Rocks can flow by diffusion and/or dislocation creep, where the fastest mechanism is dominating the flow. Natural rocks appear to have stress exponents between 1 and 10. Griggs et al. (1960) presented stress-strain curves at 5 kb confining pressure and strains of about 15% for different rocks. Dunite, pyroxenite and Yule marble showed either steady-state deformation or strain hardening. Basalt, granite and dolomite showed strain softening over a wide range of experiments. Additionally quartzite exhibited strain softening (Heard and Carter, 1968). In order to determine the rheology of Carrara up to very high shear strains ($\gamma = 28$), experimental investigations of Barnhoorn et al. (2000) have shown strain hardening until a peak stress was reached ($\gamma = 1 - 2$). Then the material entered the strain softening range until a steady-state flow was reached. However, the stress exponent ($n = 7 - 9$) was constant (Barnhoorn, pers. com., 2000) when the material deformed by power law creep (> 600 °C). Non-Newtonian flow is recently the best rheological model for most rocks, if dislocation creeps is the dominant deformation mechanism (Fig. 3.1). However, Paterson (1987) reviewed problems that arise if laboratory data are extrapolated to the scale of geological processes. Unknown variables are, for example, the confining pressure, the chemical environment, the presence of a fluid phase, the grain size and the preferred crystallographic orientation.

In the present study, plasticine has been used as analogue material. The macroscopic behaviour of most types of plasticine is quite similar as in rocks undergoing strain-rate softening and strain hardening regardless of the different microscopic aspects of deformation (Zulauf and Zulauf, 2004; and references therein). Therefore, if one is aware that the stress exponent and viscosity increase with increasing strain, the original plasticine types used with stress exponent ranging from 5.8 to 8.0 (see 3.2 and 4.1) are adequate for modelling geologic structures. The same holds for plasticine/oil mixtures. Thus, plasticine and plasticine/oil mixtures can be used to model the viscous flow of different rock types in the lower crust. If climb-accommodated dislocation creep and associated steady-state flow is assumed for the

natural rocks, the three plasticine/oil mixtures should be used, which flow under steady-state conditions.

Most of the experiments show that strain hardening occurs particularly at low temperatures and/or higher strain rates. Possible candidates for strain hardening are rocks, which are subjected to decreasing temperatures during exhumation from deep structural levels where climb-accommodated steady-state creep was possible. As the temperature, decreases during uplift, recovery by dislocation climb might be inhibited leading to strain hardening (Zulauf and Zulauf, 2004). Strain hardening is further important for the geometry of folds (Tentler, 2001). The activation energy of plasticine is similar to that of Carrara Marble ($Q = 418 \text{ kJ mol}^{-1}$; Schmid et al., 1980) and wet dunite ($Q = 420 \text{ kJ mol}^{-1}$; Chopra and Paterson, 1981). Most of the other rocks (e.g. quartzite, granite, quartzdiorite, diabase, and anorthosite) show activation energies below 420 kJ mol^{-1} (Kirby, 1983; Ranalli and Murphy, 1987). Thus, the rock most appropriate for being modelled using plasticine is Carrara Marble because both the stress exponent and the activation energy are similar to those of plasticine (Fig. 3.1).

3.2 Plasticine as analogue material

Plasticine is a modelling material that has been widely used to simulate deformations both in metallurgical (Green, 1951) and in geological research (e.g. Watkinson, 1975; Sokoutis, 1987). As we are using rheologically stratified plasticine as a rock analogue to investigate the growth of folds and boudins in three dimensions, detailed studies have been carried out concerning the rheology of different types of plasticine. For the selected experimental conditions, to demonstrate the impact of plane-strain coaxial deformation on the deformation structures of rheologically stratified analogue material, we investigated a stiff layer, with viscosity η_2 and stress exponent n_2 , embedded in a weak matrix, with viscosity η_1 and stress exponent n_1 . The layer consisted of *Beck's black* and *Kolb grey* plasticine, commercially available plasticine produced by German manufacturers made by *Beck's Plastilin*,

Gomaringen and *Kolb*, Hengersberg, Germany, respectively. The matrix consisted of *Beck's green* plasticine, also produced by *Beck's Plastilin*, Gomaringen. To reduce the viscosity of the original *Beck's green* plasticine (termed Bg0), which formed the weak matrix, the material was partly modified by adding 50, 100 and 150 ml medical white oil (Liquid paraffin, made by DEA, Hamburg) to 1 kg warm (55°C) *Beck's green* plasticine. The uncertainty in temperature is $\pm 1^\circ\text{C}$. Both were mixed in the laboratory using a kitchen aid machine to obtain the new plasticine types Bg50, Bg100 and Bg150. After mixing with the machine, the Plasticine/oil mixtures were additionally homogenised by hand and then wrapped in an ethylene bag during a few days. This plasticine constitutes the basic material for the preparation of the samples. Then it has to be homogenised by hand and 1 kg was moulded into a cube-like shape. The plasticine was then cut to cubes with a side length of 7 cm for Bg50, Bg100, and 8 cm for Bg150 with a wire-saw (Zulauf, 2004; Fig. II.2) at room temperature for the rheological measurements. It is important to note that different coloured plasticine, even if produced by the same company, have different physical properties (e.g. Sofuoglu and Rasty, 2000). Therefore, our data are only valid for *Beck's green*, *Beck's black*, *Kolb brown*, and *Kolb grey* plasticine.

The exact composition of plasticine is largely unknown because of patent restrictions. According to manufacturer's declarations, the organic matrix of plasticine consists of white oil, wax, Vaseline and lubrication solvent. The composition and shape of the filling components of plasticine is of interest, as the individual components may rotate in the weak deforming organic matrix, resulting in shape-preferred orientation and related strain hardening. The calcite and barite fillers of *Beck's green* and *Kolb grey* are plate shaped. Some of the plasticine types include small amounts of dyes such as titanium dioxide, magnetite or haematite (Zulauf and Zulauf, 2004). The volume percentages of calcite in *Beck's green* and *Beck's black* plasticine are ca. 46% (Schöpfer and Zulauf 2002). The black colour results from additional magnetite (Zulauf and Zulauf 2004).

The rheological data indicate that all types of plasticine are non-linear viscous materials characterized by strain-rate softening. The higher the strain rate, the lower is the viscosity (McClay, 1976, Zulauf and Zulauf, 2004). Plasticine types with mineral fillers show strain hardening, whereas plasticine with organic fillers shows steady-state creep (Zulauf and Zulauf, 2004). A rise in temperature results in linear decreases of n , η , and a reduction in the degree of strain hardening. Steady-state creep and major changes in n and η have further been observed at decreasing filler-matrix ratios, the latter being obtained by adding oil to the original plasticine (Zulauf and Zulauf, 2004).

3.2.1 Rheological measurements

3.2.1.1 Sample preparation

Commercially available plasticine is porous with a considerable amount of isolated air pockets. In order to establish a reasonable degree of homogeneity, these air pockets should be squeezed out of the material. First the plasticine was put in the oven at 55°C for about one hour in order to make it softer and easier to handle. The procedure to obtain cubes was the same as described above. The initial samples were cubes (edge length = 5 cm for original *Beck's green* (Bg0) and *Kolb grey* plasticine (Kg0)).

To mould the plasticine into cubes, the viscosity of the hard types was decreased by heating up to ca. 50°C for a maximum of 1 hour (Zulauf and Zulauf, 2004). The viscosity of the heated samples is significantly controlled by the degree of kneading during the cooling period. Samples heated to $T = 55^\circ\text{C}$ and cooled to room temperature without deformation are much harder than those samples that are slightly moulded by hand during cooling (Zulauf and Zulauf, 2004). Further caution is needed to avoid air bubbles, which might be introduced into the plasticine during the moulding process. These bubbles are possible sites where shear fractures may occur (Zulauf and Zulauf, 2004).

From *Beck's green*, *Beck's black* and *Kolb brown* plasticine, the rheological parameters were available from the literature (Table 4.1).

3.2.1.2 Uniaxial compression tests

The rheological parameters of *Kolb grey* and modified *Beck's green* plasticine have been determined applying uniaxial compression tests on plasticine cubes for constant strain rates ranging between 10^{-1} and 10^{-5} s^{-1} and for finite strain of 10%. The testing apparatus was a *Zwick/Z-050* traction apparatus at the Lehrstuhl für Polymerwerkstoffe, Werkstoffwissenschaften, Universität Erlangen. For our purpose, the traction apparatus was rearranged for uniaxial compression. The upper steel plate was fixed and the lower plate was moving constantly. The plate distance (dl) and the force (F) were recorded at steps of 0.02 to 1 s and the machine was linked to a computer to provide a force vs. strain plot during each run. The computer aided machine worked at constant velocity ranging from 400 to less than 0.04 mm s^{-1} . The data for the stress vs. strain diagrams were calculated using *Excel software*. The plates were within a heat chamber and the temperature was hold at 25°C . The uncertainty in temperature is $\pm 1^\circ\text{C}$. However, during the summer months, the room temperature was nearby 25°C and the chamber was overheated. The problem was solved by using a cooling box filled with water, which was heated with an aquarium thermostat. The cubes were put into water for at least one hour before the rheological test. The water dissolved the colour pigments and the samples had to be wrapped in polyethylene. Otherwise, the rheology was changed tremendously and lower viscosities were obtained.

To reduce friction, the piston of the machine, the plates and the cubes surfaces were lubricated with Vaseline. Plasticine is an approximately incompressible fluid. Thus homogeneous constant-volume deformation can be assumed. Rheological calibration was performed with a series of strain rates applied to the cubes and measuring the change of the differential stress as the axial strain progresses up to 10%. Eight runs have been carried out for each material at

finite strain rates ranging from 5.4×10^{-3} to $5.5 \times 10^{-5} \text{ s}^{-1}$ for the original *Kolb grey* plasticine (Kg0). Six runs have been carried out for each material at finite strain rates ranging from 1.2×10^{-2} to $1.4 \times 10^{-4} \text{ s}^{-1}$ for the original *Beck's green* plasticine (Bg0), 9.0×10^{-3} to $9.5 \times 10^{-5} \text{ s}^{-1}$ for Bg50, 8.0×10^{-3} to $8.5 \times 10^{-5} \text{ s}^{-1}$ for Bg100 and 8.9×10^{-3} to $9.5 \times 10^{-5} \text{ s}^{-1}$ for Bg150. The results were homogeneously deformed cubes with nearly quadratic base and straight edges indicating pure oblate deformation ($X = Y > Z$).

As the initial samples were cubes, the stress (σ) was calculated using the following equations:

$$\sigma = \frac{F(L - dL)}{L^3} \quad [3-1]$$

where L is the edge length of the cube (Fig. 3.2).

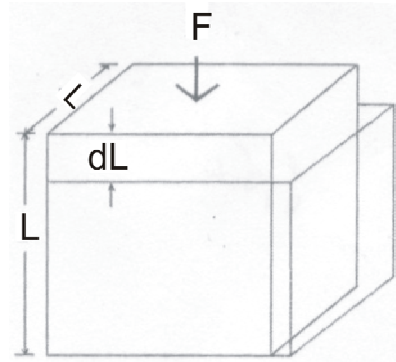


Fig. 3.2: Cartoon showing undeformed and deformed sample: F = force; L = length of undeformed sample; dL = shortening increment (after Zulauf and Zulauf, 2004).

According to Neurath and Smith (1982), the actual deviatoric stress in this experimental set-up is 2/3 of the measured stress. The incremental strain rate was calculated by dividing the plate speed by the instantaneous sample height:

$$e_n[\%] = \frac{l - L}{l} \times 100\% \quad [3-2]$$

The finite longitudinal strain rate is calculated by equation:

$$\dot{E} = \frac{e(t)}{dt} \quad [3-3]$$

where e is the finite strain and t is the time.

As the ram speed is constant throughout a test, the strain rate is not constant. However, at $e \leq 50\%$ the difference between finite and incremental strain rate is small and can be neglected.

3.2.1.3 Stress exponents

Previous studies have shown that the flow behaviour of plasticine and related materials is non-Newtonian, which can be approximately described by the so-called Dorn equation (e.g. Ranalli, 1995):

$$\dot{\epsilon} = A\sigma^n \exp(-E^*/RT) \quad [3-4]$$

where $\dot{\epsilon}$ is the steady-state strain rate, A is a material constant, σ is the differential stress, n is the stress exponent, E^* is the activation energy, R is the universal gas constant and T is the absolute temperature.

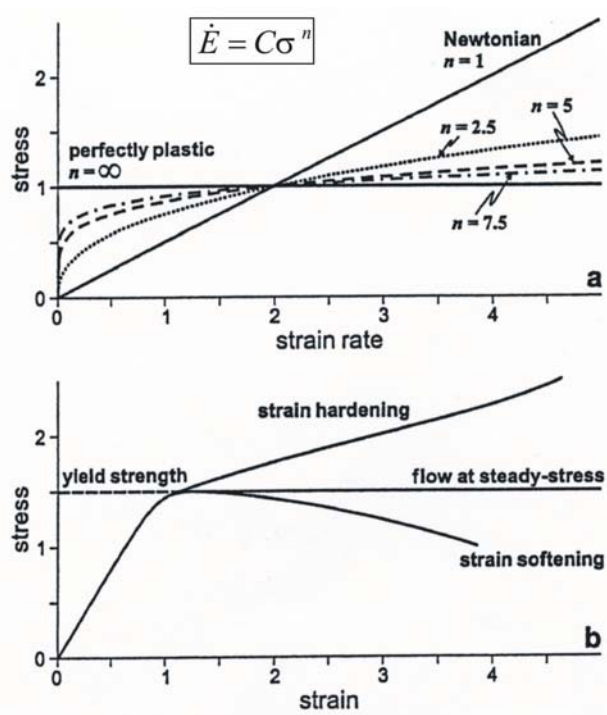


Fig. 3.3: Schematic graphs (with arbitrary scaling) showing terminology of flow behaviour. (a) Stress vs. strain rate diagram where Eq. (3-5) is plotted for various values of the stress exponent, n . Materials with $n = 1$ are Newtonian, with $n > 1$ are strain-rate softening and with $n = \infty$ are perfectly plastic (see also Twiss and Moores, 1992; Weijermars, 1997). (b) Stress vs. strain curves for ductile failure. In theory, the stress is constant after yielding (flow at steady stress), but it can either increase (strain hardening) or decrease (strain softening) (e.g. Ranalli, 1995) (after Schöpfer and Zulauf, 2002).

The equation $C = A \exp(-E^*/RT)$ represents the reaction rate as a function of absolute temperature and is known as Arrhenius equation. Therefore, at a constant temperature and strain, the constitutive equation for a non-Newtonian material (Equation [3-4]) can be written in a simplified form as follows (e.g. Weijermars and Schmeling, 1986; Ranalli, 1995; Fig. 3.3a):

$$\dot{E} = C\sigma^n \quad [3-5]$$

where \dot{E} is the longitudinal strain rate, C is a temperature- and strain-dependent constant (material constant), σ is the differential stress, and n is the stress exponent (McClay, 1976).

Equation [3-5] can be rewritten as follows:

$$\log_{10} \dot{E} = \log_{10} C + n \log_{10} \sigma \quad [3-6]$$

To obtain the stress exponent n , the deviatoric stress at a given strain (e.g. 10%) is plotted in a log stress vs. log strain rate diagram. The slope of a linear best-fit least-squares regression of a log strain-rate vs. log stress diagram yields the stress exponent. The intercept at the ordinate yields the material constant (C). The major uncertainty concerns the stress, whereas the strain rate is largely independent, apart from the uncertainties of the machine, the latter being negligible. Therefore we use a log stress vs. log strain-rate plot, where the slope of the regression line yields $1/n$ and C' is the intercept along the vertical stress axis (Fig. 3.4).

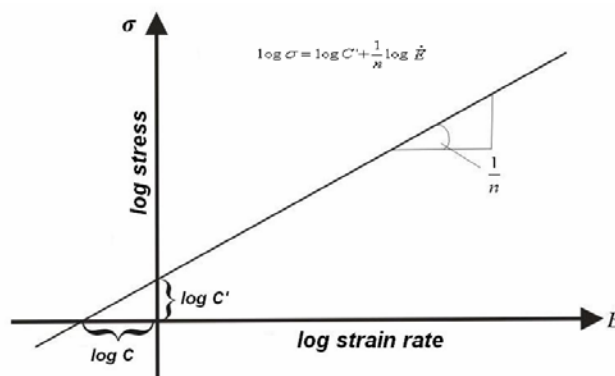


Fig. 3.4: Schematic diagram of log differential stress (σ) vs. log strain rate (\dot{E}). Slope of regression line gives $1/n$; for further explanation see text (after Zulauf and Zulauf, 2004).

Starting from Equation [3-6], the material constant can be calculated by substituting (σ/\dot{E}) couples determined experimentally (Weijermars and Schmeling, 1986). We calculated the material constant using the linear best-fit least-squares regression (Fig. 3.4) and the following equation (Zulauf and Zulauf, 2004):

$$C = 10^{-\log C^n} \quad [3-7]$$

3.2.1.4 Apparent viscosity

Plasticine is a non-Newtonian material, i.e. the stress/strain rate relationships are non-linear. The apparent dynamic viscosity η can be calculated by the following equation:

$$\eta = \frac{\sigma}{2\dot{E}} \quad [3-8]$$

Equations [3-6] and [3-8] yields Equation [3-9], which can be used to calculate the apparent dynamic viscosity using all data couples (Zulauf and Zulauf, 2004):

$$\eta = \frac{1}{2C^{\frac{1}{n}}} \dot{E}^{\frac{1}{n}-1} \quad [3-9]$$

3.3 Analogue modelling of geological structures

3.3.1 Deformation apparatus

The experimental deformation apparatus used to study the influence of the deformation regime on the geometry of a deforming stiff plasticine layer embedded in a weak plasticine matrix is shown in Figs. 3.5 and 3.6 (Zulauf et al., 2003). The numbers in Fig. 3.5 refer to the bracketed numbers in the following text. The apparatus consists of a basal PVC plate [1], on which six aluminum plates [2]–[7] have been orthogonally assembled. As the initial specimen geometry leads to point loads, which result in strong bending of plates [2]–[5], these plates have been reinforced with U-shaped beams made of steel (only shown in Fig. 3.6). Plates [2]

and [7] are fixed to the basal plate. Plates [3]–[6] are movable. In the top view of Fig. 3.5 the movement direction is indicated by black arrows. Axes a and b of the orthogonal Cartesian co-ordinate system describe the horizontal directions.

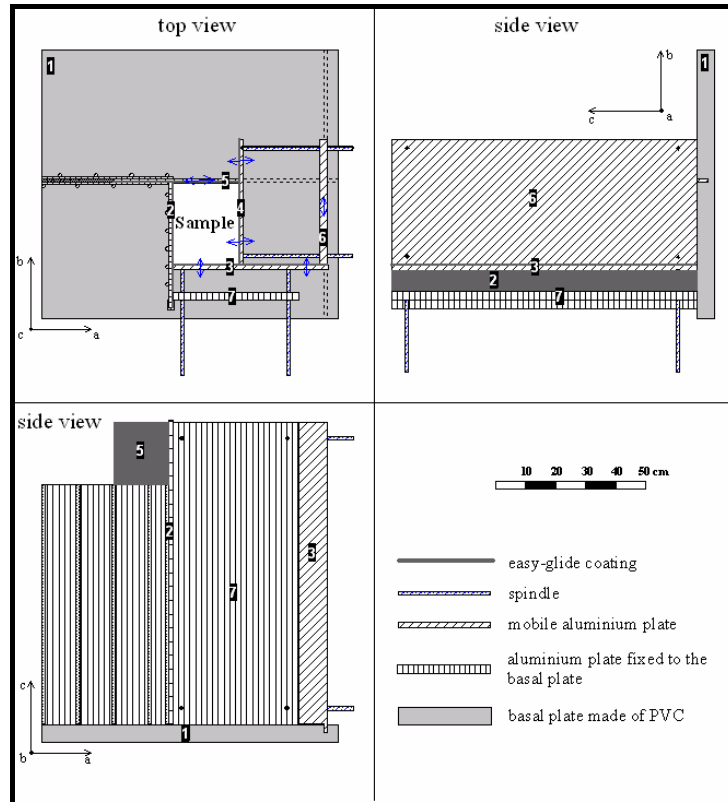


Fig. 3.5: Technical drawing of the new deformation apparatus, with the motors and tooth belts not shown (after Zulauf et al., 2003).

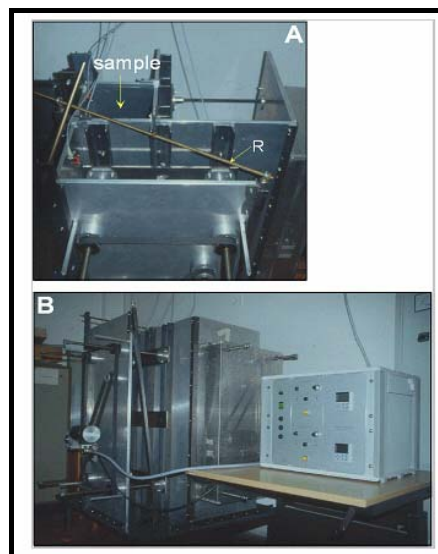


Fig. 3.6: Photographs of the deformation apparatus and electronic control unit. (A) View from above. (B) Side view. R = reinforcement spindle (after Zulauf et al., 2003).

The c axis denotes the vertical direction. Plate [6] is fixed to plate [3] and slides within a groove of the basal plate along the b direction. Plate [5] also slides within a groove of plate [1] along the a direction. Except for pure flattening strain (see below), the analogue material is bounded by plates [2]–[5]. Maximum initial model dimensions are usually $30 \times 30 \times 30$ cm. To deform the specimen, the mobile plates are shifted horizontally along the basal plate in the a and b direction, respectively. Plates [2]–[5] are faced with Teflon sheets to reduce friction. The movement of plates [3] and [4] is performed in each case by four spindles, driven by two motors via gears and a toothed belt (shown in Fig. 3.6 only). One of the motors is fixed to plate [7]; the other is fixed to plate [6]. The motor speed is variable in the range 1–3000 rpm, and the number of revolutions is shown on a digital display. The corresponding longitudinal finite strain rates $\dot{\epsilon}$ range from 4×10^{-6} to $1 \times 10^{-2} \text{ s}^{-1}$.

If plate [3] moves along the b direction, plates [6] and [4] also move in this direction, because plate [6] is fixed to plate [3] and plate [4] is linked to plate [6] by the four spindles. If these spindles are pushing plate [4] along the a direction, plate [5] is also shifted along the a direction. With this geometry an absolute maximum of 78% horizontal shortening is possible in the a and b directions. In cases of *pure constrictional strain* (Flinn parameter $k = \infty$) a control gear maintains the same speed for both motors, meaning that plates [3] and [4] are moving with the same velocity along the horizontal $Y = Z$ axis of the finite strain ellipsoid, and the X -axis is vertical. There are two possibilities to produce *plane strain* ($k = 1$). In one case, plate [3] and associated plates [4] and [6] move parallel to the b direction (that is equivalent to the Z -axis of the finite strain ellipsoid), whereas plate [5] is immobile. In the other case, plates [3] and [6] are immobile and plates [4] and [5] move along the a direction that is parallel to the Z -axis of the finite strain ellipsoid. Similar to the case of constrictional strain, the X -axis of the finite strain ellipsoid is vertical in both cases of plane-strain configuration.

3.3.2 The experimental procedure

To demonstrate the impact of plane strain on the deformation structure of rheologically stratified analogue material, we investigated a stiff layer, with viscosity η_2 and stress exponent n_2 , embedded in a weak matrix, with viscosity η_1 and stress exponent n_1 . The following three deformation regimes were considered: (1) plane strain-coaxial deformation with the stiff layer perpendicular to the long axis, X , of the finite strain ellipsoid (Fig. 1.1a), (2) plane strain-coaxial deformation with the stiff layer perpendicular to the short axis, Z , of the finite strain ellipsoid (Fig. 1.1b), and (3) plane strain-coaxial deformation with the stiff layer perpendicular to the intermediate Y -axis of the finite strain ellipsoid (Fig. 1.1c). Additional runs have been carried out under pure constrictional conditions.

Layers are obtained by pushing a plasticine block (which was moulded in the same way as described above) gently through a horizontally spanned wire. With this technique it is possible to obtain layers with thicknesses of the stiff layer ranging from 1 ± 0.2 to 10 ± 0.2 mm at 1 mm increments. Acetate sheets, which were lubricated on either side with Vaseline, were put between plates and plasticine. The plasticine was then easily removed from the plates. Plasticine that has been in contact with Vaseline (injections) was removed. Layers were cut perpendicular to the previous shortening direction with a horizontally spanned wire as described above. Distinct instabilities were not inserted into the layer before assembling it with the matrix blocks.

The “matrix-block” was cut in the middle and the layer was put carefully in-between the two halves. The initial samples (matrix plus layer) were cubes (edge length = 12 cm). Good adherence was obtained if the block was put in the oven (55 °C) for about an hour. The sample is then stored in the analogue modelling laboratory over night.

Before putting the specimen into the machine, the surfaces of the sample were lubricated with Vaseline and put into a bag made of ultra thin PVC to reduce friction. Subsequently the bag was also lubricated with Vaseline like the plates of the apparatus. The sample rested on a

tripod, which was inserted through a hole in the basal plate. Then the Y -plate (the plate perpendicular to the Y -axis of the finite strain ellipsoid) was moved. Gentle compression was sufficient and the sample stayed at its height without support. The tripod was then removed from underneath and the analogue material is then bounded by plates [1]-[4] (see Fig. 3.5). All experimental runs were carried out until a finite longitudinal strain of 30% was achieved. Further experiments have been carried out with a viscosity contrast $m < 10$ and were deformed in one run until 40% finite strain were achieved. After the experiment the plates were driven back. The sample was easily removed in its ethylene bag. To investigate the geometry of the deformed stiff layer, the specimen was cut in half along the X -axis. One of the halves served for analysing the geometry of the boudins (XY -sections), the other half was used to examine the folds (YZ -sections) (Fig. 3.7). The spacing of the single cuts was set at 1–3 cm. There was no problem in reassembling the YZ -sections in order to investigate the XZ -sections. The obtained slices were photographed and scanned.

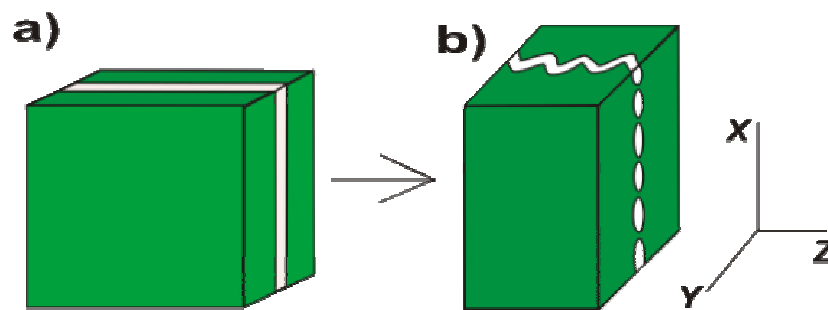


Fig. 3.7: Schematic drawing of undeformed (a) and deformed sample (b).

3.4 Computer Tomography (CT)

3.4.1 Introduction

Computer tomography (Greek *tome* = cutting, *graphia* from *graphein* = to write) is an imaging process permitting insights into the interior of a spatial body without destroying it. By using tomography, the contents of the drums can be analysed *nondestructively* - without

having to open the drums. The decisive advantage is that the contents of the drums are shown to the user by the tomograms thus generated, so that even complex structures can be observed at a glance. The facility essentially consists of a radiation source, a detector system and a mechanism for handling the drum to be examined. Use of laboratory or industrial computed tomography has several advantages compared to laboratory or industrial X-ray sources. These include: (i) a high photon flux permits measurements at high spatial resolution; (ii) the X-ray source is tuneable, thus allowing measurements at different energies; (iii) the X-ray radiation is monochromatic, which eliminates beam-hardening effects; and (iv) the beam is flat (line scanning), which simplifies the reconstruction. Methods and applications of synchrotron and conventional computerized X-ray tomography are reviewed in Wellington and Vinegar (1987), Bonse and Busch (1999), Rivers et al. (1999), and Ketcham and Carlson (2001).

Computer tomography (CT) was originally designed for medical applications (Hounsfield, 1973; Kantzas et al., 1992) as a non-destructive technique for the investigation of internal structures of human bodies. It is now applied to a variety of non-medical fields (Duliu, 1999). Geologists have adapted CT (Wellington and Vinegar, 1987; Kenter, 1989; Long and Ross, 1991; Orsi et al., 1994; Boespflug et al., 1995; Crémer et al., 2002) to characterize sedimentary facies in marine sediments.

In preparation for the analysis, the core is positioned on a bed that slides through a gantry (Michaud et al., 2003; Fig. 2). The gantry is made up of an X-ray source that is opposite to 600 receptors (Michaud et al., 2003). The receptor – source system rotates around the sample in a short period of time (2 s for one image). This helical rotation allows the measurement of the X-ray attenuation through the core at many different angles (Wellington and Vinegar, 1987). X-ray beams are attenuated through the matter following the Beer – Lambert law:

$$I = I_0 e^{-\mu x} \quad [3-10]$$

where I_o , I , and x are the initial intensity of the X-ray incident beam, the measured attenuated intensity on the detectors, and the sample thickness, respectively. The parameter μ is the linear attenuation coefficient depending on both the atomic number and the density of the investigated object (Boespflug et al., 1994).

In the present study, we used computer tomography (CT) in cases where the newly formed structures were weakly developed and thus difficult to examine using the procedure described above. The CT-studies were performed using a multislice spiral CT-scanner “Somatom Plus 4, volume Zoom, Siemens Erlangen” at Neurocenter, Department of Neurosurgery, Universität Erlangen-Nürnberg University, Germany (Fig. 3.8).

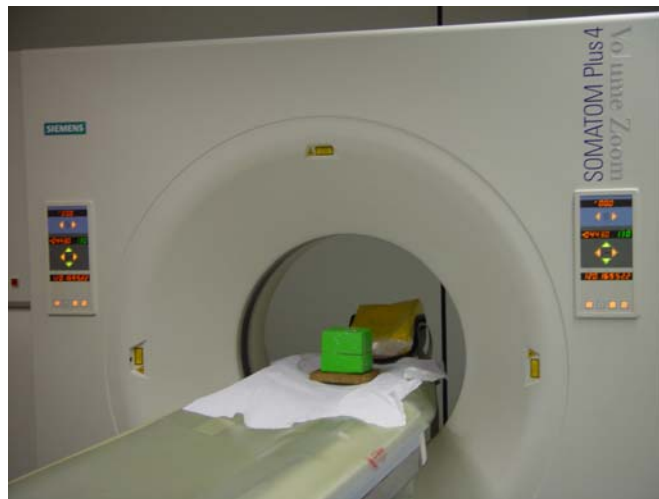


Fig. 3.8: Computer Tomography “Siemens Somatom Plus 4”, showing how the analogue material were taken up at the Division of Neuroradiology of the University of Erlangen-Nürnberg; the layer and the matrix consisted of Beck’s black and Beck’s green plasticine, respectively.

The modulation of the scans was carried out under the following conditions: collimation 4×1 mm; slice 1.25 mm; increment 1 mm, and table feed 8.7 mm. According to the details reported by the manufacturer and X-ray diffraction analyses, the initial contrast between the layer and the matrix consisted of Beck’s black and Beck’s green plasticine. Secondly, the contrast between layer and matrix consisting of Kolb grey and Beck’s green plasticine, respectively, is sufficient to distinguish structures in CT-images (Zulauf et al., 2003, Zulauf and Zulauf, 2004). A major disadvantage of the CT as seen in this study is its inaccurate

spatial resolution. Sometimes boundary surfaces between materials with different densities cannot be defined clearly. Besides, the CT used here can only dissolve up to 5 mm large ranges smaller details up to 1 mm become interpolated (Zulauf, 2004; Fig. III. 5).

3.4.2 Visualization of the CT-data

Visualization of CT data typically profits from the ability to view arbitrarily oriented sections through the three-dimensional volume represented by the data, and from the capability to extract features of interest selectively and display perspective views of them using methods of *isocontouring* or *volume rendering* (Ketcham and Carlson, 2001).

Although direct *volume rendering* is a powerful tool for visualizing complex structures within volume data, the size and complexity of the parameter space controlling the rendering process makes generating an informative rendering challenging (Wellington and Vinegar, 1987; Bonse and Busch, 1999; Rivers et al., 1999; Ketcham and Carlson, 2001). In particular, the specification of the transfer function -- the mapping from data values to renderable optical properties -- is frequently a time-consuming and unintuitive task. Ideally, the data being visualized should itself suggest an appropriate transfer function that brings out the features of interest without obscuring them with elements of little importance (Rezk-Salama, 2002; and references therein). It is therefore hardly possible to study the geometry of the deformed stiff layer in 3D using conventional cuttings along *XZ* or *YZ* planes. The *volume rendering* technique has been used to carry out the CT-images necessary to quantify the geometry of deformed layers in 3D and 4D.

For the visualization of the CT-data the program OpenQVis (Rezk-Salama, 2002), developed by the Department for Computer Science 9 (Computer Graphics) of the University of Erlangen-Nürnberg), was used. This program converts the 2D of data records (pixels) in volume data (Voxel). The rendition is difficult because of the complexity of the recorded data. For instance, volume data have to be interactive with respect to the rotation of the 3D-Data.

This also applies to the change of the opinion parameters, the adjustment of the shade and the arrangement function. The accuracy with respect to resolution of the regional structures in the recorded data is fixed in the physical model for discrete volume data. Moreover, artefacts of the special rendition algorithm affect quality (Rezk-Salama, 2002).

The volume data cover grey tones for matrix and stiff layer. Due to different physical characteristics of stiff layer and matrix, the respective Voxelparameter has different threshold values. By changing the threshold value, it is possible to blend out the matrix and hence show the stiff layer only. Threshold value dependent, the stiff layer is differentially reproduced, leading at times to ambiguous interpretations.

As for now, a set up approximating the ideal conditions, especially with a direction perpendicular to the stiff layer is not known. If the stiff layer is adjusted to the power value material, too little Voxel is represented and the stiff layer is "loechrig", i.e. the number of boudins rises strongly. A calibration of the volume data is only partially possible. There is the possibility of sending the stiff layer a certain volume and of determining dependent on it the threshold value border. Thus, the layer strength in the case of the incremental investigations decreases apparently, although actually an increase occurs. A possibility for this effect could be the dependence of the CT data on power and the size of the parts. A coherent stiff layer or a strongly folded range reflected clearly more strongly than a strongly boudined stiff layer, i.e. the X-ray penetrate the necks more strongly than the boudins and blooming thereby their edges. Threshold value attitudes concern cases primarily, in which the line of sight runs perpendicularly to the stiff layer. The changes parallel to the stiff layer are negligible.

3.4.3 Evaluation of the CT-data

Besides the visual assessment of the deformed samples with the OpenQVis Program (Rezk-Salama, 2002) there was also a quantitative geometrical analyses with the help the program geoCT (Kaisersberger, 2002).

OpenQVis makes a 3D-visualization of CT-data possible (Zulauf, 2004; Fig. III.5). The transformed data are illustrated in the grey tones given by the CT. This 3D picture can rotate, increase or translate. Moreover, thanks to OpenQVis, even sections of a chosen plane can be moved and rotated (Zulauf, 2004; Fig. III.5). An assessment of samples parallel to arbitrary cuts in all possible directions is possible. Furthermore, a measuring function is an integral part of the program, which permits simple end-to-end measurements. This end-to-end measurement takes place in the area. Special application of the program is also found in Medicine (Rezk Salama, 2002; <http://openqvis.sourceforge.net/gallery.html>).

The program geoCT makes the statistical assessment of the CT-data possible (Kaisersberger, 2002). A conversion of the data is also necessary. Along the 3 principal axes of the finite strain ellipsoid cross section transverse sections are possible in distances given by the CT (Zulauf, 2004; Fig. III.5). The program count objects of the stiff layer and measure automatically those perpendiculars to the plane defining main axis. The found objects are shown in alternating colours (Zulauf, 2004; Fig. III.5). This example shows that automatic object identification is only permissible, if the individual boudins are already drifting apart in the course of the progressive deformation.

The determination of the actual layer thickness is similarly problematic as with the program OpenQVis. An additional programmed function (Institute for Computer Science of the University of Erlangen-Nürnberg) makes a representation based on the volume possible. The evaluations took place for all samples with a threshold value based on a constant volume (85.000 mm^3). This numeric value was empirically determined. The attitude was decisive, with which the number of boudins corresponded to the value of the conventional cut evaluation.

Besides, well-trained folds can be measured efficiently on the basis an automatic drawing and centrelines identification. With initially trained folds or with ingates disturbed by Boudinage

the structures were measured manually. Furthermore, boundary regions were not considered and amplitudes were principally measured manually.

4 EXPERIMENTAL RESULTS

4.1 Rheology of plasticine used for experiments

The rheological data of the different types of plasticine used in the present study are summarized in Table 4.1. Apart from strain-hardening effects, the viscosity of *Beck's black*, *Kolb brown* and *Kolb grey* plasticine, which formed the stiff layer, was held constant throughout the experiments.

<i>Material</i>	<i>n</i>	η [Pa s]	$\dot{\epsilon}$ [s^{-1}]	<i>e</i> [%]	<i>T</i> [°C]	<i>Study</i>
<i>Beck's green</i>	8.6	1.1×10^7	4×10^{-3}	10	25	<i>Zulauf and Zulauf (2004)</i>
<i>Beck's green (Bg0)</i>	7.9	7.2×10^6	2×10^{-3}	10	25	<i>This study</i>
<i>Bg50</i>	13.5	6.8×10^6	2×10^{-3}	10	25	<i>This study</i>
<i>Bg100</i>	5.5	2.6×10^6	2×10^{-3}	10	25	<i>This study</i>
<i>Bg150</i>	10.5	1.2×10^6	2×10^{-3}	10	25	<i>This study</i>
<i>Kolb grey (Kg0)</i>	6.5	8.5×10^6	2×10^{-3}	10	25	<i>This study</i>
<i>Beck's black</i>	8.0	4.2×10^7	1×10^{-3}	10	25	<i>Schöpfer and Zulauf (2002)</i>
<i>Kolb brown</i>	5.8	2.23×10^7	4×10^{-3}	10	25	<i>Zulauf and Zulauf (2004)</i>

Table 4.1: Rheological data (*n*- and η -values) of plasticine used in the present study.

The results of constant strain-rate tests of the original *Kolb grey* and *Beck's green* plasticine/oil mixtures (50, 100, and 150 ml oil/kg) types, carried out at $T = 25^\circ\text{C}$, are presented in form of stress vs. strain plots (Fig. 4.1). The basic feature of all stress/strain curves is a steep slope at low strain, and a zone of yielding followed by almost steady state flow, the latter implying a small component of strain hardening. This increase of stress after yielding is almost linear in all plasticine types considered. It is obvious, that the stress exponent is proportional to the distances between the stress/strain curves at different strain

rates. The data of original *Beck's green* and *Kolb grey* plasticine show a wide range of the stress/strain curves indicating strong strain rate dependence of the stress (Fig. 4.1).

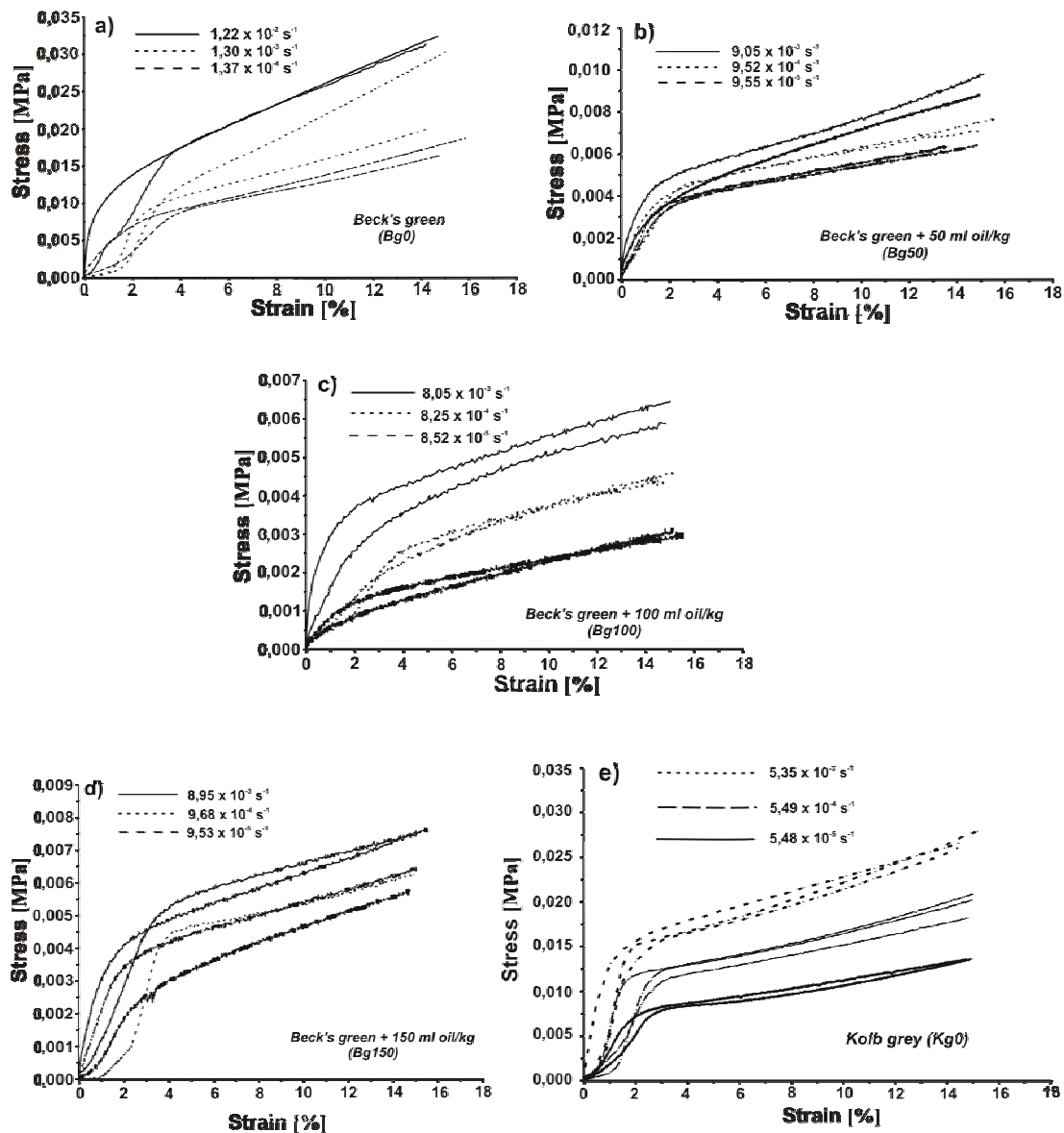


Fig. 4.1: Stress vs. strain plots for (a) *Beck's green* plasticine, (b,c,d) of *Beck's green* plasticine with different amounts of added white oil, (e) *Kolb grey* plasticine; $T = 25 \text{ }^{\circ}\text{C}$.

However, the striking feature of the stress/strain curves that is important when calculating n and C concerns the tangents at the curves at a certain strain. These tangents are not parallel. Assuming steady-state flow and taking the stress at 10% strain, a plot of \log_{10} stress vs. \log_{10} strain rate gives a straight line with slope n . From these plots, n is determined to be 7.9 for Bg0, 6.5 for Kg0, 13.5 for Bg50, 5.5 for Bg100 and 10.5 for Bg150 (Fig. 4.2).

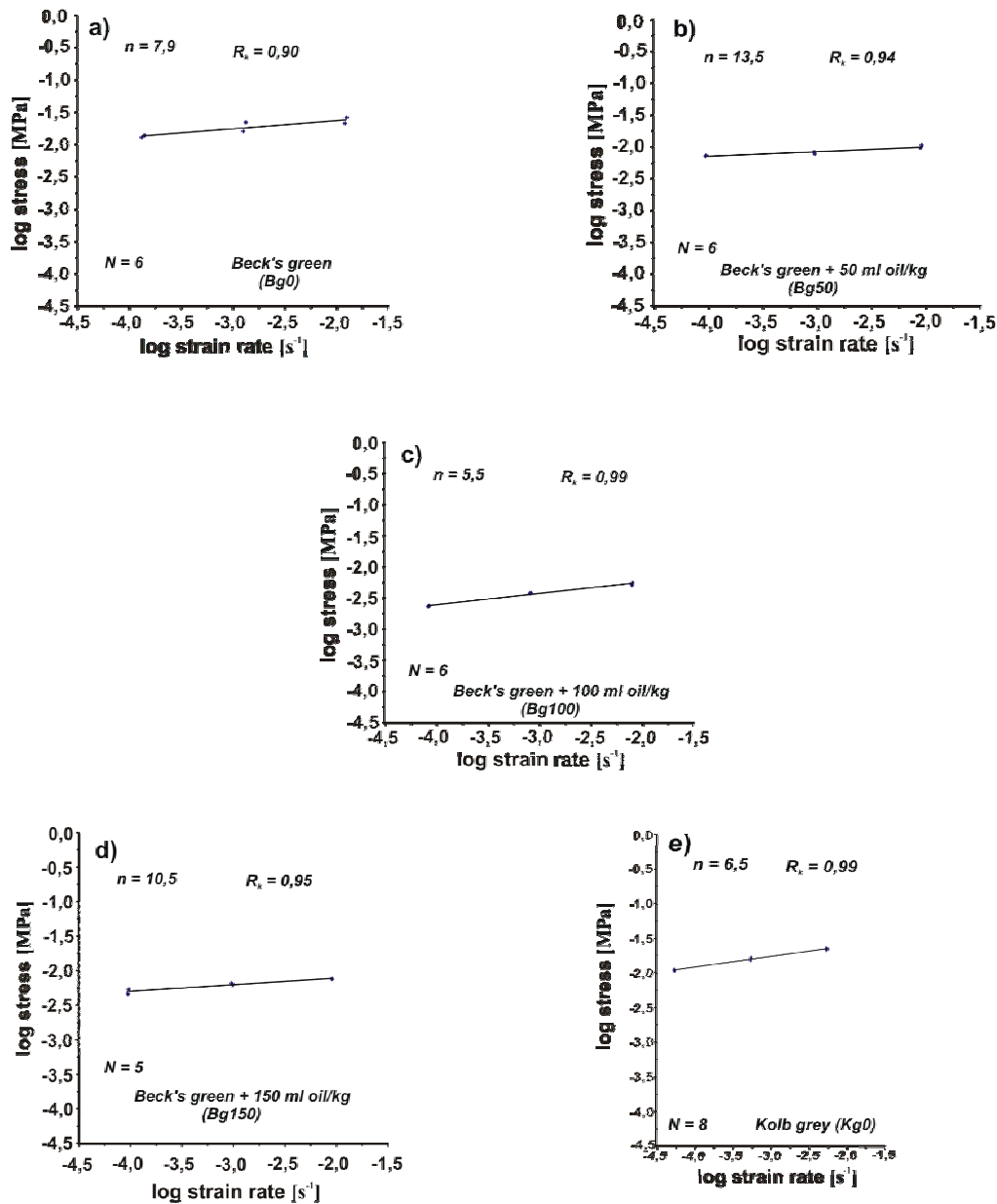


Fig. 4.2: log stress vs. log strain plots for (a) Beck's green plasticine, (b,c,d) of Beck's green plasticine with different amounts of added white oil, (e) Kolb grey plasticine; $T = 25\text{ }^{\circ}\text{C}$. R_k = regression coefficient, n = stress exponent, and N = number of runs.

According to equation [3-9], the apparent dynamic viscosity (at 10% strain and a strain rate of ca. $2 \times 10^{-3}\text{ s}^{-1}$) is $7.2 \times 10^6\text{ Pa s}$ for Bg0 (η_0), $6.8 \times 10^6\text{ Pa s}$ for Bg50 (η_{50}), $2.6 \times 10^6\text{ Pa s}$ for Bg100 (η_{100}) and $1.2 \times 10^6\text{ Pa s}$ for Bg150 (η_{150}) (Table 4.1). Although the n - and C - values are varying tremendously, the viscosities are surprisingly as expected: Addition of oil leads to a decrease in viscosity.

The apparent viscosity, η , and the stress exponent, n , of the black and green plasticine (supply June 2002) have been determined in previous studies. At a strain rate $\dot{\epsilon} = \text{ca. } 10^{-3} \text{ s}^{-1}$ and a finite strain $e = 10\%$, different supplies of original *Beck's green* plasticine are characterized by $\eta = 1.1 \times 10^7 - 7.2 \times 10^6 \text{ Pa s}$ and $n = 7.9 - 8.6$ (Zulauf and Zulauf, 2004; Table 4.1). The original *Beck's black* and *Kolb brown* plasticines show the following values: $\eta = 4.2 \times 10^7 \text{ Pa s}$ and $n = 8.0$ (Schöpfer and Zulauf, 2002) and $\eta = 2.23 \times 10^7 \text{ Pa s}$ and $n = 5.8$ (Zulauf and Zulauf, 2004), respectively.

4.2 Coeval folding and boudinage under plane strain with the axis of no change perpendicular to the layer

Plane-strain coaxial deformation of a competent plasticine layer embedded in an incompetent plasticine matrix was carried out to improve our understanding about the evolution of folds and boudins if the layer is oriented perpendicular to the Y -axis of the finite strain ellipsoid. The rock analogues used were *Beck's green* plasticine (matrix) and *Beck's black* plasticine (competent layer). Apart from strain-hardening effects, the viscosity of *Beck's black* plasticine, which formed the competent layer, was kept constant throughout the experiments. The viscosity of original *Beck's green* plasticine (termed Bg0), which formed the weak matrix, was partly modified by adding 50, 100 and 150 ml pharmaceutical white oil (liquid paraffin, made by DEA, Hamburg) to 1 kg warm (55°C) plasticine. The rheological data of the plasticine used are listed in Table 4.1. Four runs have been carried out using different viscosity ratios ($\eta_{\text{layer}}/\eta_{\text{matrix}} = \text{ca. } 1, \text{ ca. } 7, \text{ ca. } 20 \text{ and ca. } 35$) (Table 4.2). Moreover, the range in thicknesses of the competent layer employed in the experiments was in the range from 1 ± 0.2 to $10 \pm 0.2 \text{ mm}$ at 1 mm increments.

Fifty experimental runs have been carried out at a temperature T of 25°C and a strain rate $\dot{\epsilon}$ of $\text{ca. } 2 \times 10^{-3} \text{ s}^{-1}$ until a finite longitudinal strain of 30% was achieved. To investigate the geometry of the deformed competent layer, the specimen was cut in half along the X -axis.

One of the halves served for analysing the geometry of the boudins (XY -sections), the other half was used to examine the folds (YZ -sections) (Figs. 3.7 and 4.3).

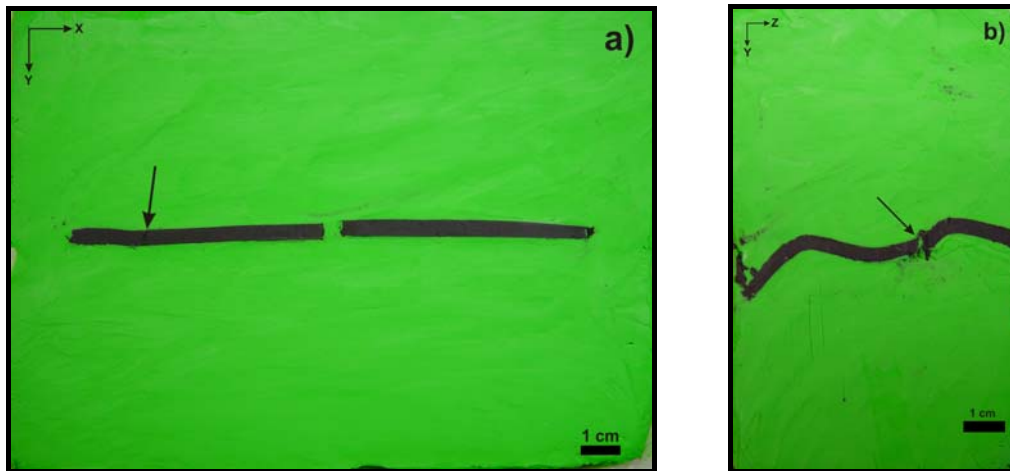


Fig. 4.3: Photograph of deformed competent layer of Beck's black plasticine embedded in matrix of modified Beck's green plasticine (Bg150) at a viscosity ratio of ca. 35; initial layer thickness = 2 ± 0.2 mm; arrow in a indicates initial neck; arrow in b indicates possible "pseudoboudin" that might result from oblique trend of necks.

Analyses of these sections include determination of: (i) finite layer thickness [H_f], (ii) length of boudins, (iii) maximum thickness of boudins, (iv) number of boudins, (v) shape of boudins, (vi) arc length of folds, (vii) number of folds, (viii) sharpness of fold hinges, and (ix) amplitude of folds. The average arc length of folds ($W_{a(fold)}$) was calculated by equation [2-7]. The results presented are based on averaged data from measurements of 50 cross (YZ) and longitudinal (XY) sections representing the fifty runs carried out using different viscosity ratios. The spacing of the single cuts was set at 1–3 cm. There was no problem in reassembling the YZ -sections in order to investigate the XY -sections. As the viscosity contrast between layer and matrix has a major impact on the geometry of the deformed competent layer (Fig. 4.4), the results below are listed with decreasing viscosity of the matrix plasticine (Table 4.2).

Layer	<i>Beck's black Plasticine</i>	<i>Beck's black Plasticine</i>	<i>Beck's black Plasticine</i>	<i>Beck's black Plasticine</i>
Matrix	<i>Beck's green Plasticine</i>	<i>Beck's green Plasticine + 50 ml oil/kg (Bg50)</i>	<i>Beck's green Plasticine + 100 ml oil/kg (Bg100)</i>	<i>Beck's green Plasticine + 150 ml oil/kg (Bg150)</i>
Viscosity ratio ($\eta_{layer}/\eta_{matrix}$)	<i>ca. 1</i>	<i>ca. 7</i>	<i>ca. 20</i>	<i>ca. 35</i>
Run	<i>4</i>	<i>3</i>	<i>2</i>	<i>1</i>

Table 4.2: Viscosity ratios of the different runs used in the present study.

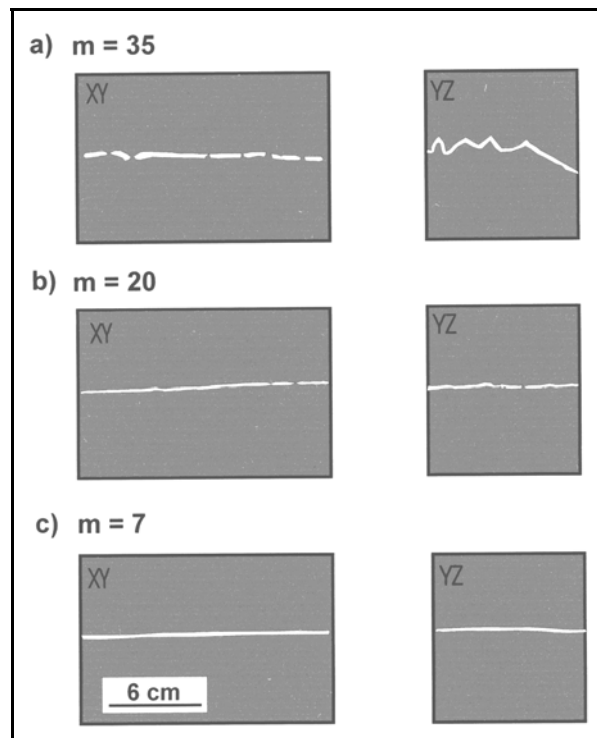


Fig. 4.4: Line drawing of deformed competent layer of Beck's black plasticine embedded in matrix of modified Beck's green plasticine at different viscosity ratios: *ca.* = 35 (a); *ca.* = 20 (b) and *ca.* = 7 (c); initial layer thickness = 1.0 ± 0.2 mm.

Twenty (2 x 10) runs have been carried out with a *viscosity ratio* of 35 and with thicknesses of the competent layer ranging from 1 ± 0.2 to 10 ± 0.2 mm at 1 mm increments. As expected, boudins formed in XY-sections (Figs. 4.3a, 4.4a), whereas folds developed in YZ-sections (Figs. 4.3b, 4.4a). In a few cases folded layers are not continuous (see arrow in Fig. 4.3b), which is attributed to the fact that some of the necks trend oblique to the principal strain axes.

With increasing layer thickness, the average arc length of folds (W_a), determined by equation [2-7], increases from ca. 35 to ca. 60 mm and the wavelength/thickness ratio (W_d) ranges from ca. 6 to ca. 11 (Fig. 4.5a; Table 4.3).

Viscosity ratio	H_i [mm]	H_f [mm]	H_f [%]	n_{folds}	$W_{a(fold)}$ [mm]	$W_{d(fold)}$	$n_{boudins}$	$W_{a(boudin)}$ [mm]	$W_{d(boudin)}$
ca. 35	1	3.3 ± 0.3	230	3.8 ± 0.8	35.7 ± 10.4	10.8	6.8 ± 1.1	31.3 ± 12.1	9.5
	2	4.0 ± 0.7	100	2.6 ± 0.7	43.3 ± 5.1	10.8	3.3 ± 0.5	45.7 ± 18.2	11.4
	3	5.6 ± 1.4	90	2.3 ± 0.5	50.7 ± 11.7	9.1	3.0 ± 0.6	50.5 ± 14.9	9.0
	4	6.9 ± 1.3	70	1.8 ± 0.4	55.5 ± 7.4	8.0	2.3 ± 0.4	55.7 ± 15.7	8.1
	5	9.2 ± 2.2	80	1.5 ± 0.5	57.2 ± 6.1	6.2	2.0 ± 0.7	58.3 ± 22.3	6.3
	6	10.4 ± 1.6	70	1.3 ± 0.4	60.2 ± 5.7	5.8	1.8 ± 0.4	65.4 ± 20.6	6.3
	7	11.0 ± 1.4	60	1	-	-	1	-	-
	8	12.3 ± 1.9	50	1	-	-	-	-	-
	9	13.0 ± 2.2	40	1	-	-	-	-	-
	10	21.2 ± 3.6	120	-	-	-	-	-	-
ca. 20	1	2.6 ± 0.7	160	1	-	-	2	46.5 ± 12.5	-
	2	3.6 ± 1.0	80	1	-	-	1	53.7 ± 5.8	-
	5	8.3 ± 1.3	70	-	-	-	-	-	-
	7	9.3 ± 0.9	30	-	-	-	-	-	-
	10	14.8 ± 0.7	50	-	-	-	-	-	-
ca. 7	1	1.1 ± 0.2	10	-	-	-	-	-	-
	2	2.2 ± 0.3	10	-	-	-	-	-	-
	5	5.2 ± 0.5	0	-	-	-	-	-	-
	7	7.3 ± 0.6	0	-	-	-	-	-	-
	10	8.9 ± 1.0	-10	-	-	-	-	-	-

Table 4.3: Finite thickness of deformed competent layer and geometrical parameters for folds and boudins at different initial layer thicknesses. H_i = initial thickness of competent layer, H_f = finite average thickness of deformed competent layer, $(\frac{H_f}{H_i} - 1) * 100$ = layer thickening in [%], n_{folds} = number of folds, $W_{a(fold)}$ = average fold arclength in YZ-sections, $W_{d(fold)}$ = average fold arclength/thickness, $n_{boudins}$ = number of boudins, $W_{a(boudin)}$ = average boudin wavelength in XY-sections and $W_{d(boudin)}$ = average boudin wavelength/thickness.

Moreover with increasing layer thickness the number of boudins ($n_{boudins}$) decreases from ca. 7 to ca. 2 and the length of boudins increases from ca. 30 to ca. 65 mm (Figs. 4.5a,b). According to our first quantification and statistical treatment, there is a clear tendency for the wavelength of both folds and boudins to be the same within uncertainty, which is actually quite large (Fig. 4.5a).

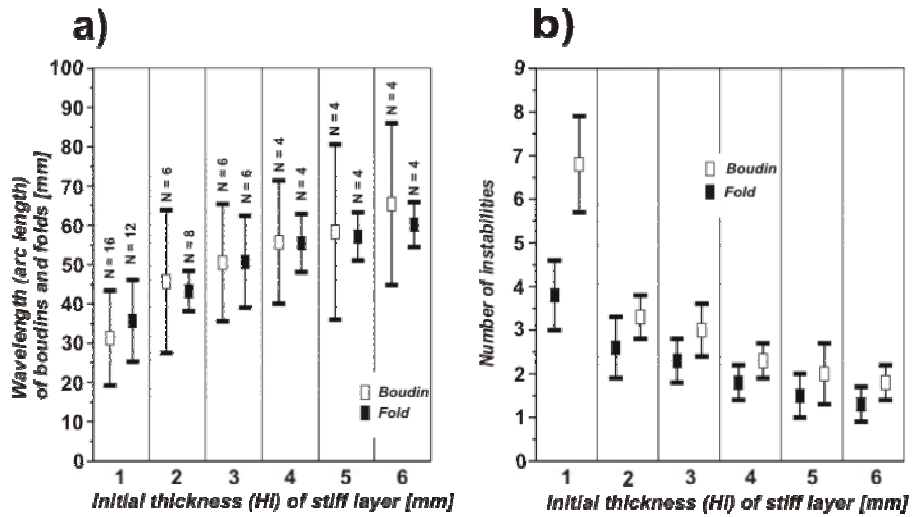


Fig. 4.5: Initial thickness of competent layer vs. wavelength (arc length) of boudins and folds (a) and initial thickness of competent layer vs. number of instabilities (b); viscosity ratio = ca. 35; N = number of data.

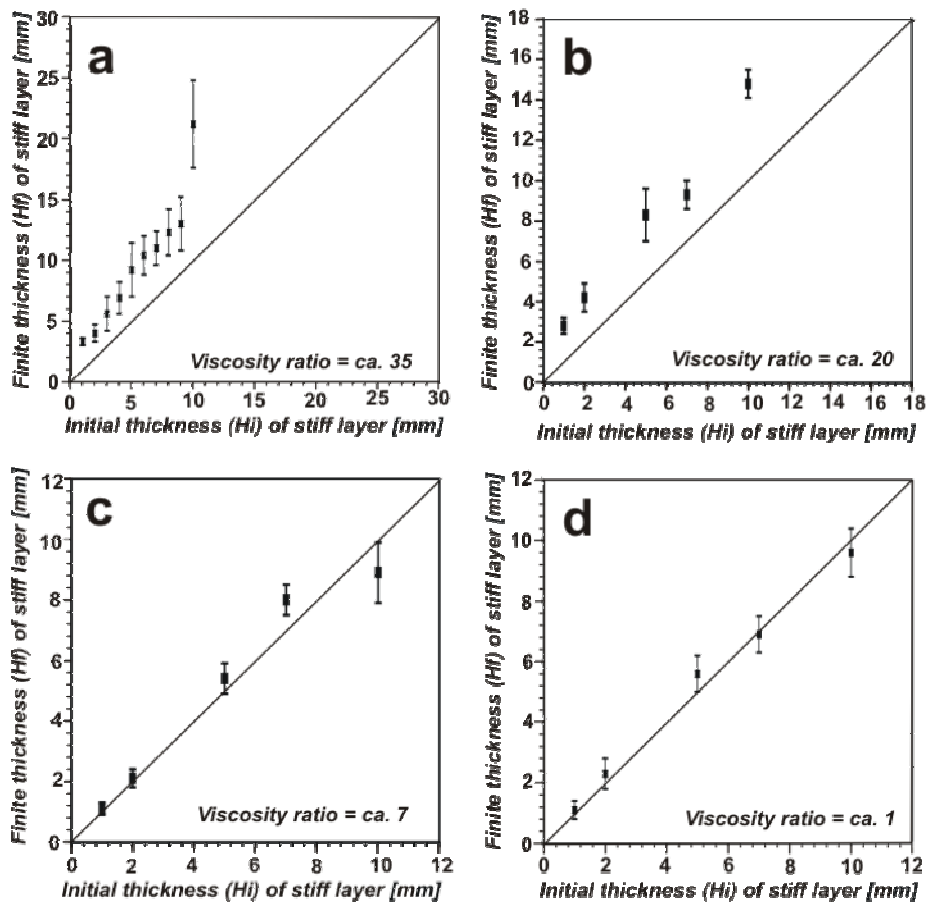


Fig. 4.6: Initial vs. finite thickness of competent layer at different viscosity ratios.

The ratio between finite and initial thickness of the competent layer (H_f/H_i) ranges from 1.4 to 3.3, meaning that the thickness of the competent layer (maximum thickness of boudins)

increased considerably by 40 – 230% (Fig. 4.6a; Table 4.3). The effect of layer thickness on fold geometry is shown in Fig. 4.7.

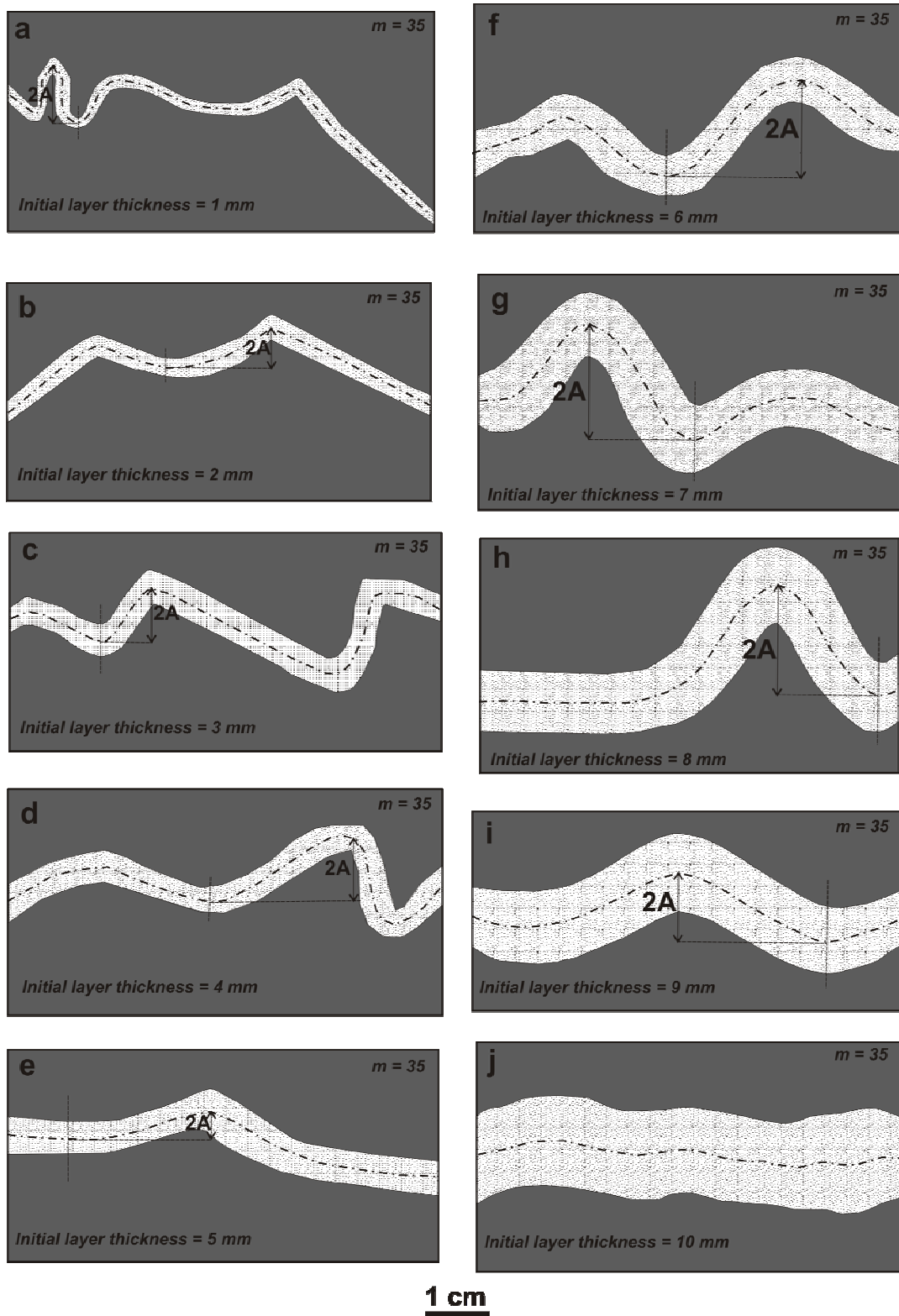


Fig. 4.7: Change in deformation geometry with thickness of layer of Beck's black plasticine embedded in matrix of Beck's green plasticine + 150 ml oil/kg; $m = 35$; $e = 30\%$.

At a *viscosity ratio* of 20, ten runs have been carried out using thicknesses of the competent layer of 1, 2, 5, 7, and 10 ± 0.2 mm. In the *YZ*-sections, weak folding is observed, characterized by large wavelengths and low amplitudes. Boudinage appears to have developed from pinch and swell structures. With increasing layer thickness, the number of boudins ($n_{boudins}$) decreases from 2 to 1 and the length of boudins increases from ca. 47 to ca. 54 mm (Table 4.3). However, at both ends of *XY*-sections the layer is surrounded by the matrix, suggesting that the weak matrix flowed much faster than the competent layer. These observations imply significant boundary effects, which are attributed to the fact that the sample is not confined and can flow without resistance along the *X*-axis. The degree of layer thickening ranges from 50 to 160% (Fig. 4.6b, Table 4.3).

At a *viscosity ratio* of 7, ten runs have been carried out using thicknesses of the competent layer of 1, 2, 5, 7, and 10 ± 0.2 mm. There is no evidence for folding and for boudinage, and the ends of the layers are hardly surrounded by the matrix. There is almost no change in thickness of the competent layer as is indicated by the H_f/H_i ratio that ranges from 0.9 to 1.1, equivalent to $\pm 10\%$ thickening (Fig. 4.6c).

In cases where the specimen does not show a competence contrast between layer and matrix (*viscosity ratio* = ca. 1), ten runs have been carried out using thicknesses of the competent layer of 1, 2, 5, 7, and 10 ± 0.2 mm. Homogeneous deformation occurs without folding in the *YZ*-sections and boudinage in the *XY*-sections. There is almost no change in thickness of the competent layer as is indicated by the H_f/H_i ratio that is ranging from 1.0 to 1.2, equivalent to $\pm 15\%$ thickening (Fig. 4.6d).

4.3 The impact of strain rate on folding and boudinage under plane strain

To demonstrate the impact of varying strain rates on growing folds and boudins under plane strain, we investigated a stiff layer, with viscosity η_2 and stress exponent n_2 , that was

embedded in a weak matrix, with viscosity η_l and stress exponent n_l . The stiff layer and matrix consist of non-linear viscous *Kolb grey* and *Beck's green* plasticine, respectively. The effective viscosity (η) of the matrix plasticine was partly modified by adding oil to the original plasticine. The rheological data of the plasticine are listed in Table 4.1. At the strain rates used in the experiments the viscosity ratio between layer and matrix ranges between 3 and 10. Different runs have been carried out where the layer was oriented perpendicular to the principal strain axes ($X>Y>Z$). In the three deformation regimes, the initial layer thickness (H_i) was set at 1.0 ± 0.2 mm. As there was an unexpected layer thickening in cases where the layer was oriented perpendicular to the minor principal axis of the strain ellipsoid Z , we carried out additional runs at different finite strains (5, 10, 20, 30, 40%) using the same material for matrix and layer with an initial thickness of the stiff layer (H_i) at 2.0 ± 0.2 mm.

4.3.1 Stiff layer perpendicular to the long axis of the finite strain ellipsoid ($S \perp X$)

In cases where the layer is oriented perpendicular to the long axis X of the finite strain ellipsoid, folds have formed in XZ sections (Fig. 4.8). If the strain rate is ranging from $7.9 \times 10^{-6} \text{ s}^{-1}$ to $1.1 \times 10^{-3} \text{ s}^{-1}$, enlargement of the strain rate results in a slight decrease in the number of folds (n_{folds}), ranging from ca. 4 to ca. 3 (Fig. 4.9a; Table 4.4). The arc length of the folds is the same within uncertainties (ca. 21mm; Table 4.4; Fig. 4.9b). There is only a weak increase of the mean value with increasing strain rate. If $\dot{\epsilon} < 1.1 \times 10^{-3} \text{ s}^{-1}$ the ratio between apparent finite and initial thickness of the stiff layer (H_f/H_i) decreases with increasing strain rate from 3.1 to 2.3, meaning that the apparent thickness of the stiff layer increased considerably by 130 – 210% (Table 4.4; Fig. 4.10). The wavelength/thickness ratio (W_d) ranges from ca. 7 to ca. 9 (Table 4.4; Fig. 4.11).

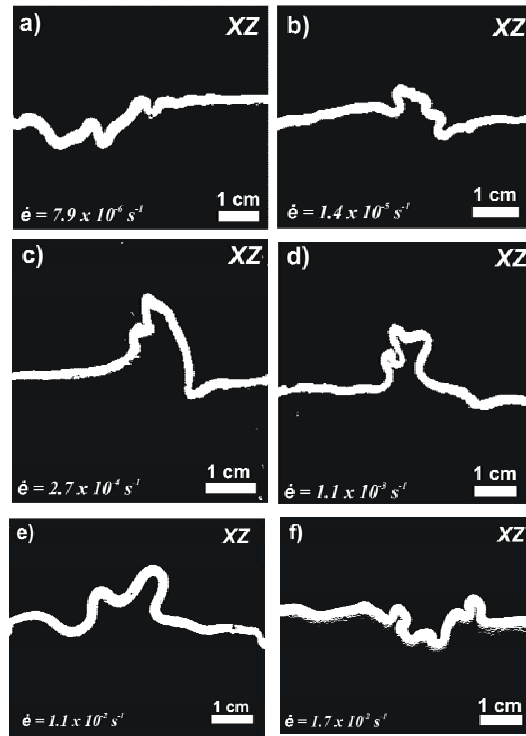


Fig. 4.8: XZ sections showing folding of the stiff layer with the layer initially perpendicular to the long X axis of the finite strain ellipsoid; strain rates used are indicated; $e = 40\%$; initial layer thickness = $1.0 \pm 0.2 \text{ mm}$.

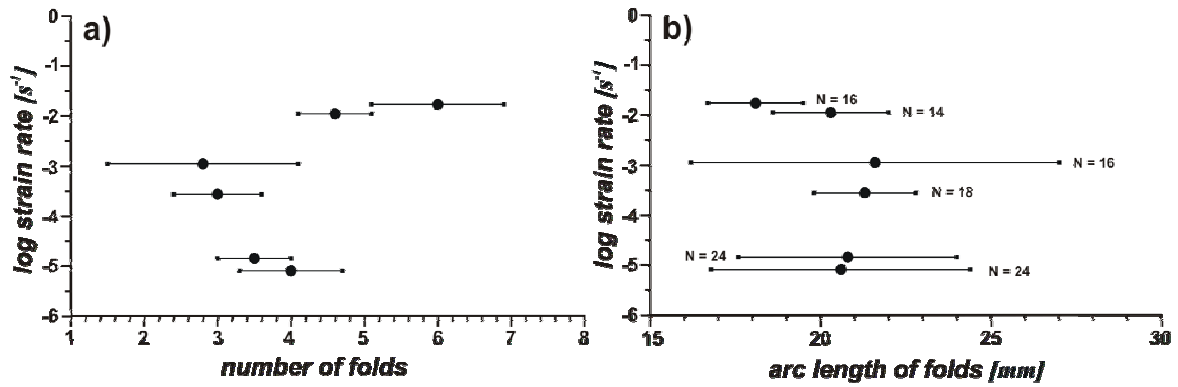


Fig. 4.9: Number and length of instabilities vs. log strain rate in case where the stiff layer is perpendicular to the long X-axis of the finite strain ellipsoid; $e = 40\%$; initial layer thickness = $1.0 \pm 0.2 \text{ mm}$.

If $\dot{\epsilon} > 1.1 \times 10^{-3} \text{ s}^{-1}$ enlargement of the strain rate results in a significant increase in the number of folds (n_{folds}), ranging from ca. 3 to ca. 6 (Fig. 4.9a; Table 4.4), and a corresponding decrease of the arc length of the folds, the latter ranging from ca. 20 to ca. 18 (Table 4.4; Fig. 4.9b).

Strain rate [s^{-1}]	H_i [mm]	H_f [mm]	H_f [%]	n_{folds}	$W_{a(fold)}$ [mm]	$W_{d(fold)}$	Thickness of fold hinge [mm]	Thickness of fold limb [mm]
7.9×10^{-6}	1.0 ± 0.2	3.1 ± 0.7	210	4.0 ± 0.7	20.6 ± 3.8	6.6 ± 1.2	3.3 ± 0.5	3.0 ± 0.4
1.4×10^{-5}	1.0 ± 0.2	2.9 ± 0.6	190	3.5 ± 0.5	20.8 ± 3.2	7.2 ± 1.1	3.1 ± 0.3	2.7 ± 0.2
2.7×10^{-4}	1.0 ± 0.2	2.5 ± 0.7	150	3.0 ± 0.6	21.3 ± 1.5	8.5 ± 0.6	2.7 ± 0.5	2.5 ± 0.3
1.1×10^{-3}	1.0 ± 0.2	2.3 ± 0.5	130	2.8 ± 1.3	21.6 ± 5.4	9.4 ± 2.4	2.4 ± 0.2	2.3 ± 0.4
1.1×10^{-2}	1.0 ± 0.2	2.5 ± 0.4	150	4.6 ± 0.5	20.3 ± 1.7	8.1 ± 0.5	2.7 ± 0.4	2.6 ± 0.3
1.7×10^{-2}	1.0 ± 0.2	2.4 ± 0.3	140	6.0 ± 0.9	18.1 ± 1.4	7.5 ± 0.6	2.6 ± 0.3	2.5 ± 0.2

Table 4.4: Geometrical parameters of folds with the stiff layer perpendicular to the long axis (X) of the finite strain ellipsoid; initial layer thickness = 1.0 ± 0.2 mm. H_i = initial thickness of competent layer, H_f = finite average thickness of deformed competent layer, $H_f\%$ = layer thickening in [%], n_{folds} = number of folds, $W_{a(fold)}$ = average fold arclength in XZ -sections, $W_{d(fold)} = W_{a(fold)} / H_f$.

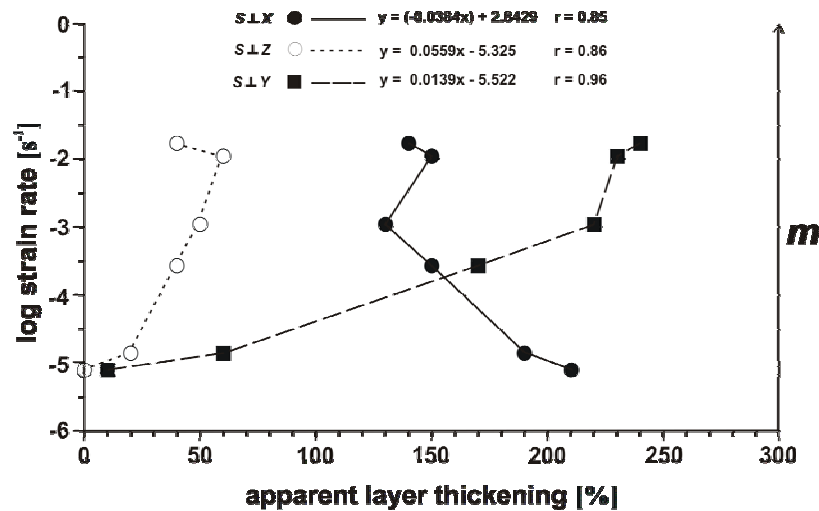


Fig. 4.10: Thickening of stiff layer vs. log strain rate. All runs under plane strain with the layers perpendicular to the X , Y and Z axis of the finite strain ellipsoid, respectively; $e = 40\%$; initial layer thickness = 1.0 ± 0.2 mm. Functions and correlation coefficient, r , are represented, m = viscosity contrast (η_2/η_1).

The wavelength/thickness ratio (W_d) decreases from ca. 10 to ca. 8 (Table 4.4; Fig. 4.11). The ratio between apparent finite and initial thickness of the stiff layer (H_f/H_i) is more or less the same within uncertainties to that acquired with a strain rate, $\dot{\epsilon} = 2.7 \times 10^{-4} s^{-1}$ (Table 4.4; Fig. 4.10).

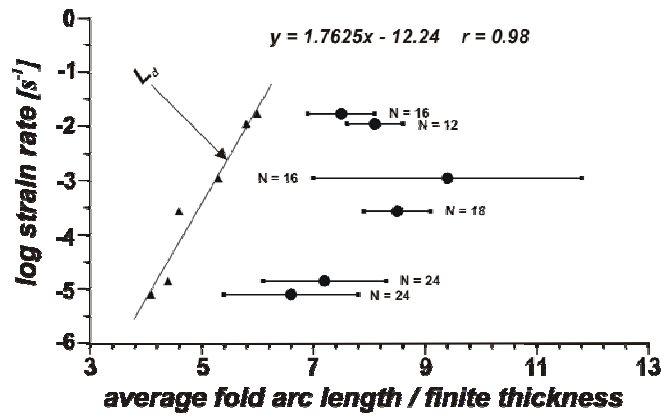


Fig.4.11: Normalized wavelength (arc length) of folds vs. log strain rate in cases where the stiff layer is perpendicular to the long axis (X) of the finite strain ellipsoid; $e = 40\%$; initial layer thickness = 1.0 ± 0.2 mm.

4.3.2 Stiff layer perpendicular to the short axis of the finite strain ellipsoid ($S \perp Z$)

If the layer is oriented perpendicular to the short axis (Z) of the finite strain ellipsoid, boudins have formed in XZ sections. Some of the boudins appear to have developed from pinch and swell structures (Fig. 4.12).

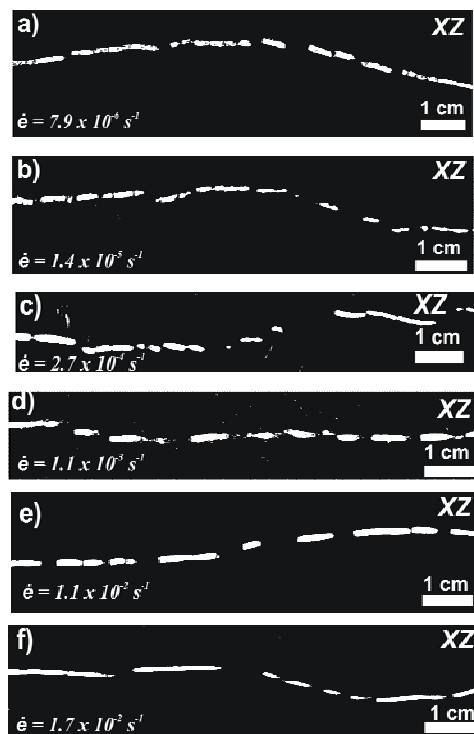


Fig. 4.12: XZ sections showing boudinage of the stiff layer with the layer initially perpendicular to the short axis (Z) of the finite strain ellipsoid; strain rates used are indicated; $e = 40\%$; initial layer thickness = 1.0 ± 0.2 mm.

There is a clear relation between strain rate and geometric parameters, although the latter show a large uncertainty. If $\dot{\epsilon} < 1.1 \times 10^{-3} \text{ s}^{-1}$, the average number of boudins (n_{boudins}) increases with increasing strain rate from ca. 8 to ca. 12 (Table 4.5; Fig. 4.13a), whereas the length of boudins decreases from ca. 11 to ca. 8 mm (Fig. 4.13b; Table 4.5). If $\dot{\epsilon} > 1.1 \times 10^{-3} \text{ s}^{-1}$, enlargement of the strain rate results in a slight decrease in the number of boudins (n_{boudins}), ranging from ca. 12 to ca. 10 (Fig. 4.13a; Table 4.5), and an increase in the length of boudins, the latter ranging from ca. 8 to ca. 11 is indicated, at increasing strain rates (Table 4.5; Fig. 4.13b).

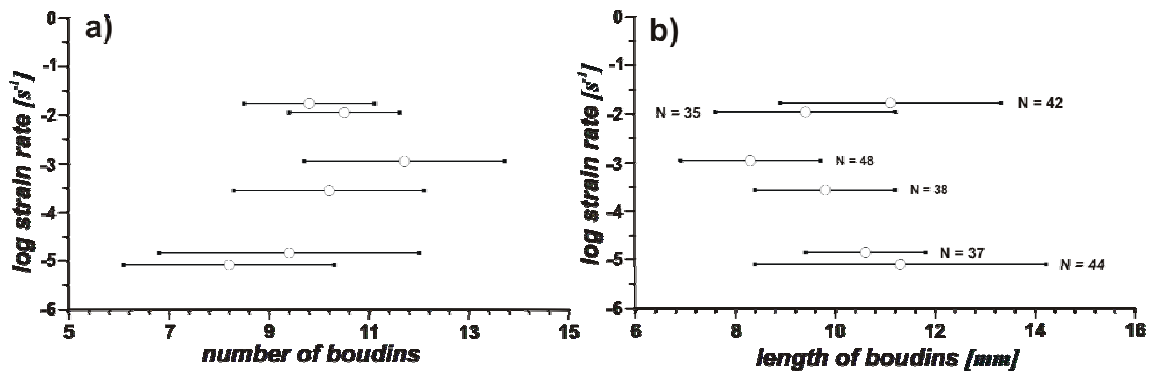


Fig. 4.13: Number and length of boudins vs. log strain rate in cases where the stiff layer is perpendicular to the short axis (Z) of the finite strain ellipsoid; $e = 40\%$; initial layer thickness = $1.0 \pm 0.2 \text{ mm}$.

Strain rate [s^{-1}]	H_i [mm]	H_f [mm]	H_f [%]	n_{boudins}	$W_{a(\text{boudin})}$ [mm]	$W_{d(\text{boudin})}$
7.9×10^{-6}	1.0 ± 0.2	1.0 ± 0.2	0	8.2 ± 2.1	11.3 ± 2.9	11.3 ± 2.9
1.4×10^{-5}	1.0 ± 0.2	1.2 ± 0.3	20	9.4 ± 2.6	10.6 ± 1.2	8.8 ± 1.0
2.7×10^{-4}	1.0 ± 0.2	1.4 ± 0.4	40	10.2 ± 1.9	9.8 ± 1.4	7.0 ± 1.0
1.1×10^{-3}	1.0 ± 0.2	1.5 ± 0.4	50	11.7 ± 2.0	8.3 ± 1.4	5.5 ± 0.8
1.1×10^{-2}	1.0 ± 0.2	1.6 ± 0.3	60	10.5 ± 1.1	9.4 ± 1.8	5.9 ± 1.1
1.7×10^{-2}	1.0 ± 0.2	1.4 ± 0.4	40	9.8 ± 1.3	11.1 ± 2.2	7.9 ± 1.7

Table 4.5: Geometrical parameters of boudins with the stiff layer perpendicular to the short axis (Z) of the finite strain ellipsoid; initial layer thickness = $1.0 \pm 0.2 \text{ mm}$. H_i = initial thickness of competent layer, H_f = finite average thickness of deformed competent layer, H_f = layer thickening in [%], n_{boudins} = number of boudins, $W_{a(\text{boudin})}$ = average boudin wavelength in XZ-sections, $W_{d(\text{boudin})} = W_{a(\text{boudin})} / H_f$.

The ratio between apparent finite and initial thickness of the stiff layer (H_f/H_i) ranges from 1.0 to 1.6, meaning that with increasing strain rate the apparent thickness of the stiff layer

increased from 0 to 60% (Fig. 4.10; Table 4.5). The wavelength/thickness ratio (W_d) ranges from ca. 11 to ca. 6 (Table 4.5; Fig. 4.14).

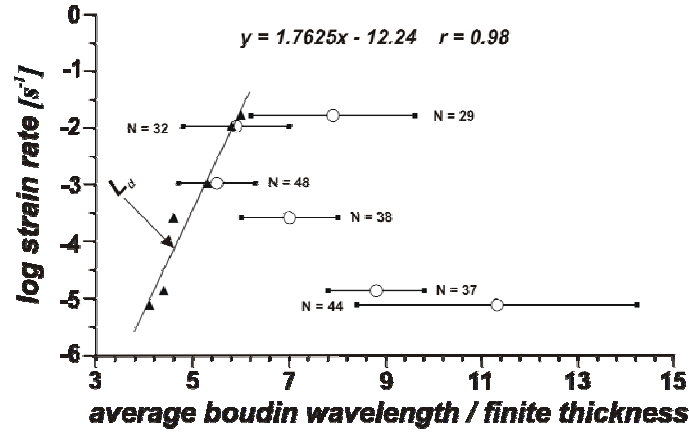


Fig.4.14: Normalized wavelength of boudins vs. log strain rate in cases where the stiff layer is perpendicular to the short Z-axis of the finite strain ellipsoid; $e = 40\%$; initial layer thickness = 1.0 ± 0.2 mm.

In order to evaluate the magnitude of finite strain at the time when the thickening of the initial stiff layer starts, we have carried out another series of experiments with an initial thickness of the stiff layer (H_i) at 2.0 ± 0.2 mm (Table 4.6).

Strain [%]	H_i [mm]	H_f [mm]	H_f [%]	H_b [mm]	$n_{boudins}$	$W_{a(boudin)}$ [mm]	$W_{d(boudin)}$	l_o [mm]	l_x [mm]	e_x	V_o [mm ³]	V [mm ³]	ΔV
5	2.0 ± 0.2	2.3 ± 0.5	15	-	0	-	-	120 ± 0.2	121.0 ± 0.8	0.013 ± 0.004	28 800	-	-
10	2.0 ± 0.2	2.4 ± 0.3	20	2.1 ± 0.3	2.7 ± 0.5	9.0 ± 5.0	3.8 ± 1.2	120 ± 0.2	123.3 ± 1.7	0.028 ± 0.014	28 800	31072 ± 740	0.079 ± 0.026
20	2.0 ± 0.2	2.6 ± 0.4	30	2.1 ± 0.4	3.5 ± 0.5	11.7 ± 2.5	4.5 ± 0.8	120 ± 0.2	125.9 ± 2.7	0.049 ± 0.010	28 800	31727 ± 1234	0.102 ± 0.043
30	2.0 ± 0.2	2.8 ± 0.3	40	2.2 ± 0.5	6.3 ± 0.4	13.0 ± 0.7	4.6 ± 0.2	120 ± 0.2	128.0 ± 3.6	0.067 ± 0.030	28 800	33792 ± 1536	0.173 ± 0.053
40	2.0 ± 0.2	3.1 ± 0.2	55	2.3 ± 0.7	6.8 ± 0.8	14.9 ± 0.4	4.8 ± 0.2	120 ± 0.2	130.2 ± 3.0	0.085 ± 0.021	28 800	35935 ± 3827	0.248 ± 0.133

Table 4.6: Geometrical parameters of boudins with the stiff layer perpendicular to the short (Z) axis of the finite strain ellipsoid; initial layer thickness = 2.0 ± 0.2 mm. H_i = initial thickness of competent layer, H_f = finite average maximum thickness of deformed competent layer, H_f = layer thickening in [%], H_b = average boudin thickness of deformed competent layer, $n_{boudins}$ = number of boudins, $W_{a(boudin)}$ = average boudin wavelength in XZ-sections, $W_{d(boudin)} = W_{a(boudin)} / H_f$, l_o = initial length of competent layer, l_x = finite average length of deformed competent layer without necks, e_x = viscous extensional strain, V_o = volume of undeformed layer, V = volume of deformed layer, ΔV = volume strain.

The results based on averaged data from measurements of thirty longitudinal (XZ) sections representing the thirty runs carried out using incremental deformation studies have shown that significant layer thickening predates the formation of boudins that reach its maximum volume at 10% strain (Table 4.6). With increasing strain, the average number of boudins ($n_{boudins}$) and the length of boudins increases from ca. 0 to ca. 7 (Table 4.6; Fig. 4.15b) and from ca. 9 to ca. 15 mm (Fig. 4.15c; Table 4.6), respectively.

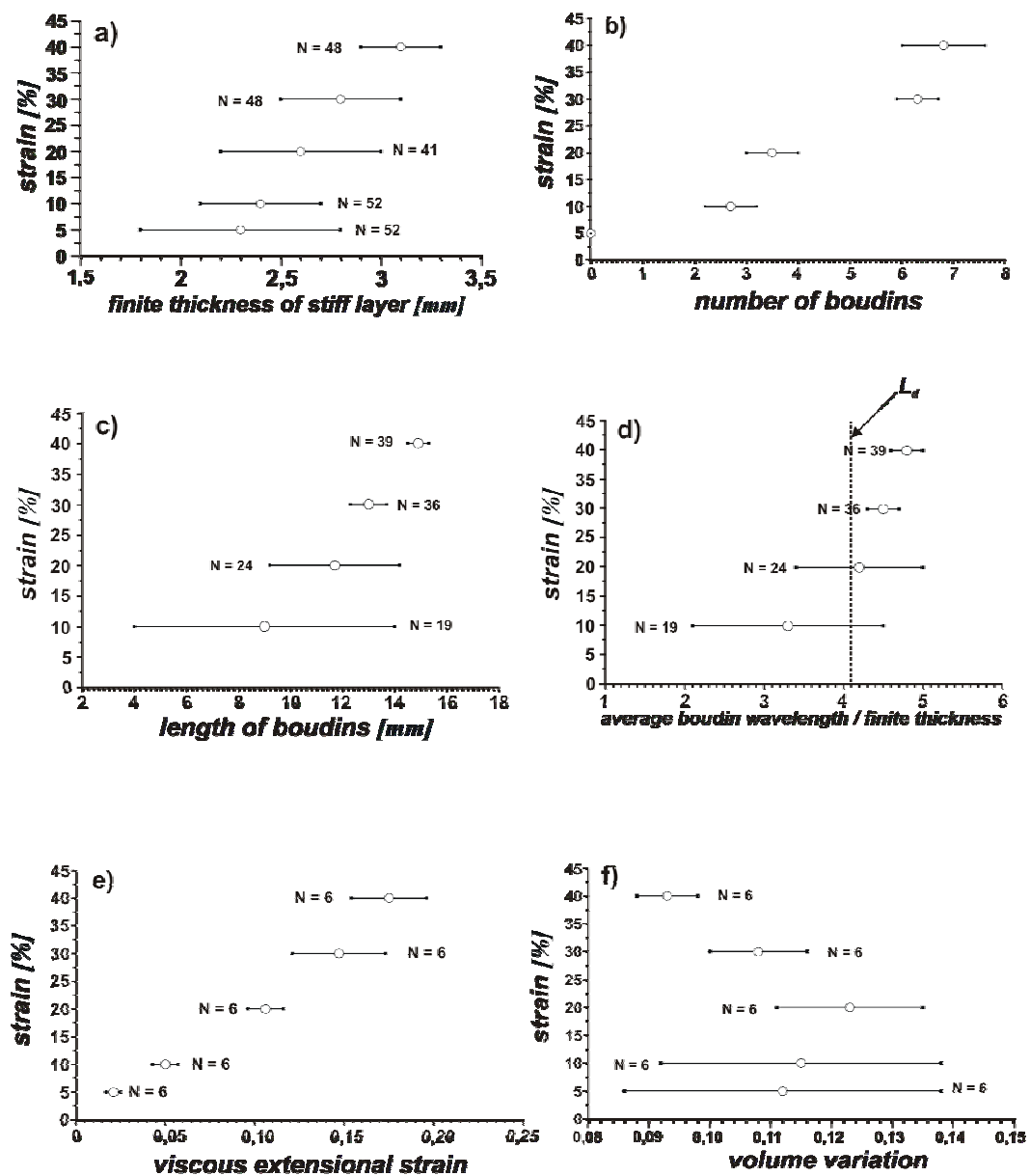


Fig. 4.15: Diagrams showing the strain-dependent evolution of geometrical parameters of boudins, which result from plane strain-coaxial deformation with the stiff layer perpendicular to the minor (Z) axis of the finite strain ellipsoid, initial layer thickness = 2.0 ± 0.2 mm and $\dot{\epsilon} = 1.1 \times 10^{-3} \text{ s}^{-1}$; (a,b) finite thickness of stiff layer and number of boudins vs. strain; (c,d) length and normalized wavelength of boudins vs. strain; (e,f) viscous extensional strain of layer and volume variation vs. strain.

The ratio between finite and initial thickness of the stiff layer (H_f/H_i) ranges from 2.3 to 3.1 meaning that the thickness of the stiff layer (maximum thickness of boudins) increased considerably by 15 – 55% (Fig. 4.15a; Table 4.6). The wavelength/thickness ratio (W_d) ranges from ca. 3 to ca. 5 (Table 4.6; Fig. 4.15d). The viscous extensional strain of the layer (e_x) ranges from 0.01 to 0.09, meaning that the deformed competent stiff layer extended from 1 to 10% throughout the deformation (Fig. 4.15e; Table 4.6). The volume strain of the layer (ΔV) increases with the bulk strain, ranging from 0.079 to 0.248 (Table 4.6; Fig. 4.15f).

4.3.3 Stiff layer perpendicular to the intermediate axis of the finite strain ellipsoid ($S \perp Y$)

If the stiff layer is oriented perpendicular to the Y -axis of the finite strain ellipsoid, there is no evidence for folding and boudinage at low ($\dot{\epsilon} = 7.9 \times 10^{-6} \text{ s}^{-1}$) and higher ($1.1 \times 10^{-2} \text{ s}^{-1} \leq \dot{\epsilon} \leq 1.7 \times 10^{-2} \text{ s}^{-1}$) strain rates (Table 4.7).

Strain rate [s^{-1}]	H_i [mm]	H_f [mm]	H_f [%]	n_{folds}	$W_{a(\text{fold})}$ [mm]	$W_{d(\text{fold})}$	n_{boudins}	$W_{a(\text{boudin})}$ [mm]	W_d (boudin)
7.9×10^{-6}	1.0 ± 0.2	1.1 ± 0.4	10	0	-	-	0	-	-
1.4×10^{-5}	1.0 ± 0.2	1.6 ± 0.6	60	1.8 ± 0.4	13.3 ± 1.2	8.3 ± 0.8	3.2 ± 0.4	26.6 ± 14.6	16.6 ± 9.1
2.7×10^{-4}	1.0 ± 0.2	2.7 ± 0.7	170	1.3 ± 0.4	48.8 ± 2.6	18.1 ± 1.0	2.0 ± 0.6	98 ± 30.0	36.3 ± 11.1
1.1×10^{-3}	1.0 ± 0.2	3.2 ± 0.7	220	1.0 ± 0.0	52.2 ± 8.5	16.3 ± 2.6	1.2 ± 0.4	105 ± 24.0	32.8 ± 7.5
1.1×10^{-2}	1.0 ± 0.2	3.3 ± 0.2	230	0	-	-	0	-	-
1.7×10^{-2}	1.0 ± 0.2	3.4 ± 0.2	240	0	-	-	0	-	-

Table 4.7: Geometrical parameters for folds and boudins with the stiff layer perpendicular to the intermediate (Y) axis of the finite strain ellipsoid; H_i = initial thickness of competent layer, H_f = finite average thickness of deformed competent layer, H_f = layer thickening in [%], n_{folds} = number of folds, $W_{a(\text{fold})}$ = average fold arclength in YZ -sections, $W_{d(\text{fold})} = W_{a(\text{fold})} / H_f$, n_{boudins} = number of boudins, $W_{a(\text{boudin})}$ = average boudin wavelength in XY -sections, $W_{d(\text{boudin})} = W_{a(\text{boudin})} / H_f$.

At strain rates between the above values, the layer shows pinch-and-swell as well as boudinage structures in XY sections, whereas the YZ sections show weak folding (Fig. 4.16).

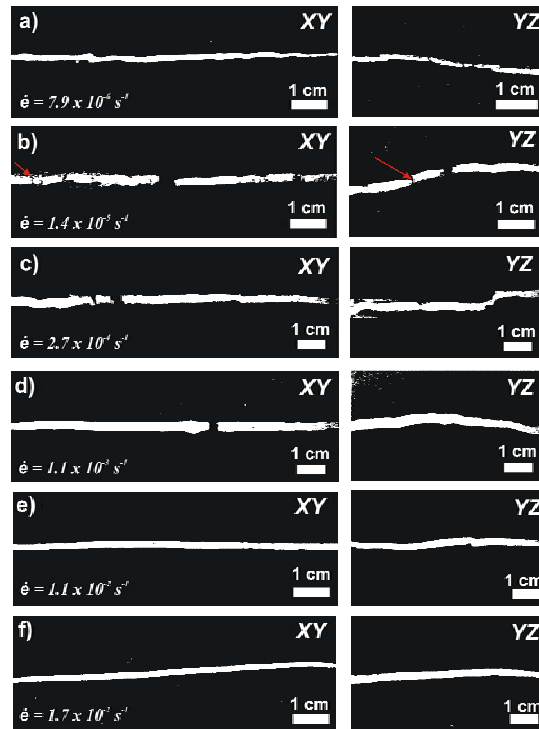


Fig. 4.16: XZ - and YZ -sections showing folding and boudinage of the stiff layer with the layer perpendicular to the intermediate axis (Y) of the finite strain ellipsoid; strain rates used are indicated; $e = 40\%$; initial layer thickness = 1.0 ± 0.2 mm; arrow in (a) indicates initial neck; arrow in (b) indicates possible “pseudoboudin” that might result from oblique trend of necks.

The ratio between apparent finite and initial thickness of the stiff layer (H_f/H_i) in this experimental run ranges from 1.1 to 3.4, meaning that with increasing strain rate the apparent finite thickness of the stiff layer (maximum thickness of boudins) increased considerably from 10 to 240% during deformation (Table 4.7; Fig. 4.10). The degree of thickening decreased if $\dot{\epsilon} > 1.1 \times 10^{-3} \text{ s}^{-1}$. Folds are characterized by large wavelengths. In a few cases folded layers are not continuous (see arrow in Fig. 4.16) which is attributed to the fact that some of the necks are trending oblique to the principal strain axes (“pseudo-boudinage”, Zulauf et al., 2003). Despite the large uncertainties of the geometrical parameters, there is a clear relation between strain rate and number of folds and boudins. Enlargement of the strain rate results in a slight decrease of the number of folds (n_{folds}), ranging from ca. 2 to ca. 1 (Fig. 4.17a; Table 4.7) and

a large increase of the average arc length of folds (W_d) from ca. 13 to ca. 52 mm (Table 4.7; Fig. 4.17b).

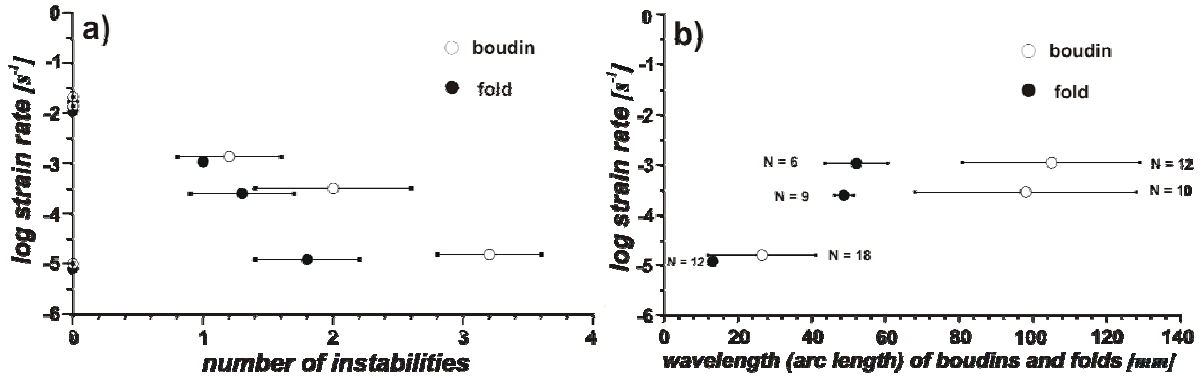


Fig. 4.17: Number and length of instabilities vs. log strain rate in cases where the stiff layer is perpendicular to the intermediate Y-axis of the finite strain ellipsoid; $e = 40\%$; initial layer thickness = 1.0 ± 0.2 mm.

The wavelength/thickness ratio (W_d) of folds ranges from ca. 8 to ca. 18 (Fig. 4.18; Table 4.7). With increasing strain rate the number of boudins ($n_{boudins}$) decreases from ca. 3 to ca. 1 (Fig. 4.17a; Table 4.7) and the length of boudins increases from ca. 27 to ca. 105 mm (Fig. 4.17b; Table 4.7). The wavelength/thickness ratio (W_d) ranges from ca. 17 to ca. 36 (Fig. 4.18; Table 4.7).

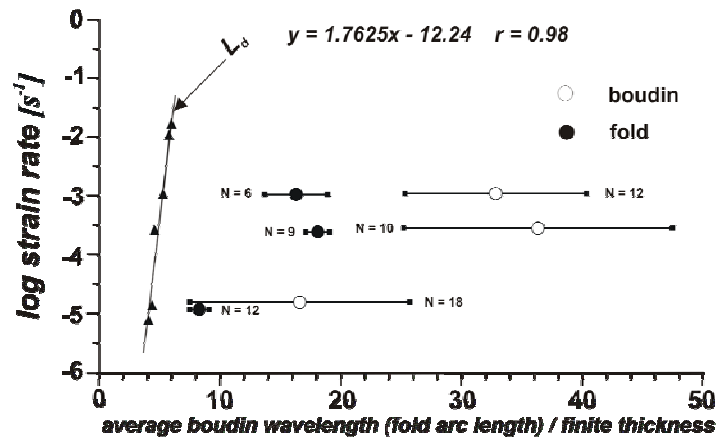


Fig. 4.18: Normalized wavelength (arc length) of boudins and folds vs. log strain rate in cases where the stiff layer is perpendicular to the intermediate axis (Y) of the finite strain ellipsoid; $e = 40\%$; initial layer thickness = 1.0 ± 0.2 mm.

4.4 Coeval folding and boudinage under plane strain through space and time

Results of theoretical studies (cf. Ramberg, 1959; Ramsay, 1967, Fig. 3-54; Weijermars, 1997, Fig. 14-24b) and analogue scale-model experiments (Zulauf et al., 2003; this study), suggest that during one single deformation event plane-strain coaxial deformation with the layer oriented perpendicular to the Y -axis of the finite strain ellipsoid seems to be suitable for producing coeval folds and boudins in non-linear viscous material. As the results of previous 3D-studies are based only on finite deformation structures, they cannot be used to prove if both structures grew simultaneously or in sequence.

In the present experimental study the impact of plane strain on the deformation structures of rheologically stratified analogue material was investigated in 4D. Plane strain acted on a single stiff layer that was embedded in a weak matrix, with the layer oriented perpendicular to the intermediate Y -axis of the finite strain ellipsoid. The layer consisted of *Kolb brown* plasticine. The matrix was made of *Beck's green* Plasticine. Contrary to the viscosity of the stiff layer, which was kept constant throughout the experiments, the effective viscosity (η) of the matrix plasticine was partly modified by adding oil to the original plasticine. The experiments have been carried out with a viscosity contrast m of 18.6. For details of the rheological parameters of the plasticine, see Table 4.1.

To study the geometry of the deformed stiff layer in 3D, without destroying (cutting) the sample, and the impact of stress relaxation due to deformation interruption, two different experimental runs have been carried out using computer tomography (CT). The first run was carried out without interruption. During the second run the deformation was stopped in each case at increments of 10% longitudinal strain.

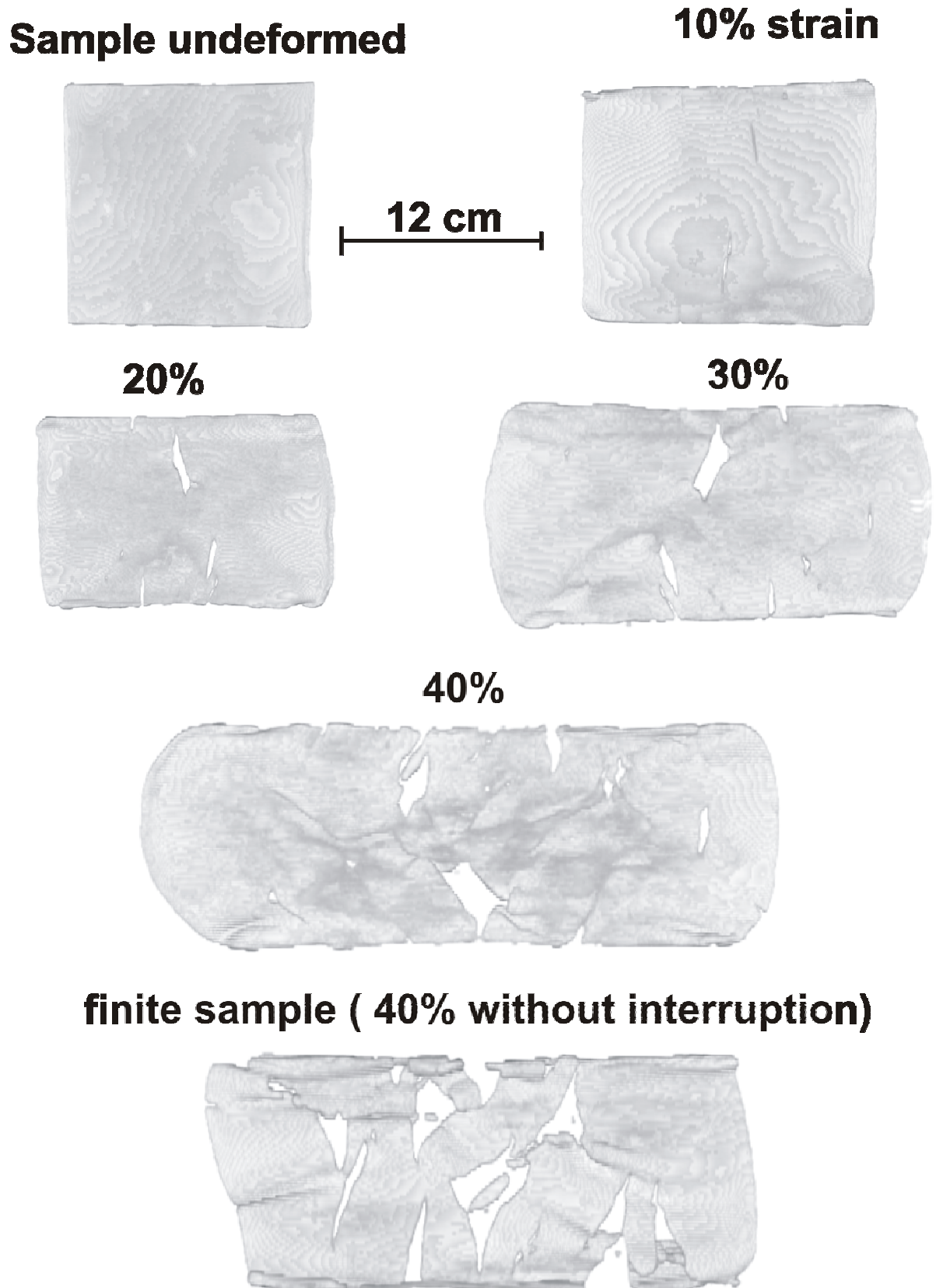
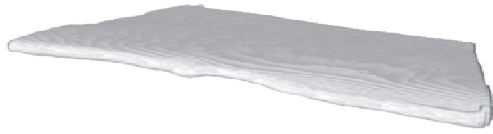


Fig. 4.19: Three-dimensional views of deformed competent layer of Kolb brown plasticine embedded in matrix of modified Beck's green plasticine at viscosity ratio $ca. = 19$ and strain rate $ca. = 4 \times 10^{-3} \text{ s}^{-1}$, based on computer tomography, showing the development of plane strain boudins. Only the stiff layer is shown. The undeformed sample is depicted on top, followed by 4 deformation stages, each of which implies 10% longitudinal strain.

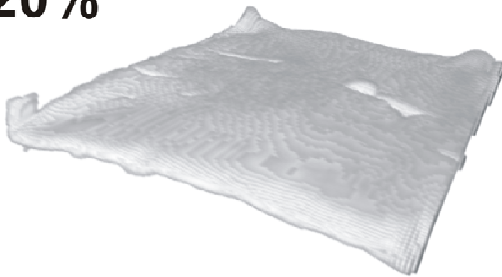
Sample undeformed



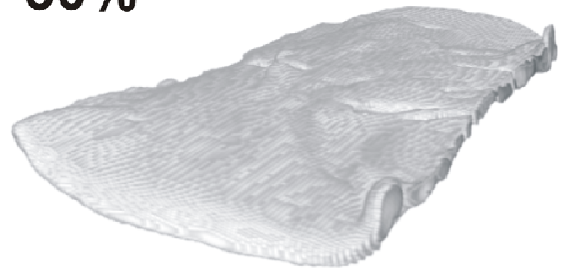
10% strain



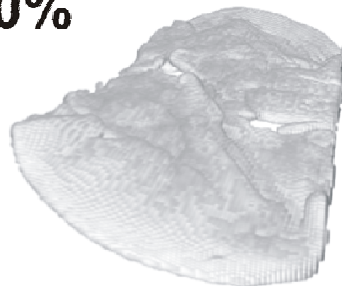
20%



30%



40%



12 cm

finite sample (40% without interruption)

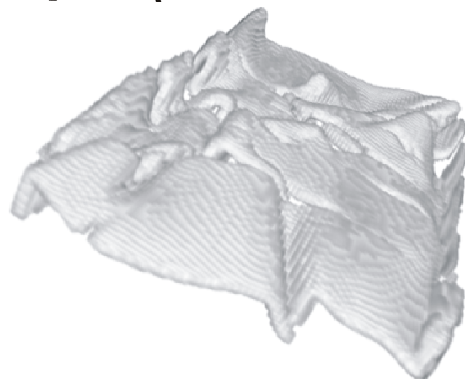


Fig. 4.20: Three-dimensional views of deformed competent layer of Kolb brown plasticine embedded in matrix of modified Beck's green plasticine at viscosity ratio $ca. = 19$ and strain rate $ca. = 4 \times 10^{-3} s^{-1}$, based on computer tomography, showing the development of plane strain folds. Only the stiff layer is shown. The undeformed sample is depicted on top, followed by 4 deformation stages, each of which implies 10% longitudinal strain. Viscosity ratio was $ca. 19$.

After having imposed the respective incremental strain, the sample was removed from the apparatus and analyzed using computer tomography (CT). Every experiment was carried out at a temperature, T , of 25°C and a strain rate, $\dot{\epsilon}$, of ca. $4 \times 10^{-3} \text{ s}^{-1}$ until a finite longitudinal strain of 40% was achieved.

When comparing the final deformation states of the two runs, a difference in deformation geometry of the stiff layer is obvious (Figs. 4.19 and 4.20). The structures are more mature in experiments in which deformation was continuous compared to those experiments that have been interrupted for screening and thus could multiply relax (Figs. 4.19 and 4.20). Boudins are present already at 10% strain (Figs. 4.19 and 4.20). Low-amplitude folds are hardly visible at 10% strain, but became more or less distinct if 20-30% strain is reached. With increasing strain, the length of the necks increases. There is clear evidence that additional new necks and boudins also develop during progressive strain. A strong interaction between folds and boudins at high strain magnitudes is indicated by the fact that the long axes of most of the necks and boudins are aligned oblique to the principal strain axes.

4.5 Coeval folding and boudinage under pure constriction with the X -axis parallel to the layer

During this study, the impact of layer thickness on the geometry of folds and boudins under pure constriction has been studied with the initially planar layer oriented parallel to the X -axis of the finite strain ellipsoid. The stiff layer and matrix consists of non-linear viscous *Kolb brown* and *Beck's green* plasticine, respectively. Apart from strain-hardening and strain rate effects, the viscosity of *Kolb brown* plasticine and *Beck's green* plasticine were held constant throughout the experiments. The rheological parameters have been determined by previous investigations (Zulauf and Zulauf, 2004; this study). Six runs have been carried out using thicknesses of the stiff layer of 1, 2, 4, 6, 8 and 10 ± 0.2 mm. All experimental runs were carried out at a temperature T of $30 \pm 2^\circ\text{C}$ and a strain rate, $\dot{\epsilon}$, of ca. $1.1 \times 10^{-4} \text{ s}^{-1}$ until a finite

longitudinal strain of 40% was achieved with a viscosity contrast m of 3.1. The apparent viscosity, η , and the stress exponent, n , for the layer at a strain rate $\dot{\epsilon} = \text{ca. } 10^{-3} \text{ s}^{-1}$ and a finite strain $e = 10\%$ are $2.23 \times 10^7 \text{ Pa s}$ and $n = 5.8$ and for the matrix $7.2 \times 10^6 \text{ Pa s}$ and 7.9.

The results of the experiments, documented in Table 4.8, are based on averaged data from measurements of 30 cross (YZ) and longitudinal ($XY=XZ$) sections. The spacing of the single cuts was set at 1–3 cm. There was no problem in reassembling the YZ -sections in order to investigate the $XY=XZ$ -sections.

$H_i[\text{mm}]$	$H_f[\text{mm}]$	$H_f[\%]$	n_{folds}	$W_{a(\text{fold})}[\text{mm}]$	$W_{d(\text{fold})}$	n_{boudins}	$W_{a(\text{boudin})}[\text{mm}]$	$W_{d(\text{boudin})}$
1	1.1 ± 0.4	10	-	-	-	21.0 ± 1.6	13.4 ± 7.7	12.2 ± 4.5
2	2.1 ± 0.4	5	-	-	-	9.0 ± 0.7	38.8 ± 18.2	18.5 ± 9.6
4	4.0 ± 0.4	0	-	-	-	6.8 ± 1.1	58.2 ± 36.8	14.6 ± 8.0
6	6.0 ± 0.8	0	-	-	-	5.5 ± 1.1	44.1 ± 23.2	7.4 ± 1.3
8	8.0 ± 0.9	0	-	-	-	4.8 ± 0.8	41.2 ± 20.2	5.2 ± 2.5
10	10.0 ± 1.0	0	1	-	-	4.0 ± 0.9	39.6 ± 18.9	4.0 ± 1.6

Table 4.8: Finite thickness of deformed competent layer and geometrical parameters of folds and boudins at different initial layer thicknesses; viscosity ratio = ca. 3 and strain rate = ca. $1.1 \times 10^{-4} \text{ s}^{-1}$. H_i = initial thickness of competent layer, H_f = finite average thickness of deformed competent layer, $(\frac{H_f}{H_i} - 1) * 100$ = layer thickening in [%], n_{folds} = number of folds, $W_{a(\text{fold})}$ = average fold arclength in YZ -sections, $W_{d(\text{fold})}$ = average fold arclength/thickness, n_{boudins} = number of boudins, $W_{a(\text{boudin})}$ = average boudin wavelength in XY -sections and $W_{d(\text{boudin})}$ = average boudin wavelength/thickness.

To investigate the geometry of the deformed competent layer, the specimen was cut in half along the X -axis. One of the halves served for analysing the geometry of the boudins ($XY=XZ$ -sections), the other half was used to examine the folds (YZ -sections) (Fig. 4.21). Analyses of these sections include determination of: (i) finite average thickness of deformed competent layer [H_f], (ii) number of folds [n_{folds}], (iii) number of boudins [n_{boudins}], (iv) average boudin wavelength [$W_{a(\text{boudin})}$].

The data show that there is no evidence for folding in the *YZ*-sections at the following thicknesses of the stiff layer: 1, 2, 4, 6 and 8 ± 0.2 mm (Table 4.8).

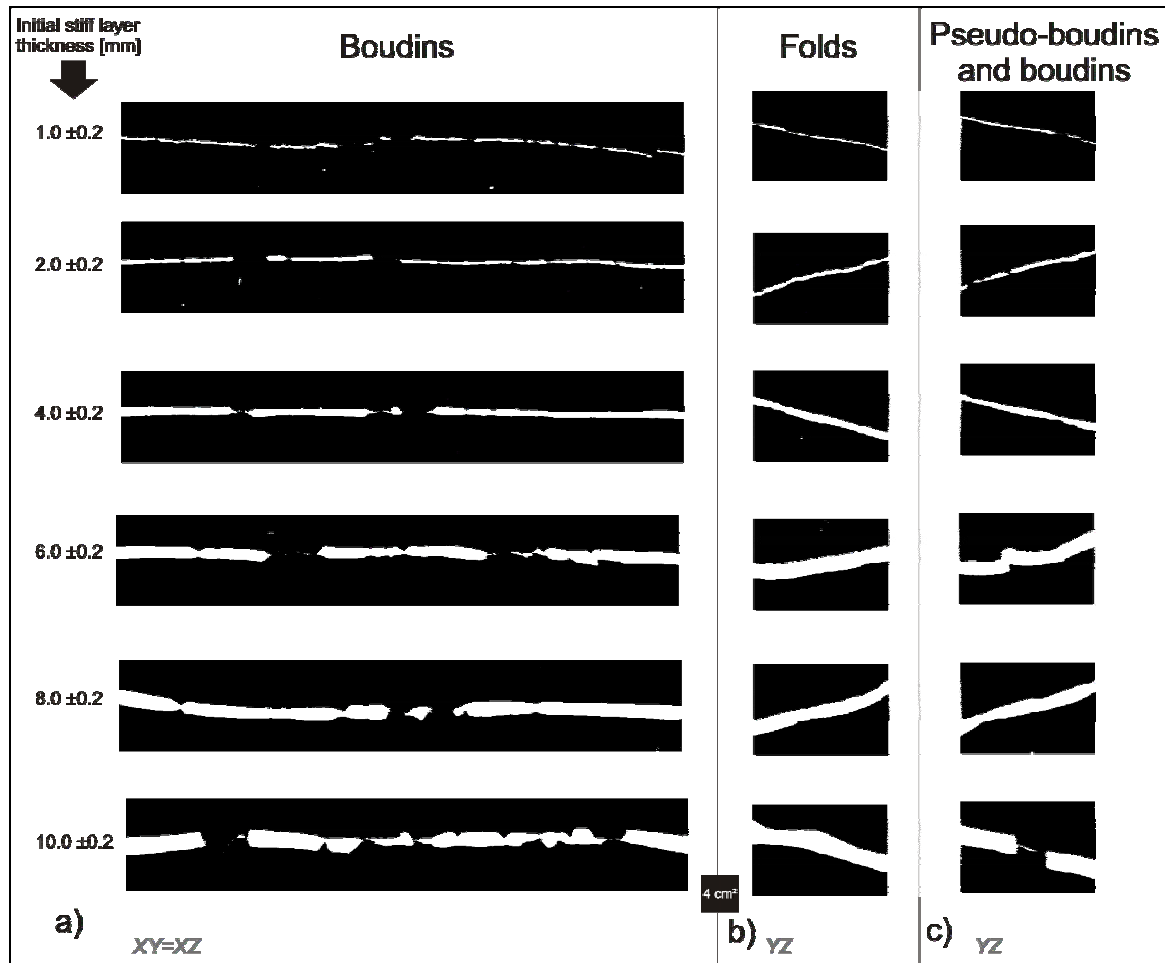


Fig. 4.21: *XY = XZ* and *YZ* section showing boudinage (a) and low amplitude fold and “pseudo-boudinage” or boudinage (b,c) of the stiff layer, respectively, under pure constrictional strain with the layer initially oriented parallel to the long axis of the finite strain ellipsoid; $e = 40\%$; strain rate = $1.1 \times 10^{-4} \text{ s}^{-1}$ and viscosity contrast was ca. 3.

In *YZ*-sections the layers are sometimes not continuous (Fig. 4.21c) which is attributed to the fact that some of the necks are trending oblique to the principal strain axes (“pseudo-boudinage”, Zulauf et al., 2003). In *XY=XZ*-sections the layer shows boudinage. Some of the boudins appear to have developed from pinch and swell structures (Fig. 4.21a). A striking feature of the experiments is the fact that, at a layer thickness of 10 ± 0.2 mm, boudins formed in *XY*-sections (Fig. 4.21a), whereas weak folding, characterized by large wavelengths, developed in *YZ*-sections (Fig. 4.21b). In this case, the *YZ*-sections show rather “boudinage”

(Fig. 4.21c) instead of “pseudo-boudinage” as has been described previously. This “boudinage” as it was the case with the “pseudo-boudinage” could result from the fact that some of the necks do not follow the YZ plane, but are slightly oblique with respect to the principal strain axes (Zulauf et al., 2003). There is a clear relation between the initial thickness of the stiff layer and geometric parameters, although the latter show a large uncertainty. With increasing layer thickness, the average number of boudins ($n_{boudins}$) decreases from ca. 21 to ca. 4 (Table 4.8; Fig. 4.22b).

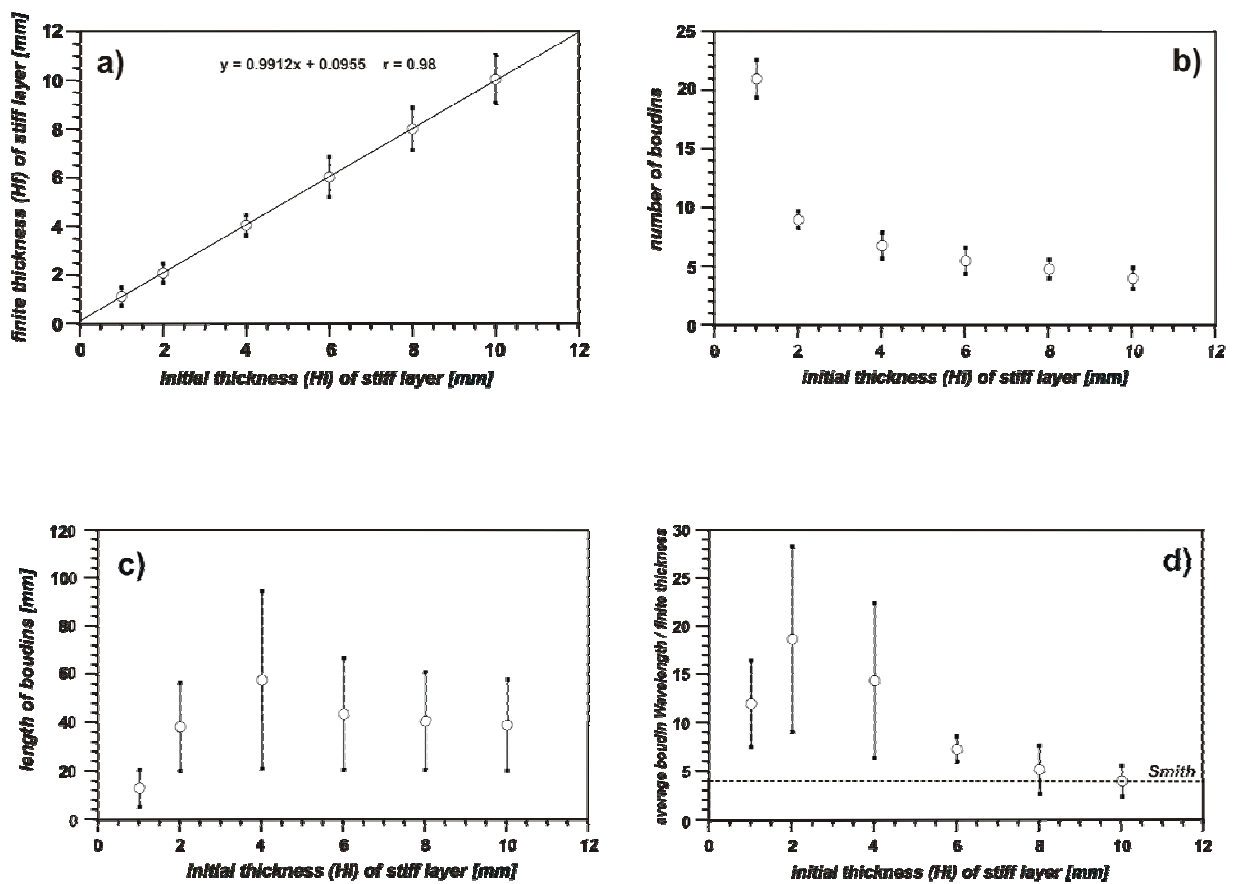


Fig. 4.22: Initial thickness of competent layer vs. finite thickness of competent layer (a), number of boudins (b), length of boudins (c) and wavelength of boudins (d). Functions and correlation coefficient, r , are represented at the top of each chart; horizontal dashed line is $L_d = 4.0$, calculated using equation [2-6].

The wavelength of boudins is the same within uncertainties (ca. 21 mm; Table 4.8; Fig. 4.22c). There is almost no change in thickness of the competent layer as is indicated by the H_f/H_i ratio that ranges from 1.0 to 1.1, equivalent to $\pm 10\%$ thickening (Fig. 4.22a). The wavelength/thickness ratio (W_d) ranges from ca. 4 to ca. 19 (Table 4.8; Fig. 4.22d).

5 DISCUSSION

5.1 Rheological data

In early scale models of tectonic deformation, it was assumed that rocks behave as Newtonian fluids (e.g. Ramberg, 1981) and for this reason Newtonian fluids were used as analogue materials. However, with recent improvements in the understanding of the rheology of natural rocks, it has been realized that lower crustal rocks behave other than Newtonian. In analogue modelling, the model must be rheologically similar to the prototype (e.g. Weijermars and Schmeling, 1986). Plasticine as a rock analogue is a non-Newtonian fluid (Schöpfer and Zulauf, 2002; Zulauf and Zulauf, 2004).

The rheological data indicate that all types of plasticine used in the present study are non-linear viscous materials characterized by strain-rate softening with a poorly defined yield transition from elastic to plastic behaviour at axial strains ranging from ca. 1 to ca. 3% (McClay, 1976, Zulauf and Zulauf, 2004). A common feature of all stress/strain curves is a strong increase in stress, followed by plastic yielding with moderate strain hardening (see Fig. 3.3b for terminology used in this section). The stress exponent is proportional to the distances between the stress/strain curves at different strain rates. The data obtained from the original material (Fig. 4.1a,e) show a wide range of stress/strain curves, indicating strong strain rate dependence of the stress. Adding oil to plasticine results in a significant change in the rheology of the original plasticine. An interpolation of viscosity and stress exponent of oil mixed plasticine is difficult because: (1) there is a non-linear relation between the apparent viscosity and the amount of added oil, and (2) the stress exponent changes unsystematically (Fig. 5.1).

The nonlinear rheology of plasticine is attributed to structural changes in the material, e.g. reorientation of the fillers. Addition of oil inhibits these structural changes (Schöpfer and Zulauf, 2002).

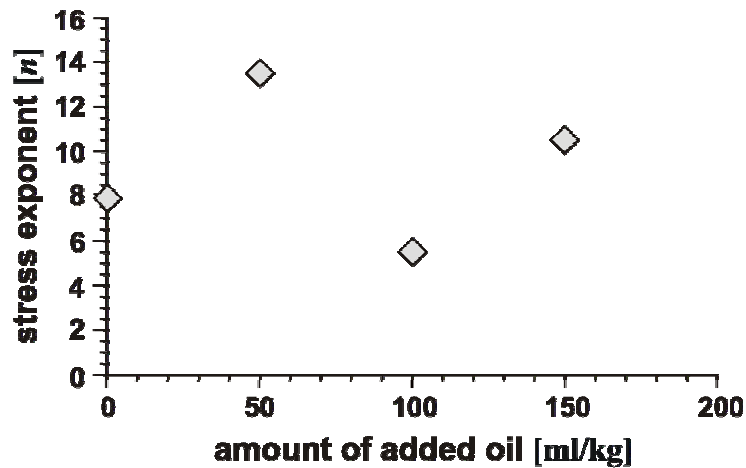


Fig. 5.1: Amount of added oil vs. stress exponent of the different runs used in the present study. Note that the plasticine used is the original Beck's green plasticine.

Table 4.1 summarises stress exponents and apparent viscosities for different types of plasticine used in the present study. It is important to note that the values given are only valid for the given strain rate, strain and temperature (axial strain e of 10%, a strain rate $\dot{\epsilon}$ of ca. 10^{-3} s^{-1} , and a temperature T of 25°C ; the uncertainty in temperature is $\pm 1^\circ\text{C}$). The stress exponents, n , and apparent viscosities, η , are ranging from 5.5 – 13.5 and 1.2×10^6 – 4.2×10^7 Pa s, respectively.

5.2 Coeval folding and boudinage under plane strain with the axis of no change perpendicular to the layer

Results of theoretical studies (cf. Ramberg, 1959, Fig. 7; Ramsay, 1967; Talbot and Sokoutis, 1995; Weijermars, 1997, Fig. 14-24) and analogue scale-model experiments (Kobberger and Zulauf, 1995; Zulauf et al., 2003; this study) suggest that folds and boudins may grow during one single deformation event. This holds for all types of coaxial deformation (from pure flattening via plane strain to pure constriction), if particular geometrical and rheological boundary conditions are given.

According to this study and Zulauf et al. (2003), plane-strain coaxial deformation seems to be suitable for producing coeval folding and boudinage in non-linear viscous material if the layer

is oriented perpendicular to the Y -axis of the finite strain ellipsoid. In this case, the thickness of the competent layer (H_i) increased significantly if the viscosity ratio ranges from ca. 20 to ca. 35. These observations are not or are only partly in line with results presented by Watkinson (1975) and Grujic and Mancktelow (1995). One reason for the differences in deformation geometry might be the fact that both authors used analogue materials, which differ significantly from plasticine. Moreover, Watkinson (1975) used clay multilayers, which developed folds in YZ -sections. He found that the thickness of the layers did not significantly change during deformation. The XY -sections, however, have not been monitored by him. Grujic and Mancktelow (1995) used wax as rock analogue which is characterized by a stress exponent ($n = 2 - 3$) that is much lower than the stress exponents used in the present studies ($n = 8 - 13$). The stress exponent of the competent layer, however, should have a large impact on the deformation geometry, and boudinage is hardly possible in Newtonian material (Smith 1977). Grujic and Mancktelow (1995) found that folding is only possible at viscosity ratios larger than ca. 30. They did not observe boudins. Our results, on the other hand, are compatible with results obtained by Zulauf et al. (2003), who deformed non-linear viscous *Beck's orange* plasticine + 100 ml oil kg^{-1} (matrix) and non-linear viscous *Kolb brown* plasticine + 50 ml oil kg^{-1} (layer) using the same apparatus and the same bulk deformation regime as has been used in the present study.

Apart from finite strain, that was held constant at 30% from run to run, both the viscosity ratio and the initial thickness of the competent layer are the parameters that largely control the deformation geometry. If the initial layer thickness is held constant, increasing viscosity ratio promotes the development of instabilities, such as folds and boudins. In this case, folding and incipient boudinage are only possible if the viscosity ratio is set at ca. 35. If the viscosity ratio is set at ca. 20, weak folding is visible in the YZ -section, whereas the XY -section is almost free from boudinage. This observation suggests that under the present plane-strain conditions, folding is a stronger instability than boudinage, meaning that in this particular case of plane

strain, theoretical amplification rates due to the instability are larger for folding than for boudinage (cf. Smith, 1975). If the viscosity contrast is decreased, it is expected that folding can still be observed while boudinage is still too weak to develop significant structures. If the viscosity ratio is \leq ca. 7, layer and matrix deform almost homogeneously and neither a fold nor a boudin will grow.

Viscous layer thickening is an unexpected, but characteristic phenomenon of the deformation structures, which did not occur in other cases of simultaneous folding and boudinage, such as pure constriction (Kobberger and Zulauf, 1995; Zulauf and Zulauf, 2005). Thus, constraining the degree of layer thickening using common techniques of strain analysis can be used to identify the present structures in natural tectonites. Layer thickening, however, is difficult to explain. It should be intimately related to the difference in strain rate of layer and matrix and the growth of instabilities. If the viscosity ratio between layer and matrix is low, i.e. <10 , the strain rate of both materials is approximately the same, meaning that layer and matrix will show a similar shortening strain rate along Z and an extensional strain rate along X . Thus, the deformation of layer and matrix is almost homogeneous and the shortening of the layer along Z is balanced by extension along X . As we are dealing with bulk plane-strain, where the strain rate along Y is 0, the above considerations explain why the thickness of the layer should not significantly change at low viscosity ratios. If the viscosity ratio increases to values $\gg 10$, the strain rate of the matrix will be strikingly higher than the strain rate of the layer, resulting in the growth of instabilities and layer thickening. Layer thickening is only possible if the viscous shortening strain rate of the layer along Z ($\dot{\epsilon}_Z(\text{layer})$) is larger than the viscous extensional strain rate of the layer along X ($\dot{\epsilon}_X(\text{layer})$). As we do not know at which stage of progressive deformation the layer thickening occurs, the question why both strain rates are different cannot be answered at the present stage. Incremental deformation studies and quantitative geometrical analyses using computer tomography are necessary to shed more light on this question.

This difference in longitudinal strain rate of matrix and layer along X causes drag forces along the matrix/layer interface, which is one prerequisite for the development of fracture boudins (Ramberg, 1955). If the layer is thick enough, these drag forces will not be able to cause tensional forces within the layer, which exceed the tensional strength of the layer. Thus, the layer will not be inhomogeneously deformed; boudins do not occur. If, on the other hand, the layer is thin, its tensional strength is much lower, and boudinage is possible.

Measurements of natural folds give low wavelength to thickness ratios, usually <10 and commonly in the range 4 – 6 (Sherwin and Chapple, 1968). This implies a correspondingly low effective viscosity ratio between layer and matrix (<50) and non-linear material behaviour to achieve the amplification of the observed folds (Smith, 1979). Similar values of W_d should also be expected applying equation [2-6] (Fletcher, 1974; Smith, 1977, 1979), developed for plane-strain deformation of power-law materials if the competent layer is oriented perpendicular to the X -axis of the finite strain ellipsoid.

From the rheological parameters of the plasticine used, L_d is calculated at 8.4. This value is similar to the values calculated for $W_{d(fold)}$ and $W_{d(boudin)}$, although there is a large uncertainty for the latter (Fig. 5.2).

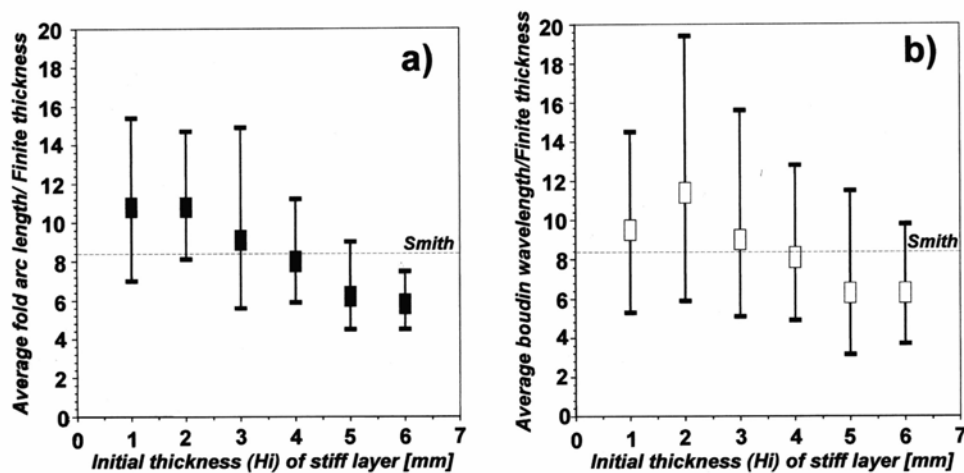


Fig.5.2: Initial thickness of stiff layer of Beck's black plasticine vs. average fold arc length/finite thickness (a), and initial thickness of stiff layer vs. average boudin wavelength/finite thickness (b); viscosity ratio = ca. 35; horizontal dashed line is $L_d = 8.4$, calculated using equation [2-6].

Thus, the equation of Smith (1977, 1979), probably also holds for folds and coeval boudins that result from plane-strain coaxial deformation with the layer oriented perpendicular to the Y -axis of the finite strain ellipsoid, although significant layer thickening did occur. The similar values of W_d and L_d can be interpreted that the viscous elongation of the layer along the X -direction did not significantly affect the initial wavelength of the instabilities.

The overall decrease in wavelength/thickness ratio with layer thickness (Fig. 5.2) is difficult to explain. One reason might be the fact that initial layer irregularity is different for the different layer thicknesses.

The principal difference in fold shape depends on both the viscosity contrast and the thickness of the competent layer. Many authors have investigated the influence of material rheology on the geometry of amplifying folds. Folds with the same kind of geometry as presented in our study have also been described in layered viscous materials (Johnson and Fletcher, 1994), and in strain-softening materials (Neurath and Smith, 1982; Tentler, 2001). This confirms that the principal difference in fold shape is not only dependent on the viscosity contrast and the thickness of the layer. There are other, rheological and geometrical, constraints that could account for sharp hinges etc., such as pseudo-plastic behaviour (Johnson, 1970), strain-softening behaviour (Neurath and Smith, 1982), an increase in the layer's power-law exponent or material anisotropy (Lan and Hudleston, 1996), or variations in the degree of initial layer irregularity.

The new results should be important for all workers who are focusing on the relation between rock rheology and geometry of natural instabilities. There are different geodynamic settings in which the X -axis of the finite strain ellipsoid is parallel to the fold axis. Examples where deformation structures might result from bulk plane-strain with the Y -axis perpendicular to the layer are: (1) folding during crustal extension in rocks of the Austroalpine nappes in eastern Switzerland (Froitzheim, 1992); (2) folding in eclogite facies rocks of the Ile de Groix (Shelley and Bossière, 1999); (3) folding and boudinage of rocks of the Phyllite-Quartzite unit

of Crete during subduction (Zulauf et al., 2002). In order to verify the present assumption that these structures do really result from bulk plane-strain with the Y -axis perpendicular to the competent layer, the amount of layer thickening should be constrained using common techniques of strain analysis.

5.3 The impact of strain rate on folding and boudinage under plane strain

The results of the second set of experiments suggest a considerable influence of the strain rate on the geometry of the deformed stiff layer including its thickness. Apart from the strain rate, the deformation geometry of the stiff layer is controlled by the orientation of the stiff layer with respect to the principal strain axes. The impact of the orientation of the stiff layer is most striking when regarding the apparent finite thickness of the deformed layer. In the case of pure boudinage ($S \perp Z$), layer thickening is less significant and largely *increases* with strain rate. In cases of pure folding ($S \perp X$), the degree of layer thickening is much higher and largely *decreases* with strain rate. If folds and boudins are growing together ($S \perp Y$), the degree in layer thickening *increases* with strain rate. In the latter cases, however, the degree of thickening varies significantly more than in the other two cases. The different intensity of layer thickening at different orientations of the layer is compatible with literature data (e.g. Zulauf et al., 2003). The change in layer thickening with strain rate, however, is more difficult to explain. As we are dealing with strain-rate softening plasticine, the strain rate should have an impact on the viscosity of layer and matrix and thus on the viscosity contrast between both. There is an almost linear increase in the viscosity ratio with log strain rate. Within the range of strain rates used, the viscosity contrast varies from 3.3 to 10.2 (Table 5.1; Fig. 5.3). In the case of pure folding ($S \perp X$) this relation between strain rate and viscosity contrast explains

the decrease in layer thickening with strain rate and viscosity contrast, respectively. The difference in slope in the log strain rate vs. thickening plot above and below $\dot{\epsilon} = 1.1 \times 10^{-3} \text{ s}^{-1}$ is difficult to explain.

Strain rate [s ⁻¹]	$\eta_1(\text{matrix})$ [Pa s]	$\eta_2(\text{layer})$ [Pa s]	m	$n_1(\text{matrix})$	$n_2(\text{layer})$	L_d
7.9×10^{-6}	3.02×10^8	1.01×10^9	3.3	10.5	6.5	4.1
1.4×10^{-5}	1.70×10^8	7.02×10^8	4.1	10.5	6.5	4.4
2.7×10^{-4}	8.92×10^6	4.23×10^7	4.7	10.5	6.5	4.6
1.1×10^{-3}	1.21×10^6	8.54×10^6	7.1	10.5	6.5	5.3
1.1×10^{-2}	1.10×10^5	1.04×10^6	9.5	10.5	6.5	5.8
1.7×10^{-2}	7.20×10^5	7.06×10^4	10.2	10.5	6.5	6.0

Table 5.1: Rheological data of Beck's green plasticine with 150 ml oil kg⁻¹ (matrix) and original Kolb grey plasticine (stiff layer) at different strain rates $\dot{\epsilon}$, 10% strain and temperature of $T = 24 \pm 1^\circ\text{C}$. η_1 = matrix viscosity; η_2 = layer viscosity; m = viscosity contrast (η_2/η_1); L_d = theoretical wavelength/thickness ratio calculated after Smith (1977).

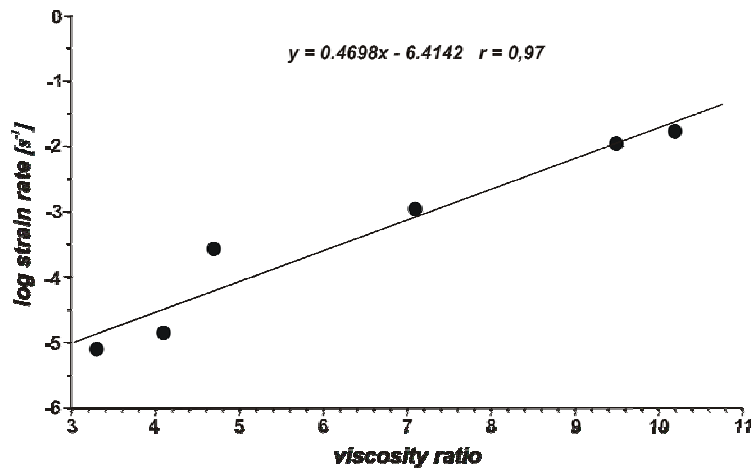


Fig. 5.3: Viscosity ratio between layer and matrix vs. log strain rate of the different runs. Functions and correlation coefficient, r , are represented at the top of the chart. Note that the plasticine used is the same in all cases.

Increasing viscosity contrast with strain rate also explains the increase in fold arc length and the decrease in the number of folds at slow strain rates ($\dot{\epsilon} < 1.1 \times 10^{-3} \text{ s}^{-1}$). This trend in

change of layer geometry is compatible with results of analytical solutions, although the absolute values of the normalized arc length (W_d) are significantly higher than those calculated after the Smith equation (Fig. 4.11).

Substituting the measured values of the stress exponents and the strain-rate dependent effective viscosities of the original *Kolb grey* plasticine (stiff layer) and the modified *Beck's green* plasticine (matrix) into equation [2-6], the dominant wavelength/thickness, L_d , is found to be range from 4.1 to 5.3 (Table 4.7; Figs. 4.11, 4.14 and 4.18).

The decrease in arc length with strain rate and viscosity contrast, respectively, at $\dot{\epsilon} > 10^{-3} \text{ s}^{-1}$ is difficult to explain. However, although the strain-rate dependent change in arc length is not compatible with the gradient suggested by the Smith equation, the absolute values of W_d are approximating the values of L_d at the highest strain rate used. This observation is in line with the fact that the analytical solutions should not hold for low viscosity contrasts. Previous results of analogue modelling with higher viscosity ratios between layer and matrix (*ca.* $7 \leq m \leq \text{ca. } 35$), on the other hand, are compatible with the Smith equation (this study). It has further to be emphasized that the values of W_d might be somewhat higher than those presented if the real finite thickness instead of the apparent finite thickness is used for the normalization procedure.

The situation is still more complicated if the layer is oriented perpendicular to the Z -axis (pure boudinage). Both the length and the number of boudins are opposite compared to the pure folds. However, similar to the case of pure folding, the change from a negative (positive) to a positive (negative) slope in the diagram log strain rate vs. length of boudins (number of boudins) does also occur at $\dot{\epsilon} = 1.1 \times 10^{-3} \text{ s}^{-1}$, pointing to a change in the growth of the instabilities if this strain rate is reached. At slow strain rates and corresponding low viscosity contrast the difference between W_d and L_d is considerably large. At higher strain rates, the W_d values are more close to the L_d values (Fig. 4.14) confirming the assumption that results of

analytical solutions do not hold for low viscosity ratios between matrix and layer (Smith, 1977, 1979).

A particular problem concerns the layer thickening in cases of pure boudinage. This thickening cannot be explained only by the drag effect related to the cutting of the sample. Increasing layer thickening at increasing strain rate and viscosity contrast respectively remains an open question.

If the layer is oriented perpendicular to the Y -axis (coeval folding and boudinage), the impact of the strain rate on layer thickening is more important than in the other two cases of pure folding and pure boudinage. At the slowest strain rate, which corresponds to $m = 3.3$, layer thickening is almost absent. This behaviour can be explained by the fact that the bulk strain perpendicular to the layer, and thus parallel to the Y -axis, is zero. As matrix and layer show similar flow behaviour because of the low viscosity contrast, the deformation is almost homogeneous and thickening of the layer is not possible (this study). This assumption is supported by the lack of instabilities at the lowest strain rate used. If the strain rate increases, layer thickening increases almost linearly with log strain rate, and instabilities (folds and boudins) are growing. This behaviour can be explained by elevated viscosity contrast between layer and matrix at higher strain rates. Enlarged viscosity contrast supports inhomogeneous deformation and growth of instabilities. Obviously, the latter are intimately related to layer thickening.

Peculiar is the fact that in cases where $S \perp Y$, the number of instabilities decreases significantly with increasing strain rate and that no instability grows at the highest strain rate used. This behaviour cannot be explained by the impact of the strain rate on the viscosity contrast. The latter is 10 at the highest strain rate. On the other hand, previous studies have shown that coeval folding and boudinage should be possible at a viscosity contrast of ca. 10, whereas at $m \leq ca. 7$, layer and matrix deform almost homogeneously and neither a fold nor a boudin will grow (this study).

The growth of classical folds ($S \perp X$) or boudins ($S \perp Z$) is possible already at low strain rates which imply low viscosity ratios. However, apart from the exception mentioned above, the growth of coeval folds and boudins ($S \perp Y$) requires much higher strain rates which are related to higher viscosity ratios. The fact that the growth of instabilities with $S \perp Y$ requires higher viscosity ratios is in line with results presented by Zulauf et al. (2003) who used not only plasticine as analogue material but also the same apparatus and the same bulk deformation regime as has been used in the present study.

5.4 Coeval folding and boudinage under pure constriction with the X -axis parallel to the layer

There is no evidence for folding in YZ -sections if the thickness of the stiff layer is ≤ 8 mm, although the layer shows boudinage in $XY=XZ$ -sections. At a layer thickness of 10 mm, boudins formed in XY -sections, and weak folding, characterized by large wavelengths, developed in YZ -sections. In order to produce constrictional folds and boudins, Kobberger and Zulauf (1995), Zulauf et al. (2003), and Zulauf and Zulauf (2005) have used similar boundary conditions like those of the present study. There is almost no change in the thickness of the competent layer and, given that $m < \text{ca. } 10$, constrictional folding is hardly possible, whereas constrictional boudins may develop (Zulauf and Zulauf, 2005). The constrictional runs of the present thesis have obtained similar results. Thus, under pure constriction boudins are stronger instabilities than folds. The opposite behaviour has been found under plane strain with the layer-oriented perpendicular to the Y -axis (see above). As boudins affect the orientation of the fold axes and vice versa (Fig. 4.21c), pure constriction and plane strain, with S perpendicular to Y , result in complex but characteristic patterns of coeval folds and boudins (Zulauf et al., 2003).

Theories of buckle folding in non-linear materials suggest the initial wavelength of buckle folds and boudins to be the same. The geometrical and rheological parameters of these instabilities are determined by equation [2-6] (Fletcher, 1974; Smith, 1977, 1979).

To compare the theoretical value (L_d) with the average boudin wavelength ($W_{a(\text{boudin})}$), measured in the experiments, we normalized the initial wavelength of the structures determined by equation [2-9].

From the rheological parameters of the plasticine used, L_d is calculated at 4.0. This value clearly exceeds the W_d -value if the thickness of the stiff layer is 1, 2, 4 and 6 mm. L_d on the other hand is similar to the W_d -values calculated for the thickness of 8 and 10 mm, the latter showing relatively large uncertainties (Fig. 4.22d). Thus, the equation of Smith (1977, 1979), probably also holds approximately for folds and coeval boudins that result from pure constriction with the layer oriented perpendicular to the $Y=Z$ -axis of the finite strain ellipsoid in cases where the viscosity ratio between layer and matrix is low (i.e. ca. 3) and the layer thickness is large.

6 CONCLUSIONS AND OPEN QUESTIONS

In the present study (and in numerous others) it has been shown that small scaled modelling can improve our knowledge about the formation of geological structures. Proper modelling needs a detailed investigation of the properties of the analogue materials. According to the new results of experimental runs obtained using a new machine that supports every type of coaxial strain, the following conclusions can be drawn:

1. The macroscopic behaviour of plasticine is quite similar as in strain hardening rocks regardless of the different microscopic aspects of deformation. Therefore, if one is aware that the stress exponent and viscosity increase with increasing strain, the three original materials (*Beck's black*, *Kolb grey* and *Beck's green*) with stress exponents ranging from 6.5 to 8 are adequate for modelling geological structures (folds, boudins) in mechanically stratified material under plane-strain conditions. The two plasticine/oil mixtures (Bg50 and Bg150) are suitable as incompetent matrix material, where (as in this study) unrealistic high stress exponents can be neglected and only the apparent viscosity needs to be considered.

2. Rheology tests on original *Beck's black*, *Kolb grey* and *Beck's green* plasticine and plasticine/oil mixtures (Bg50, Bg100 and Bg150) have shown that this material has a nonlinear rheology. Both stress exponent and viscosity increase with increasing strain. The material exhibit strain-hardening and steady-state flow is never reached. These special properties of plasticine make strict scaling difficult, but with some limitations, it can be used as analogue material for rocks deforming by dislocation creep with weak strain hardening.

3. Coeval folding and boudinage of a competent layer are possible under plane strain if (a) the weak matrix and the competent layer consist of non-linear viscous material with n -values $\gg 1$, (b) the competent layer is oriented perpendicular to the Y -axis of the finite strain ellipsoid, and (c) the viscosity contrast between layer and matrix is larger than ca. 20.

4. Folding and boudinage under plane strain are associated with a significant increase in the thickness of the competent layer. The latter phenomenon does not occur in other cases of simultaneous folding and boudinage, such as bulk pure constriction. The layer thickening is an unexpected phenomenon that cannot be entirely explained at the present stage. Incremental deformation experiments and geometrical analyses of the instabilities using computer tomography are required to shed more light on this phenomenon.

5. Our experiments suggest that substituting the measured values of the stress exponents and the effective viscosities of the original *Beck's black* plasticine ($\eta_1 = 4.2 \times 10^7$ Pa s and $n_1 = 8.0$) and the modified *Beck's green* plasticine (Bg150; $\eta_2 = 1.2 \times 10^6$ Pa s and $n_2 = 10.5$) into the theoretical dominant wavelength equation predicted by Smith (1977), the dominant wavelength/thickness, L_d , is found to be 8.4. There is a clear tendency that this value is similar to the values calculated for $W_{d(fold)}$ and $W_{d(boudin)}$, although there is a large uncertainty for the latter. Thus, the equation of Smith (1977, 1979), probably also holds when folds and boudins develop simultaneously ($S \perp Y$) and when boudins develop independently ($S \perp Z$), but can obviously not be applied at very low viscosity ratios as is indicated by the low-strain-rate experiments.

6. The deformation geometry of the stiff layer is strongly controlled by the strain rate and the type of overall three-dimensional coaxial strain. There is a clear relation between viscosity ratio and strain rate.

7. The growth of classical folds ($S \perp X$) or boudins ($S \perp Z$) is possible already at low viscosity ratios. However, the growth of coeval folds and boudins ($S \perp Y$) requires much higher viscosity ratios.

8. Folds and boudins develop simultaneously under pure constrictional strain, given that the analogue material shows non-linear viscous behaviour, and viscosity ratio between layer and matrix are set at 10 or even higher (Zulauf and Zulauf, 2005).

9. Because of the complex deformation patterns, the study of high-strain constrictional and plane strain structures is hardly possible using conventional cuttings along XZ or YZ planes. CT-images are necessary to quantify the geometry of deformed layers in 3D and 4D.

10. The new results are important for the interpretation of natural tectonites, particularly in those cases where fold-axes are subparallel to the stretching direction (Fig. 6.1).

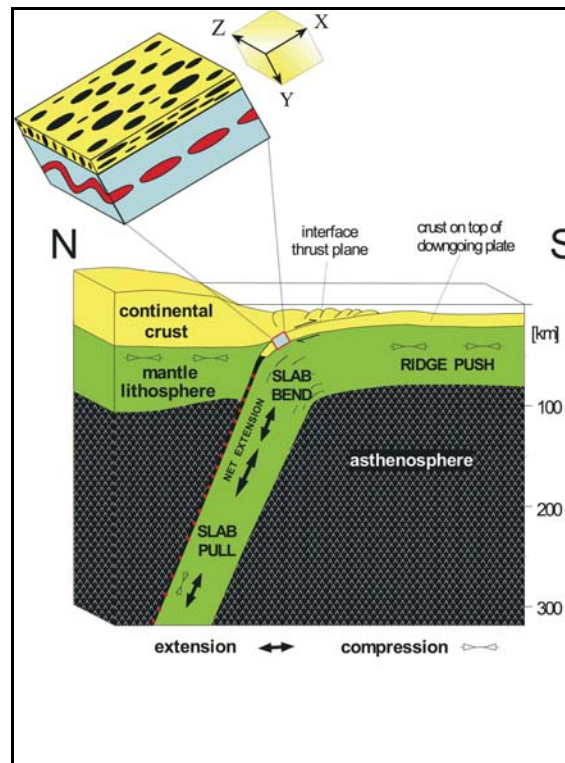


Fig. 6.1: Model explaining coeval folding and boudinage under bulk plane-strain coaxial conditions in subduction environment (modified after Zulauf et al., 2002).

Several open questions will be answered by further experiments. They concern not only the influence of layer thickness, but also the impact of varying stress exponent, and orientation of the layer. Further studies will also focus on three dimensional pure constriction deformation of a competent plasticine layer embedded in a competent plasticine matrix to improve our understanding about the evolution of folds and boudins if the layer is oriented parallel to the X -axis of the finite strain ellipsoid.

One significant open question concerns layer thickening in cases of boudinage with $S \perp Z$?

7 REFERENCES

- Abbassi, M.R. and Mancktelow, N.S. **1990**: The effect of initial perturbation shape and symmetry on fold development. *Journal of Structural Geology* 12, 273 – 282.
- Abbassi, M.R. and Mancktelow, N.S. **1992**: Single layer buckle folding in non-linear materials –I. Experimental study of fold development from an isolated initial perturbation. *Journal of Structural Geology* 13, 85 – 104.
- Anthony, M. and Wickham, J. **1978**: Finite-element simulation of asymmetric folding. *Tectonophysics* 47, 1 – 14.
- Ashby, M.F. and Verral, R.A. **1977**: Micromechanisms of flow and fracture and their relevance to the rheology of the upper mantle. *Phil. Trans. R. Soc.* 288A, 59 – 95.
- Barnhoorn, A., Burlini, L., Bystricky, M. and Kunze, K. **2000**: Rheology and microstructure of Carrara marble experimentally deformed to high strains: 8. Symposium "Tektonik, Struktur- und Kristallingeologie", Freiburg, Terra Nostra, Schriften der Alfred-Wegener-Stiftung:, p. 68.
- Bazant, Z.P. and Cedolin, L. **1991**: *Stability of structures: Elastic, Inelastic, Fracture, and Damage Theories*. Oxford University Press, New York.
- Biot, M.A. **1961**: Theory of folding of stratified viscoelastic media and its implications in tectonics and orogenesis. *Geological Society of America Bulletin* 72, 1595 – 1620.
- Biot, M.A., Odé, H. and Roever, W.L. **1961**: Experimental verification of the theory of folding of stratified viscoelastic media. *Geological Society of America Bulletin* 72, 1621 – 1632.
- Blumenfeld, P. **1983**: Le “tuilage des megacristaux”, un critère d’écoulement rotationnel pour les fluidalites des roches magmatiques ; Application au granite de Barbey. *Bulletin de la Société Géologique de France* 25, 309 – 318.

- Boespflug, X., Ross, N., Long, B. and Dumais, J.F. **1994**: Tomodensitométrie axiale: relation entre l'intensité tomographique et la densité de la matière. *Can. J. Earth Sci.* 31, 426 – 434.
- Boespflug, X., Long, B. and Occhietti, S. **1995**: CAT-scan in marine stratigraphy: a quantitative approach. *Mar. Geol.* 122, 281 – 301.
- Bonse, U. and Busch, F. **1999**: X-ray computed microtomography (μ CT) using synchrotron radiation (SR). *Progress in Biophysics and molecular Biology* 65 (1/2), 133 – 169.
- Bremaecker, J.C.d. and Becker, E.B. **1978**: Finite element models of folding. *Tectonophysics* 50, 349 – 367.
- Chapple, W.M. **1968**: A mathematical theory of finite-amplitude rock-folding. *Geological Society of America Bulletin* 79, 47 – 68.
- Cloos, E. **1947**: Boudinage. *Transactions of the American Geophysical Union* 28, 626 – 632.
- Cobbold, P.R., Cosgrove, J.W. and Summers, J.M. **1971**: Development of internal structures in deformed anisotropic rocks. *Tectonophysics* 12, 23 – 53.
- Cobbold, P.R. **1975**: Fold propagation in single embedded layers. *Tectonophysics* 27, 333 – 351.
- Cobbold, P.R. **1976**: Fold shapes as functions of progressive strain. *Phil. Trans. R. Soc. London A283*, 129 – 138.
- Cobbold, P.R. **1977**: Finite-element analysis of fold propagation: a problematic application? *Tectonophysics* 38, 339 – 358.
- Cobbold, P.R. and Quinquis, H. **1980**: Development of sheath folds in shear regimes. *Journal of Structural Geology* 2, 119 – 126.
- Cobbold, P.R. and Jackson, M.P.A. **1992**: Gum rosin (colophony); a suitable material for thermomechanical modelling of the lithosphere. *Tectonophysics* 210, 255 – 271.
- Coe, K. **1959**: Boudinage structure in west Cork, Ireland. *Geological Magazine* 96-3, 191 – 200.

-
- Crémer, J.F. Long, B., Locat, J., Desrosiers, G. and de Montety, L. **2002**: Application de la Scanographie à l'étude de la densité des sédiments et à la caractérisation des structures sédimentaires : exemple des sédiments déposés dans la rivière Saguenay (Québec, Canada) après la crue de Juillet 1996. *Can. Geotech. Journal* 39, 440 – 450.
- Cruikshank, K.M. and Johnson, A.M. **1993**: High-amplitude folding of linear-viscous multilayers. *Journal of Structural Geology* 15(1), 79 – 94.
- Davy, P. and Cobbold, P.R. **1991**: Experiments on shortening of a 4-layer model of the continental lithosphere. *Tectonophysics* 188, 1 – 25.
- Den Hartog, J.P. **1949**: *Strength of materials*. Dover Publications, New York.
- DePaor, D.G., Simpson, C., Bailey, C.M., McCaffrey, K.J.W., Bean, E., Gower, R.J.W., and Aziz, G. **1991**: The role of solution in the formation of boudinage and transverse veins in carbonate rocks at Rheems, Pennsylvania. *Geological Society of America Bulletin* 103, 1552 – 1563.
- Dieterich, J.H. **1969**: Origin of cleavage in folded rocks. *American Journal of Science* 267, 155 – 165.
- Dieterich, J.H. and Carter, N.L. **1969**: Stress history of folding. *American Journal of Science* 267, 129 – 154.
- Dieterich, J.H. **1970**: Computer experiments on mechanics of finite amplitude folds. *Canadian Journal of Earth Sciences* 7, 467 – 476.
- Dubey, A.K. **1980**: Late stages in the development of folds as deduced from model experiments. *Tectonophysics* 65, 311 – 322.
- Dubey, A.K. **1997**: Simultaneous development of non cylindrical folds, frontal ramps, and transfer faults in a compressional regime: Experimental investigations of Himalayan Examples. *Tectonics* 16, 336 – 346.
- Dubey, A.K. and Cobbold, P.R. **1977**: Non cylindrical flexural slip folds in nature and experiment. *Tectonophysics* 38, 223 – 239.

- Duliu, O.G. **1999**: Computer axial tomography in geosciences: an overview. *Earth Sci. Rev.* 48, 265 – 281.
- Etchecopar, A. **1974**: Simulation par ordinateur de la deformation progressive d'un aggregate polycrystalline. Étude du développement de structures orientées par écrasement et cisaillement. Unpublished Ph.D. thesis, University of Nantes, France.
- Etchecopar, A. **1977**: A plane kinematic model of progressive deformation in a polycrystalline aggregate. *Tectonophysics* 39, 121 – 139.
- Euler, L. **1744**: *Methodus Inveniendi Lineas Curvas Maximi Minimive proprietate gaudentes.* Marcum-Michaelem Bousquet & Socios., Lausanne & Geneve.
- Fletcher, R.C. **1974**: Wavelength selection in the folding of a single layer with power law rheology. *American Journal of Science* 274, 1029 – 1043.
- Fletcher, R.C. **1977**: Folding of a single viscous layer: exact infinitesimal-amplitude solution. *Tectonophysics* 39, 593 – 606.
- Fletcher, R.C. and Sherwin, J. **1978**: Arc lengths of single layer folds: a discussion of the comparison between theory and observation. *American Journal of Science* 278, 1085 – 1098.
- Fletcher, R.C. **1991**: Three-dimensional folding of an embedded viscous layer in pure shear. *Journal of Structural Geology* 13, 87 – 96.
- Franssen, R.C.M.W. and Spiers, C.J. **1990**: Deformation of polycrystalline salt in compression and in shear at 250 – 350 °C. In: Knipe, R.J. and Rutter, E.H. (Eds), *Deformation Mechanisms, Rheology and Tectonics.* Geological Society, London, Special Publication no. 54, 201 – 213.
- Froitzheim, N. **1992**: Formation of recumbent folds during synorogenic crustal extension (Austroalpine nappes, Switzerland). *Geology* 20, 923 – 926.
- Gaudemer, Y. and Tapponier, P. **1987**: Ductile and brittle deformations in the northern Snake Range, Nevada. *Journal of Structural Geology* 9, 159 – 180.

-
- Gerbault, M., Burov, E.B., Poliakov, A.N.B. and Daignieres, M. **1999**: Do faults trigger folding of the lithosphere? *Geo. Res. Lett* 26 (2), 271 – 274.
- Ghosh, S.K. **1966**: Experimental tests of buckling folds in relation to strain ellipsoid in simple shear deformation. *Tectonophysics* 3, 169 – 185.
- Ghosh, S.K. **1968**: Experiments on buckling of multilayers which permit interlayer gliding. *Tectonophysics* 6, 207 – 249.
- Ghosh, S.K. **1974**: Strain distribution in superposed buckling folds and the problem of reorientation of early lineation. *Tectonophysics* 21, 249 – 272.
- Ghosh, S.K., Mandal, N., Khan, D. and Deb, S.K. **1992**: Models of superposed buckling in single layers controlled by initial tightness of early folds. *Journal of Structural Geology* 14, 381 – 394.
- Ghosh, S.K. and Ramberg, H. **1968**: Buckling experiments on intersecting folds patterns. *Tectonophysics* 5, 89 – 105.
- Gleason, G.C. and Tullis, J. **1995**: A flow law for dislocation creep in quartz aggregates determined with molten salt cell. *Tectonophysics* 247, 1 – 23.
- Goldstein, A.G. **1988**: Factors affecting the kinematic interpretation of asymmetric boudinage in shear zones. *Journal of Structural Geology* 10, 707 – 716.
- Goscombe, B., Passchier, C.W. and Hand, M. **2004**: Boudinage classification: end-member boudin types and modified boudin structures. *Journal of Structural Geology* 26, 739 – 763.
- Green, A.P. **1951**: The use of plasticine models to simulate the plastic flow of metals. *Philosophical Magazine* 7(42), 365 – 373.
- Griggs, D.T., Turner, F.J. and Heard, H.C. **1960**: Deformation of rocks at 500 to 800°C: *Memoir of the Geological Society of America* 79, 39 – 104.
- Grujic, D. and Mancktelow, N.S. **1995**: Folds with axes parallel to the extension direction: an experimental study. *Journal of Structural Geology* 17, 279 – 291.

- Hall, Sir J. **1815**: On the vertical position and convolutions of certain strata, and their relation with granite. Transactions of the Royal Society Edinburgh 7, 79 – 108.
- Hanmer, S.K. **1984**: The potential use of planar and elliptical structures as indicators of strain regime and kinematics of tectonic flow. Current Research, Part B, Geological Survey of Canada 84-1B, 133 – 142.
- Hanmer, S.K. **1986**: Asymmetrical pull-aparts and foliation fish as kinematic indicators. Journal of Structural Geology 8, 111 – 122.
- Hanmer, S.K. and Passchier, C.W. **1991**: Shear-Sense Indicators: A Review. Geological Survey of Canada 90-17, 72p.
- Harker, A. **1889**: On the local thickening of dykes and beds by folding. Geological Magazine, New Series 6, 69 – 70.
- Heard, H.C. and Carter, N.L. **1968**: Experimentally induced “natural” intergranular flow in quartz and quartzite. American Journal of Science 266, 1 – 42.
- Heard, H.C. and Raleigh, C.B. **1972**: Steady-state flow in marble at 500 °C to 800 °C. Geological Society of America Bulletin 83, 935 – 956.
- Hobbs, B.E., Means, W.D. and Williams, P.F. **1976**: An outline of structural geology. John Wiley & Sons, Inc., New York. 571p.
- Horsfield, W. **1977**: An experimental approach to basement-controlled faulting, Geologie en Mijnbouw 56, 363 – 370.
- Hounsfield, G.N. **1973**: Computerized transverse axial (tomography): Part 1. Description of system. Br. J. Radiol. 46, 1016 – 1022.
- Hubbert, M.K. **1937**: Theory of scale models as applied to the study of geologic structures. Geological Society of America Bulletin 48, 1459 – 1520.
- Hubbert, M.K. **1951**: Mechanical basis for certain familiar geologic structures. Geological Society of America Bulletin 62, 355 – 372.

- Hudleston, P.J. **1973**: An analysis of "single layer" folds developed experimentally in viscous media. *Tectonophysics* 16, 189 – 214.
- Hudleston, P.J. and Stephansson, O. **1974**: Layer shortening and fold-shape development in the buckling of single layers. *Tectonophysics* 17, 299 – 321.
- Hudleston, P.J. **1986**: Extracting information from folds in rocks. *J. Geol. Education* 34, 237 – 245.
- Hudleston, P.J. and Lan, L. **1993**: Information from fold shapes. *Journal of Structural Geology* 15, 253 – 264.
- Hudleston, P.J. and Lan, L. **1994**: Rheological controls on the shapes of single-layer folds. *Journal of Structural Geology* 16, 1007 – 1021.
- Johnson, A.M. **1970**: *Physical processes in geology*: San Francisco, Freeman, Cooper and Company, 1 – 577.
- Johnson, A.M. and Fletcher, R.C. **1994**: *Mechanical analysis and interpretation of structures in deformed rock*: New York, Columbia University Press, 1 – 461.
- Jongmans, D. and Cosgrove, H.W. **1993**: Observations structurales dans la région de Bastogne. *Ann. Soc. Geol. Belg.* 116, 129 – 136.
- Kaisersberger, K. **2002**: *Visualisierung und Analyse geologischer Volumendaten*. Unveröffentlichte Studienarbeit, Universität Erlangen – Nürnberg. 59 Seiten.
- Kantzas, A., Marentette, D. and Jha, K.N. **1992**: Computer-assisted tomography: from a quantitative visualization to quantitative core analysis. *J. Pet. Technol.* 31(9), 48 – 56.
- Kenter, J. A.M. **1989**: Applications of computerized tomography in sedimentology. *Mar. Geotechnol.* 8, 201 – 211.
- Ketcham, R.A and Carlson, W.D. **2001**: Acquisition, optimization and interpretation of X-ray computed tomographic imagery: Applications to the geosciences. *Computer and Geosciences* 27, 381 – 400.
- Kirby, S.M. **1983**: Rheology of the lithosphere. *Rev. Geophys. Space Phys.* 21, 1458 – 1487.

- Kobberger, G. and Zulauf, G. **1995**: Experimental folding and boudinage under pure constrictional conditions. *Journal of Structural Geology* 17, 1055 – 1063.
- Kohlstedt, D.L., Evans, B. and Mackwell, S.J. **1995**: Strength of the lithosphere: Constraints imposed by laboratory experiments. *Journal of Geophysical Research* 100, 587 – 602.
- Lacassin, R. **1988**: Large-scale foliation boudinage in gneisses. *Journal of Structural Geology* 10, 643 – 647.
- Lan, L. and Hudleston, P. **1995b**: A method of estimating the stress exponent in the flow law for rocks using fold shape. *Pageoph* 145 (3/4), 621 – 635.
- Lan, L. and Hudleston, P. **1996**: Rock rheology and sharpness of folds in single layers. *Journal of Structural Geology* 18, 925 – 931.
- Lan, L. and Wang, R. **1987**: Finite-element analysis of an overturned fold using a viscous-fluid model. *Tectonophysics* 139, 309 – 314.
- Landau, L.D. and Lifshitz, E.M. **1970**: *Theory of Elasticity*. Oxford, Pergamon press.
- Lewis, R.W. and Williams, J.R. **1978**: A finite-element study of fold propagation in a viscous layer. *Tectonophysics* 44, 263 – 283.
- Lloyd, G.E. and Ferguson, C.C. **1981**: Boudinage structure: some new interpretations based on elastic-plastic finite element simulations. *Journal of Structural Geology* 3, 117 – 128.
- Lloyd, G.E., Ferguson, C.C. and Reading, K. **1982**: A stress-transfer model for the development of extension fracture boudinage. *Journal of Structural Geology* 4, 355 – 372.
- Lohest, M. **1909**: De l'origine des veines et des geodes des terrains primaires de Belgique. Troisième note: *Annales de la Société Géologique de Belgique* 36, 275 – 282.
- Long, B.F. and Ross, N. **1991**: *Etudes océanographiques physiques et biologiques: analyses complémentaires*. Rapp. INRS-Oceanol., Project SEBJ 1LP-892-1-02, 73.

- Malavielle, J. **1987**: Kinematics of compressional and extensional ductile shearing deformation in a metamorphic core complex of the northeastern Basin and Range. *Journal of Structural Geology* 9, 541 – 554.
- Malavielle, J. and Lacassin, R. **1988**: „Bone-shaped“ boudins in progressive shearing. *Journal of Structural Geology* 10, 335 – 345.
- Mancktelow, N.S. **1988**: The rheology of paraffin wax and its usefulness as an analogue for rocks. *Bull. Geol. Instn. Univ. Uppsala* 14, 181 – 193.
- Mancktelow, N.S. and Abbassi, M.R. **1992**: Single layer buckle folding in non-linear materials – II. Comparison between theory and experiment. *Journal of Structural Geology* 13, 105 – 120.
- Mancktelow, N.S. **1999a**: Finite-element modelling of single-layer folding in elasto-viscous materials: the effect of initial perturbation geometry. *Journal of Structural Geology* 21, 161 – 177.
- Mandal, N. and Karmakar, S. **1989**: Boudinage in homogeneous foliated rocks. *Tectonophysics* 170, 151 – 158.
- Mandal, N. and Khan, D. **1991**: Rotation, offset and separation of oblique-fracture (rhombic) boudins: theory and experiments under layer-normal compression. *Journal of Structural Geology* 13, 349 – 356.
- Mandal, N., Khan, D. and Deb, S.K. **1992**: An experimental approach to wide-necked pinch-and-swell structures. *Journal of Structural Geology* 14, 395 – 403.
- Mandal, N., Chakraborty, C. and Samanta, S.K. **2000**: Boudinage in multilayered rocks under layer-normal compression: a theoretical analysis. *Journal of Structural Geology* 22, 373 – 382.
- Marcoux, J., Brun, J.-P. and Ricou, L.E. **1987**: Shear structures in anhydrite at the base of thrust sheets (Antalya, southern Turkey). *Journal of Structural Geology* 9, 555 – 561.

- Marques, F.G. and Cobbold, P.R. **1995**: Development of highly non-cylindrical folds around rigid ellipsoidal inclusions in bulk simple shear regimes: natural examples and experimental modelling. *Journal of Structural Geology* 17, 589 – 602.
- Manz, R. and Wickham, J. **1978**: Experimental analysis of folding in simple shear. *Tectonophysics* 44, 79 – 90.
- McClay, K.R. **1976**: The rheology of plasticine. *Tectonophysics* 33, T7 – T15.
- Michaud, E., Desrosiers, G., Long, B., de Montety, L., Crémer, J.F., Pelletier, E., Locat, J., Gilbert, F. and Stora, G. **2003**: Use of axial tomography to follow temporal changes of benthic communities in an unstable sedimentary environment (Baie des Ha! Ha!, Saguenay Fjord. *Journal of Experimental Marine Biology and ecology* 285 – 286, 265 – 282.
- Molen, V.d. **1985**: Interlayer material transport during layer-normal shortening; Part I, The model. *Tectonophysics* 115, 275 – 295.
- Molen, V.d. **1985**: Interlayer material transport during layer-normal shortening; Part II, Boudinage, pinch-and-swell and migmatites at Soendre Stroemfjord airport, West Greenland. *Tectonophysics* 115, 297 – 313.
- Neurath, C. and Smith, R.B. **1982**: The effect of material properties on growth-rates of folding and boudinage: experiments with wax models. *Journal of Structural Geology* 4, 215 – 229.
- Orsi, T.H., Edwards, C.M. and Anderson, A.L. **1994**: X-ray computed tomography – a non destructive method for quantitative analysis of sedimentary cores. *J. Sediment. Res., A* 64, 690 – 693.
- Parrish, D.K. **1973**: A non-linear finite element fold model. *American Journal of Science* 273, 318 – 334.
- Passchier, C.W. and Druguet, E. **2002**: Numerical modelling of asymmetric boudinage. *Journal of Structural Geology* 24, 1789 – 1804.

-
- Paterson, M.S. **1987**: Problems in the extrapolation of laboratory rheological data. *Tectonophysics* 133, 33 – 43.
- Peltzer, G., Gillet, P. and Tapponnier, P. **1984**: Formation des failles dans un matériau modèle: la plasticine. *Bulletin de la Société Géologique de France* 26, 161 – 168.
- Pfiffner, O.A. and Ramsay, J.G. **1982**: Constraints on geological strain rates: arguments from finite strain states of naturally deformed rocks. *Journal of Geophysical Research* 87, 311 – 321.
- Platt, J.P. and Vissers, R.L. **1980**: Extensional structures in anisotropic rocks. *Journal of Structural Geology* 2, 397 – 410.
- Price, N.J. and Cosgrove, J.W. **1990**: *Analysis of Geological Structures*. Cambridge University Press, 1 – 502.
- Quirke, T.T. **1932**: Boudinage, an unusual structural phenomenon. *Geological Society of America Bulletin* 34, 649 – 660.
- Ramberg, H. **1955**: Natural and experimental boudinage and pinch-and-swell structures. *Journal of Structural Geology* 63, 512 – 526.
- Ramberg, H. **1959**: Evolution of ptygmatic folding. *Norsk Geologisk Tidsskrift* 39, 99 – 152.
- Ramberg, H. **1961**: Contact strain and folding instability of a multilayered body under compression. *Geol. Rdsch* 51, 405 – 439.
- Ramberg, H. **1963**: Fluid dynamics of viscous buckling applicable to folding of layered rocks. *Bull. Am. Ass. Petr. Geol* 47(3), 484 – 505.
- Ramberg, H. **1959**: Evolution of ptygmatic folding. *Norsk Geologisk Tidsskrift* 39, 99 – 152.
- Ramberg, H. **1967**: *Gravity, Deformation and the Earth's Crust, as Studied by Centrifuged Models*. Academic Press, London. 214p.
- Ramberg, H. **1981**: *Gravity, Deformation and the Earth's Crust*, 2nd ed. Academic Press, London.
- Ramsay, J.G. **1866**: The geology of North Wales. *Mem. Geol. Surv. Gt. Britain* 111, 1 – 381.

- Ramsay, J.G. **1967**: Folding and fracturing of rocks. New York, McGraw-Hill Book Co.
- Ramsay, J.G. and Huber, M.I. **1987**: The techniques of modern structural geology, Volume 2: Folds and fractures: London, Academic Press, 1 – 700.
- Ranalli, G. and Murphy, D.C. **1987**: Rheological stratification of the lithosphere. *Tectonophysics* 132, 281 – 295.
- Ranalli, G. **1995**: Rheology of the Earth, Chapman & Hall, London, 1 – 413.
- Rezk – Salama, C. **2002**: Volume Rendering Techniques for General Purpose Graphics Hardware. In: *Arbeitsberichte des Institutes für Informatik 35*. Friedrich-Alexander-Universität Erlangen-Nürnberg, Technische Fakultät, Institut für Informatik, Erlangen, 201 Seiten.
- Richard, P. **1991**: Experiments on faulting in a two-layered cover sequence overlying a reactivated basement fault with oblique-slip. *Journal of Structural Geology* 13, 459 – 469.
- Rivers, M.L., Sutton, S.R. and Eng, P. **1999**: Geoscience applications of X-ray computed microtomography. In: Bonse, U. (Ed.), *Developments in X-ray Tomography 2*. SPIE, Bellingham, 78 – 86.
- Schellart, W.P. **2002**: Analogue modelling of large-scale tectonic processes. *Journal of the Virtual Explorer* 7, 1 – 6.
- Schmalholz, S.M. **2000**: Finite amplitude folding of viscoelastic rocks: importance of elasticity for slow tectonic motion. PhD thesis, Geologischen Institut, Zürich, Dissertation Naturwissenschaften ETH Zürich, Nr. 13576, 167 Seiten.
- Schmid, S.M., Boland, J.N. and Paterson, M.S. **1977**: Superplastic flow in fine-grained limestone. *Tectonophysics* 43, 257 – 291.
- Schmid, S.M., Paterson, M.S. and Boland, J.N. **1980**: High temperature flow and dynamic recrystallization in Carrara marble. *Tectonophysics* 65, 245 – 280.

-
- Schöpfer, M.P.J. **2000**: Experimentelle Untersuchung zur Bildung von Falten und Boudins. Unpublished diploma thesis, Friedrich-Alexander-Universität Erlangen-Nürnberg.
- Schöpfer, M.P.J. and Zulauf, G. **2002**: Strain-dependent rheology and the memory of plasticine. *Tectonophysics* 354, 85 – 99.
- Selkman, S. **1978**: Stress and displacement analysis of boudinage by the finite-element method. *Tectonophysics* 44, 115 – 139.
- Shelley, D. and Bossière, G. **1999**: Ile de Groix: retrogression and structural development in an extensional regime. *Journal of Structural Geology* 21, 1441 – 1455.
- Shemenda, A.I. **1983**: Similarity criteria in mechanical modelling of tectonic processes. *Soviet Geology and Geophysics* 24, 8 – 16.
- Sherwin, J.A. and Chapple, W.M. **1968**: Wavelength of single layer folds: a comparison between theory and observation. *American Journal of Science* 266, 167 – 179.
- Simpson, C. and Schmid, S.M. **1983**: An evaluation of criteria to deduce the sense of movement in sheared rocks. *Geological Society of America Bulletin* 94, 1281 – 1288.
- Smith, R.B. **1975**: Unified theory of the onset of folding, boudinage and mullion structure. *Geological Society of America Bulletin* 86, 1601 – 1609.
- Smith, R.B. **1977**: Formation of folds, boudinage and mullions in non-Newtonian materials. *Geological Society of America Bulletin* 88, 312 – 320.
- Smith, R.B. **1979**: The folding of a strongly non-Newtonian layer. *American Journal of Science* 279, 272 – 287.
- Smoluchowski, M. **1909a**: Über ein gewisses Stabilitätsproblem der Elastizitätslehre und dessen Beziehung zur Entstehung von Faltengebirgen. *Anzeiger der Akademie der Wissenschaften in Krakau, mathematisch-naturwissenschaftliche Klasse* 2, 3 – 20.
- Smoluchowski, M. **1909b**: Versuche über Faltungerscheinungen schwimmender elastischer Platten. *Anzeiger der Akademie der Wissenschaften in Krakau, mathematisch-naturwissenschaftliche Klasse* 2, 727 – 734.

- Sofuoglu, H. and Rasty, J. **2000**: Flow behaviour of Plasticine used in physical modelling of metal forming processes. *Tribology International* 33, 523 – 529.
- Sokoutis, D. **1987**: Finite strain effects in experimental mullions. *Journal of Structural Geology* 9, 233 – 242.
- Stephansson, O. and Berner, H. **1971**: The finite-element method in tectonic processes. *Physics of the Earth and Planetary Interiors* 4, 301 – 321.
- Stephansson, O. **1974**: Stress-induced diffusion during folding. *Tectonophysics* 22, 233 – 251.
- Strömgaard, K.E. **1973**: Stress distribution during deformation of boudinage and pressure shadows. *Tectonophysics* 16, 215 – 248.
- Swanson, M.T. **1992**: Late Acadian – Alleghenian transpressional deformation: evidence from asymmetric boudinage in the Casco Bay area, coastal Maine. *Journal of Structural Geology* 14, 323 – 341.
- Swanson, M.T. **1999**: Kinematic indicators for regional dextral shear along the Norumbega fault system in the Casco Bay area, coastal Maine. *Geological Society of America Special Paper* 331, 1 – 23.
- Talbot, C.J. and Sokoutis, D. **1995**: Strain ellipsoids from incompetent dykes: application to volume loss during mylonitization in the Singö gneiss zone, central Sweden. *Journal of Structural Geology* 17, 927 – 948.
- Talbot, C.J. **1999**: Can field data constrain rock viscosity? *Journal of Structural Geology* 21, 949 – 957.
- Tentler, T. **2001**: Experimental study of single layer folding in nonlinear materials, in *Tectonic Modeling: A volume in Honor of Hans Ramberg*, edited by Koyi HA, Mancktelow NS, 89 – 100.
- Timoshenko, S.P. and Woinowsky-Krieger, S. **1959**: *Theory of plates and shells*. McGraw-Hill Book Company, Auckland.

- Tokhtuev, G.V. **1967**: Boudinage structures and their role in the localisation of ore mineralization (with examples from the Ukrainian Shield and other regions): Kiev, Naukova-Dumka, 1 – 215 (Uncovered in 1985 in the newly compiled USGS electronic database, provided encouraging independent support for boudinage- controlled mineralization).
- Treagus, S.H. and Lan, L. **2000**: Pure shear deformation of square objects, and applications to geological strain analysis. *Journal of Structural Geology* 22, 105 – 122.
- Twiss, R.J. and Moores, E.M. **1992**: *Structural Geology*: New York, W.H. Freeman and Company, 1 – 532.
- Watkinson, A.J. **1975**: Multilayer folds initiated in bulk plane strain, with the axis of no change perpendicular to the layering. *Tectonophysics* 28, T7 – T11.
- Weijermars, R. **1986**: Flow behaviour and physical chemistry of bouncing putties and related polymers in view of tectonic laboratory applications. *Tectonophysics* 124, 325 – 358.
- Weijermars, R. **1997**: *Principles of Rock Mechanics*. Alboran Science Publishing. 359p.
- Weijermars, R. and Schmeling, H. **1986**: Scaling of Newtonian and non-Newtonian fluid dynamics without inertia for quantitative modelling of rock flow due to gravity (including the concept of rheological similarity). *Physics of the Earth and Planetary Interiors* 43, 316 – 330.
- Wellington, S.L. and Vinegar, H.J. **1987**: X-ray computerized tomography. *J. Pet. Technol.*, August, 885 – 898.
- Whitten, E.H.T. **1966**: *Structural geology of folded rocks*. Chicago, Ill: Rand McNally, NY, 1 – 678.
- Williams, J.R., Lewis, R.W. and Zienkiewicz, O.C. **1978**: A finite-element analysis of the role of initial perturbations in the folding of a single viscous layer. *Tectonophysics* 45, 187 – 200.

- Williams, J.R. **1980**: Similar and chevron folds in multilayers using finite element and geometric models. *Tectonophysics* 65, 323 – 338.
- Willis, B. **1891 – 1892**: The mechanics of Appalachian Structure: United States Geological Survey, 13th Annual Report, Part. 2, 211 – 289.
- Wilson, G. **1961**: The tectonic significance of small-scale structures and their importance to the geologist in the field. *Annales de la Société Géologique de Belgique* 84, 424 – 548.
- Woldekidan, T. **1982**: Deformation of multilayers compressed normal to the layering. Unpublished Ph.D thesis, University of London.
- Zhang, Y., Hobbs, B.E and Ord, A. **1996**: Computer simulation of single-layer buckling. *Journal of Structural Geology* 18(5), 643 – 655.
- Zuber, M.T and Parmentier, E.M. **1996**: Finite amplitude folding of a continuously viscosity-stratified lithosphere. *Journal of Geophysical Research* 101(B3), 5489 – 5498.
- Zulauf, G., Kowalczyk, G., Krahl, J., Petschick, R. and Schwanz, S. **2002**: The tectonometamorphic evolution of high-pressure low temperature metamorphic rocks of eastern Crete, Greece: constraints from microfabrics, strain, illite crystallinity and paleodifferential stress. *Journal of Structural Geology* 24, 1805 – 1828.
- Zulauf, G., Zulauf, J., Hastreiter, P. and Tomandl, B. **2003**: A deformation apparatus for three-dimensional deformation and its application to rheologically stratified analogue material. *Journal of Structural Geology* 25, 469 – 480.
- Zulauf, J. and Zulauf, G. **2004**: Rheology of plasticine used as rock analogue: The impact of temperature, composition and strain. *Journal of Structural Geology* 26, 725 – 737.
- Zulauf, J. **2004**: Analogmodellierung von Falten und Boudins in Raum und Zeit. PhD thesis, Friedrich-Alexander-Universität Erlangen-Nürnberg, Institut für Geologie und Mineralogie, Erlangen, *Erlanger Geologische Abhandlungen* 135, 115p.
- Zulauf, J. and Zulauf, G. **2005**: Coeval folding and boudinage in four dimensions. *Journal of Structural Geology* 27, 1061 – 1068.

LIST OF ABBREVIATIONS

Symbol	Definition	Dimension
A	Amplitude of folded layer	[mm]
C	Temperature-and strain-dependent constant (material constant)	[MPa ⁻ⁿ s ⁻¹]
e	Longitudinal strain of the main axes (e_x, e_y, e_z)	-
\dot{e}	Finite longitudinal strain rate	[s ⁻¹]
\dot{E}	Incremental longitudinal strain rate	[s ⁻¹]
E^*	Activation energy	[kJ mol ⁻¹]
ε_{ij}	Deviatoric strain tensor	-
F	Force	[N]
G	Shear modulus	[m s ⁻²]
H_i	Initial thickness of competent layer	[mm]
H_f	Finite average thickness of deformed competent layer	[mm]
H_b	Average boudin thickness of deformed competent layer	[mm]
$\Delta H = \left(\frac{H_f}{H_i} - 1\right) * 100$	Layer thickening	[%]
η_1	Apparent dynamic viscosity of matrix	[Pa.s]
η_2	Apparent dynamic viscosity of layer	[Pa.s]
l	Finite length	[mm]
L	Initial length	[mm]
L_d	Theoretical wavelength / thickness ratio calculated after Smith (1977) (λ / H)	-
λ	Wavelength of folded layer	[mm]
m	Viscosity contrast (η_2 / η_1)	-

n	<i>Stress exponent</i>	-
n_1	<i>Stress exponent of matrix</i>	-
n_2	<i>Stress exponent of layer</i>	-
N	<i>Number of data</i>	-
n_{folds}	<i>Number of folds</i>	-
$n_{boudins}$	<i>Number of boudins</i>	-
R	<i>Universal gas constant</i>	$[8.314 \text{ J mol}^{-1} \text{ K}^{-1}]$
R_k	<i>Regression coefficient</i>	-
S	<i>Surface</i>	$[\text{m}^2]$
t	<i>Time</i>	$[\text{s}]$
T	<i>Temperature</i>	$[^\circ\text{C}]$
T_k	<i>Temperature in Kelvin ($^\circ\text{C} + 273$)</i>	$[\text{K}]$
τ	<i>Shear stress</i>	$[\text{MPa}]$
σ	<i>Differential stress ($\sigma_1 - \sigma_3$)</i>	$[\text{MPa}]$
σ_1	<i>Main principal stress</i>	$[\text{MPa}]$
σ_2	<i>Medial principal stress</i>	$[\text{MPa}]$
σ_3	<i>Least principal stress</i>	$[\text{MPa}]$
$Wa(\text{boudin})$	<i>Average boudin wavelength in XY-sections</i>	$[\text{mm}]$
$Wa(\text{fold})$	<i>Average fold arclength in YZ-sections</i>	$[\text{mm}]$
$Wd(\text{boudin})$	<i>Average boudin wavelength / thickness measured on deformed samples</i>	-
$Wd(\text{fold})$	<i>Average fold arclength / thickness measured on deformed samples</i>	-
X	<i>Long axis of the finite strain ellipsoid</i>	-
Y	<i>Intermediate axis of the finite strain ellipsoid</i>	-
Z	<i>Short axis of the finite strain ellipsoid</i>	-

CURRICULUM VITAE

Name: **ENAMA MENGONG**
First Name: **Mathurin**
Date of birth: 07 June 1973
Place of birth: Yaoundé (Cameroon)
Nationality: Cameroonian
Family status: Single
Religion: Catholic
Current position: Research PhD Candidate
Languages: Fluently English, French, and good knowledge in German
Emails addresses : M.Enama-Mengong@em.uni-frankfurt.de ; mathurin_e@yahoo.com

EDUCATION

Since 11/2004: Postgraduate studies continue at the Institute of Geology and Paleontology; ***Johann Wolfgang University Frankfurt am Main***; Germany (Structural geology and Analogue modelling) Ph.D. Title: Folding and boudinage under constriction and plane strain: Results from analogue modelling.

2001 – 11/2004: Postgraduate studies at the Institute of Geology and Mineralogy; ***University of Erlangen-Nürnberg***; Germany (Structural geology and Analogue modelling) Ph.D. Title: Folding and boudinage under constriction and plane strain: Results from analogue modelling.

1999 – 1998: Study of Earth Sciences at Faculty of Science. University of Yaoundé I (Cameroon) with final examination as D.E.A (***First Year Doctorate***) of Earth Sciences, Option: Surface Processes, Speciality: Applied Geology–Metallogeny.

1998 – 1993: Study of Earth Sciences at Faculty of Science. University of Yaoundé I (Cameroon) with final examination as Master of Earth Sciences, Option: Internal Processes, Speciality: Petrology–Geochemistry and Structural Geology.

1993 – 1985: High School in Mbalmayo (Cameroon) and School-leaving examination.

1985 – June 1979: Basic School and Modern Secondary School in Dschang (Cameroon).

GRANTS

01.10.04 – 31.12.04: DAAD grant, Johann Wolfgang University Frankfurt am Main, Institute of Geology and Paleontology, Frankfurt am Main. (**Germany**).

01.04.04 – 30.09.04: DAAD grant, University of Erlangen-Nürnberg, Institute of Geology and Mineralogy, Erlangen. (**Germany**).

01.04.03 – 31.03.04: DAAD grant, University of Erlangen-Nürnberg, Institute of Geology and Mineralogy, Erlangen. (**Germany**).

01.04.02 – 31.03.03: DAAD grant, University of Erlangen-Nürnberg, Institute of Geology and Mineralogy, Erlangen (**Germany**).

01.04.01 – 31.03.02: DAAD grant, University of Erlangen-Nürnberg, Institute of Geology and Mineralogy, Erlangen (**Germany**).

MEMBERSHIPS

Geologische Vereinigung (**GV; Germany**); Geological Society of America (**GSA; USA**).

EMPLOYMENT

Since 11/2004: PhD Research Candidate, *Johann Wolfgang University Frankfurt am Main*, Institute of Geology and Paleontology (**Germany**).

2001 – 11/2004: PhD Research Candidate, *University of Erlangen-Nürnberg*, Institute of Geology and Mineralogy (**Germany**).

2000 – 1999: Post Graduate Teaching Assistantship in Cartography practical to 1st and 2nd Years Natural Science Students, Department of Earth Sciences, Faculty of Science, University of Yaoundé I (**Cameroon**).

1999 – 1998: Post Graduate Teaching Assistantship in Cartography practical to 1st and 2nd Years Natural Science Students, Department of Earth Sciences, Faculty of Science, University of Yaoundé I (**Cameroon**).

1998 – 1997: Post Graduate Teaching Assistantship in Cartography practical to 1st and 2nd Years Natural Science Students, Department of Earth Sciences, Faculty of Science, University of Yaoundé I (**Cameroon**).

1997 – 1996: Post Graduate Teaching Assistantship in Cartography practical to 1st Years Natural Science Students, Department of Earth Sciences, Faculty of Science, University of Yaoundé I (**Cameroon**).

DISSERTATION COMPLETED

Enama Mengong, M. “Study of Industrial Clays in the area of Yaoundé, Cameroon”. Rapp. Bibliographique D.E.A Univ. Yaoundé I, Fac. Sci., Dépt. Sci. Terre, 36p. – D.E.A (First Year Doctorate), **June 1999**.

Enama Mengong, M. “Contribution to the Pétro-structural study and the cartography of the metamorphites in the north of Yaoundé, Cameroon”. Mém. Maîtrise, Univ. Yaoundé I, Fac. Sci., Dépt. Sci. Terre, 95p. – M.Sc, (First Year Doctorate), **September, 1998**.

RESEARCH/PRESENTATIONS

Enama Mengong, M. and Zulauf, G., **2006**. Coeval folding and boudinage under pure constriction with the *X*-axis parallel to the layer. – Journal of Structural Geology (in preparation).

Enama Mengong, M. and Zulauf, G., **2006**. Coeval folding and boudinage under plane strain through space and time. – Tectonophysics (in preparation).

Enama Mengong, M. and Zulauf, G., **2006**: The impact of strain rate on folding and boudinage under plane strain: Results from analogue modelling. – Geotectonic Research (submitted).

Enama Mengong, M. and Zulauf, G., **2005**. Coeval folding and boudinage under plane strain with the axis of no change perpendicular to the layer. – International Journal of Earth Sciences (<http://dx.doi.org/10.1007/s00531-005-0032-z>).

Enama Mengong, M. and Zulauf, G., **2005**. Coeval folds and boudins under plane strain with the axis of no change perpendicular to the layer. Presented at the 101st Annual Meeting in San José, USA (*Tectonics of the U.S. Cordillera, Sweet Connection and Beyond III: A Session in Honor of Eldridge Moores; April 29 – May 1, 2005, USA*) (published as Oral presentation abstract).

Enama Mengong, M. and Zulauf, G., **2004**. Coeval folds and boudins under plane strain with the axis of no change perpendicular to the layer. TSK 10, Terra Nostra 01, p 58.

Enama Mengong, M. and Zulauf, G., **2004**. Coeval folds and boudins under plane strain with the axis of no change perpendicular to the layer; *26th Nordic Geological Winter Meeting in Uppsala; January 06 – 09, 2004, Sweden* (published as poster abstract).

Enama Mengong, M. and Zulauf, G., **2003**. Coeval folds and boudins under plane strain with the axis of no change perpendicular to the layer. European Journal of Mineralogy, 81. Jahrestagung der Deutschen Mineralogischen Gesellschaft vom 22. bis 25. September 2003 in Bochum (Germany), p 46.

Enama Mengong, M. and Zulauf, G., **2002**. Coeval folds and boudins under plane-strain: First results from analogue modelling. TSK 9, Erlanger Geologische Abhandlungen, Sonderband 3, 67 – 68.

Ajonina, N. H., **Enama Mengong, M.**, Zulauf, G. and Ajibola. A., **2002**. A model for the tectono-stratigraphic evolution of the Mamfe Basin, West Africa (**Abstract**).

Enama Mengong, M., Zulauf, G., Ajonina. N. H. and Ajibola. A., **2002**. Sedimentology of the upper Mamfe formation, Mamfe Basin, West Africa (**Abstract**).

Erklärung

Hiermit erkläre ich, Mathurin Enama Mengong, geb. 07.06.1973, dass ich die vorgelegte Dissertation nur mit den von mir angegebenen Hilfsmitteln verfasst habe. Ich habe keine fremde Hilfe in Anspruch genommen, die nicht in der Dissertation angegeben wurde.

Mathurin Enama Mengong